Università degli Studi di Cagliari

Dipartimento Di Ingegneria Elettrica Ed Elettronica
Corso di Dottorato di Ricerca in Ingegneria Elettronica e Informatica
Ciclo XXXI

Ph.D. Thesis

Development of an Integrated Battery Management System for Improving Power Quality in Microgrids.

Author:
Andrea Salimbeni

Supervisor:
Prof. Alfonso Damiano

Ph.D. Coordinator:
Prof. Fabio Roli

February 2019

CONTENTS

ABSTRACT

The present dissertation concerns about the implementation of a novel configuration of an Integrated Active Filtering System (AFS), coupled with a Sodium Metal Halides Battery (SMHB), to improve Power Quality in Microgrids.

This work is developed within the European H2020 project NETfficient, "*Energy and Economic Efficiency for Today's Smart Communities through Integrated Multi Storage Technologies*", under grant agreement No 646463.

The first chapter is dedicated to state of the art analysis of all technologies involved in the present work. In particular, Microgrid (MG) paradigm, active filters and the SMHB technology have been discussed in depth.

The second and the third chapters show two case-studies related to Microgrids installed in the Renewable Energy Platform of Sardegna Ricerche in Macchiareddu, Sardinia. In these chapters, the technical-economic feasibility of a microgrid implementation has been analysed. Two different solar power generation configurations have been investigated (amorphous and concentrated photovoltaic generation).

The next chapter regards the implementation of the control algorithm of the AFS. The proposed control algorithm is based on the identification of the instantaneous active power which allows the determination of the switching pattern sequence for properly controlling a Four-Leg Voltage Source Inverter (4L-VSI). The control system allows at the same time the definition of charging/discharging battery current values. The adopted 3D Space Vector Pulse Width Modulation (3D-SVPWM) has been described and the results of a simulation on Matlab-Simulink environment has been shown.

In the fifth chapter the Sodium Metal Halides Battery technology has been investigated deeply. In particular, the implementation of a novel Thévenin equivalent circuit model has been presented. A comparison between an improved model that considers the presence of iron reactions and one that does not consider it, and the associated results have been shown.

The sixth chapter is focused on the sizing criteria of an LC-filter aimed to decouple the AFS and the SMHB. The sizing procedure and the results in terms of decoupling capability have been shown.

The next chapter analyses different Frequency Based energy Management (FBM) aimed to optimise the charging and discharging phases of an Hybrid Energy Storage System (HESS). Two algorithms have been compared, highlighting advantages and disadvantages of the two different strategies. The algorithm has been tasted based on residual power data related to the island of Borkum, in Germany, place of the NETfficient project implementation.

Finally, in the seventh chapter the implementation on FPGA of the control algorithm for the modulation of a 4L-VSI has been developed on LabVIEW environment and the first tests on the effective operation of the chosen modulation on a prototype inverter assembled in the laboratory, has been presented.

OVERVIEW

INTRODUCTION

In recent years the importance that the major media have given to climate change has increased significantly. If at first the issue concerned only some technicians or some personalities with a particular interest in environmental issues, now it is also discussed in the mass media [1], it strongly affects the daily political debate [2] and many celebrities have made public statements or taken part in awareness campaigns [3][4][5]. Since the 1960s, when the concept of greenhouse effect had migrated from academic journals to the minds of policymakers; to 1980s, when the attitude changed and media started bringing scientists' concerns into mainstream conversation; the situation has changed over the time to present itself as a political stance in recent years: in fact, since 2000s, climate change had become a partisan issue and this had a greater impact in the United States [6].

Concerning international agreements about climate-change, since when the United Nations Framework Convention on Climate Change (UNFCCC) was adopted, on May the 9th 1992, twenty-three international climate summits have taken place, the so-called Conferences of the Parties (COPs). They represent an attempt to tackle this situation by international coordination – with 194 of the world's 206 states participating [1]. The Kyoto protocol (1997) and the Paris agreement (2015) are the most important documents drawn up during COPs. The first treaty defined strategies for reducing greenhouse gases emissions with specific targets set for 2012, extended after 2020 during the 18th COP held in Doha in 2012. In view of the close conclusion of the Kyoto Protocol in 2012, in 2009 the Directive 2009/29/EC set the strategy 20-20- 20, which came into force in 2013 and will last until 2020. The second treaty defined the strategies to be adopted starting from 2020. The role of the United States, one of the countries with the greatest impact in terms of greenhouse gas emissions, was ambiguous for both treaties: ratified at first by Clinton (Kyoto) and Obama (Paris), were later rejected by the new government of Bush (Kyoto) and Trump (Paris)[1][7][8].

In this context, the three main strategies introduced by the aforementioned European directive reflect the areas of intervention that are considered most important: reduction of emissions, reduction of energy demand, increase in the production of energy from renewable sources. Precisely because of this last point, on January 26 2009, the International Renew-

able Energy Agency (IRENA) was officially created. The charter of IRENA is to close the gap between the enormous potential of renewable energy resources and their low market penetration, by advising its members in a fashion similar to its sister agencies: the oil-focused International Energy Agency (IEA) and the nuclear-focused International Atomic Energy Agency (IAEA) [9]. With this aim IRENA published a report in 2018, "Global Energy Transformation: A Road map to 2050", which analyses from a technical-economic point of view how production from Renewable Energy Sources (RES) affects and would affect the targets set by the Paris agreement: the rise in average global temperature must be limited to "well below 2°C" in the present century, compared to pre-industrial levels. The report begins with the sentence:

"Renewable energy needs to be scaled up at least six times faster for the world to start to meet the goals set out in the Paris Agreement."

The document also states that:

"Keeping the global temperature rise below 2 degrees Celsius (°C) is technically feasible. It would also be more economically, socially and environmentally beneficial than the path resulting from current plans and policies."[10]

Therefore, according to the document drawn up by IRENA, the increase in temperature due to climate change is more likely to remain within the limits set by the Paris Agreement if the societies focus on policies related to renewable resources and energy efficiency. A comparison of the cumulative trend of CO_2 emissions according to current policies and that proposed by IRENA simulations, is presented in Fig.1. The expected temperature increase is also associated with the CO_2 cumulative emissions trend.

With the same purpose, the IRENA simulation considers that "the total share of renewable energy must rise from around 15% of Total Primary Energy Supply (TPES) in 2015 to around 66% in 2050", compared to the 27% that would be obtained with the current policies. This comparison is shown in Fig.2. Moreover, IRENA states that the rising in the percentage of renewable energy in the power sector should be set from 25% in 2017 to 85% in 2050, requiring considerable changes in technical, economic and political strategies. In particular, in Europe, the percentage should rise to 70%. This transition would also lead to an increase in the energy sector employment if the right management policies would be promoted.

The IRENA report identifies six main operational areas on which to act, in order to successfully start the transition necessary to achieve the objectives set by the Paris Agreement.

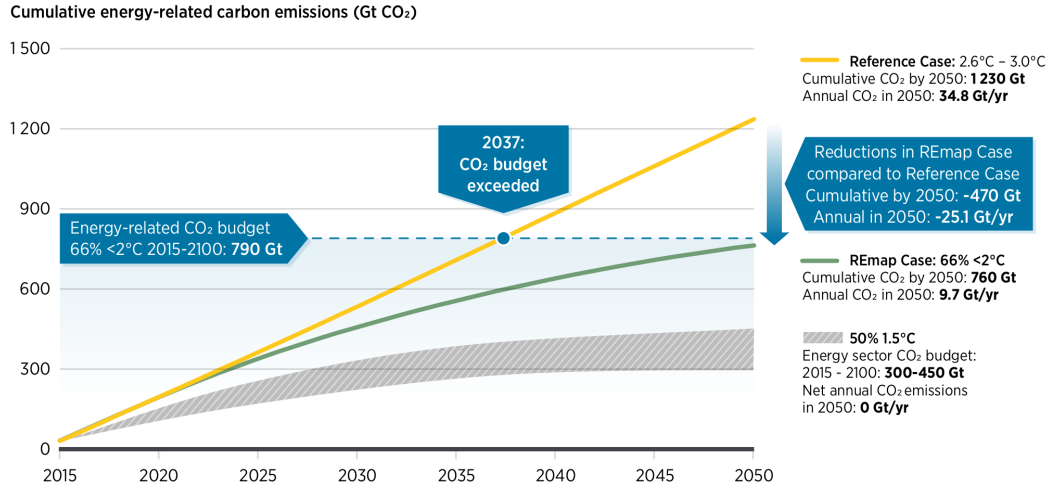

Figure 1: Comparison between the CO_2 cumulative emissions trend according to current policies and the proposed IRENA simulation.

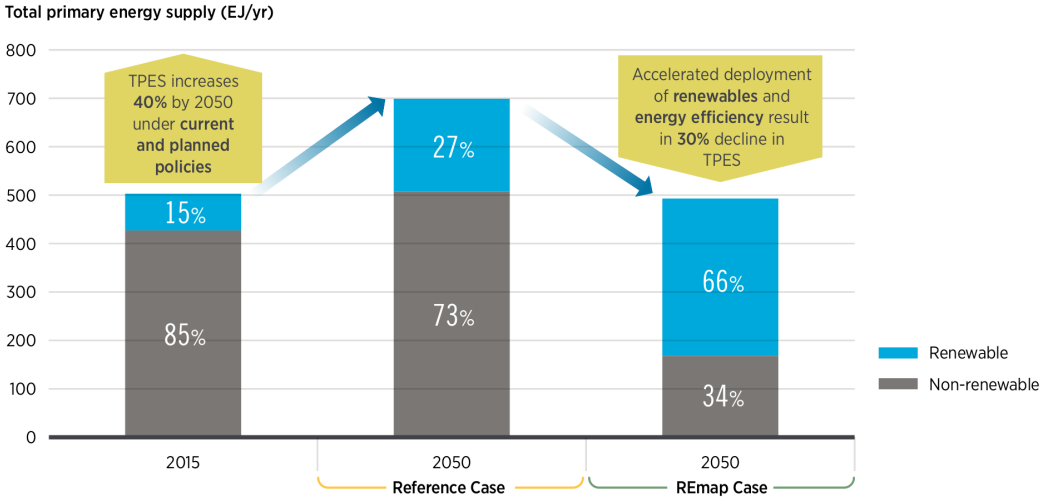

Figure 2: Comparison between REmap and Reference cases regarding the global share of renewable energy.

1. Investigate the synergies between energy efficiency and renewable energy;

2. Planning the power sector with the aim of raising the share of renewable energy;

3. Raise the use of electricity in transport, building and industry;

4. Foster innovation,

5. Change socio-economic structures and investments to make them suitable for transition;

6. Ensuring fair distribution of costs and benefits of the transition.

Points one, two and four are those on which this thesis will focus more. It is worth noting how approaches that combine the innovation, the synergy between energy efficiency and renewable resources, the increase in the share of energy produced from renewable sources, are certainly very interesting in order to achieve the aforementioned objectives.

In this regard, distributed generation paradigms, particularly Microgrids, are considered among the most promising solutions. In fact, UNFCCC has focused its attention on this energy model and in the document entitled "Background paper on distributed renewable energy generation and integration", analyses the Distributed Renewable Electricity Generating Technologies (DREGTs). First of all, it should be considered that, at present time, both the centralised system and the distributed one present pros and cons; The increase of the incidence of distributed generation on the total energy production has to consider these factors. Tab.1 summarises the main advantages of this two different energy models. [11]. Furthermore, Tab.2 shows the classification adopted in relation to the users involved.

In particular, the term "Off-grid", adopted in power system, refers to a single isolated structure that produces its own energy. Instead "Nanogrids",

Table 1: Advantages of the two different typology of energy generation.

Tipology	Advantages
Centralised	Wide range of mature technologies Lower per-kW costs Higher load diversity that implies flatter demand profile Well-developed industry
Distributed	Appropriate for small/remote communities Greater system resilience due to diversity of supply Reduced Transmission and Distribution (T&D) losses Allows for direct private investment in generation

Table 2: Terminology for the definition of a grid according to the installed power (it refers to individual technology)

Terminology	Number of users	Capacity [kW]
Off-grid	1	1
Nanogrids	$1 < x \leqslant 10$	
Microgrids	$10 < x \leqslant 100$	$1 < x \leqslant 1000$
Minigrids	$100 < x \leqslant 1000$	
Utility grid	$x > 1000$	$x > 1000$

"Microgrids" and "Minigrids" refer to power system configurations supported by inner energy generation, with power between 10 and 1000 kW, that can operate both in grid-connected or in islanded mode.

The prospect of working in island mode introduces several issues related to the unplanned RES energy production and to the management of the Nano/Micro/Minigrid. For those reasons, the storage and the smart-grid management could be considered as enabling technologies capable to ease the widespread application of DREGTs, although they are not considered absolutely necessary for the DREGTs success [11].

The number of power plants, based on the off-grid paradigm and fed by different RESs, has been increasing in recent years, bringing the installed world power from 1909.684 MW in 2008 to 6574.595 MW in 2018, which corresponds to an increase of 344%, as highlighted in Fig.3 and Fig.4 [12] [13].

Based on these premises, the recent research activities are more focused on these aspects and on Power Quality. In particular, the control system will have the objective of determining the action necessary to compensate for the current and voltage harmonic distortions present in the main grid

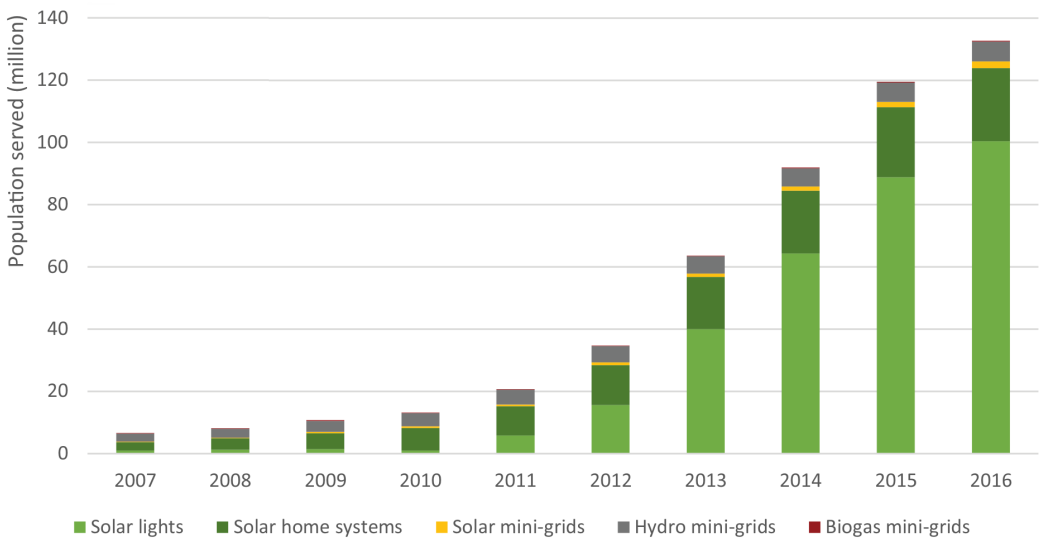

Figure 3: Population served by off-grid renewable energy solutions globally [12].

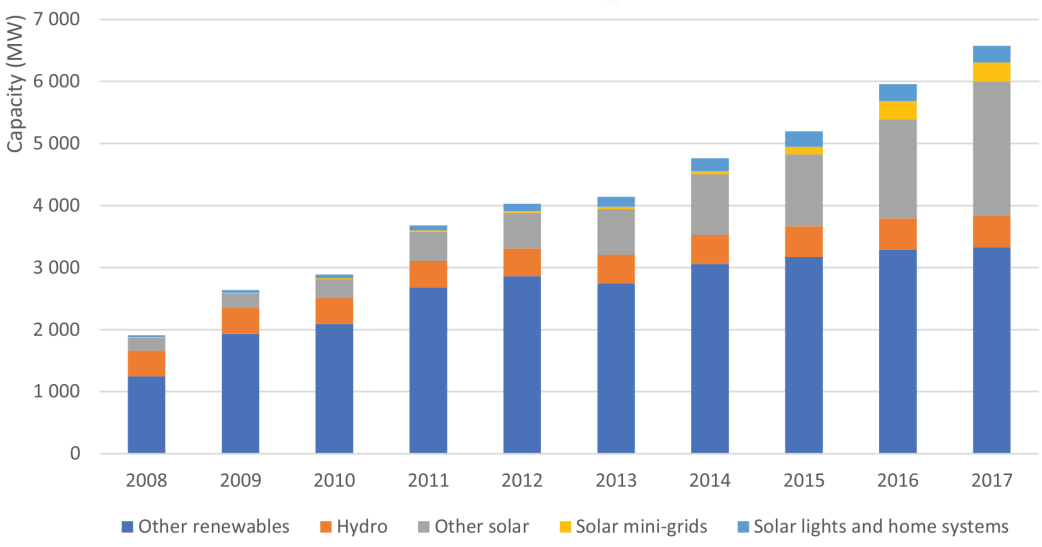

Figure 4: Capacity of off-grid renewable energy solutions globally [12].

and, at the same time, to manage the charge and discharge of the storage through the management of the active filter itself. The storage management is also based on the usage of predictive algorithms that allow the limitation of drawbacks associated to the intermittence of RES power generation. Therefore, the aforementioned control system will have improvement actions on power quality, battery management, self-consumption and microgrid efficiency. The research activity was carried out in the laboratories of Electric Energy at the Piattaforma Energie Rinnovabili of Sardegna Ricerche, in Macchiareddu, Sardinia; with the future goal of putting the system in operation in the same building.

The present work is structured in nine chapters organised as follows:

THE FIRST CHAPTER presents an analysis of the state of the art of the main technologies considered in this thesis: active filters, battery modelling, Microgrids and battery management algorithms, particularly SMHB. This chapter explains the technical-scientific context of the topics presented below.

The next two chapters constitute case studies that have made it possible to draw the necessary considerations on the technical and economic feasibility of the microgrid in the laboratory building. These have allowed the testing of the dummy energy management control algorithm implemented at the present time in the commercial converter, giving the possibility to monitor all the quantities involved.

THE SECOND CHAPTER deals with a monitoring campaign of a Microgrid installed in the Renewable Energies Platform of Sardegna Ricerche in Macchiareddu. The Microgrid consists of an amorphous photovoltaic power plant, that supply the offices of the Platform, and a storage system composed of lithium batteries;

THE THIRD CHAPTER deals with a second monitoring campaign of Microgrid installed in the same laboratories but this time supplied by a concentrator photovoltaic power plant.

The following chapters analyse the presented AFS.

THE FOURTH CHAPTER deals with simulations carried out to test the active filter control algorithm, in order to have results to reflect on before implementing the system experimentally. This algorithm is based on the determination in Real Time of the instantaneous active power at the Point of Common Coupling (PCC);

THE FIFTH CHAPTER deals with the modelling of the SMHB battery which will be used as the DC power supply of the active filter. In fact, the correct modelling of the battery behaviour makes the results of the simulations performed in chapter three even more meaningful. Furthermore, it allows preliminary testing of the battery behaviour under different operating conditions, without risking malfunctions or damage;

THE SIXTH CHAPTER deals with the LC filter that will be installed between the converter and the battery, in order to separate the two dynamics of the two elements of the system. The fast dynamics of the current absorbed by the converter would, in fact, degrade the life of the battery considerably;

THE SEVENTH CHAPTER deals with a possible batteries management system based on predictive data, in order to optimize the charge and discharge cycles, improve the battery usage and therefore the self-consumption of the system.

THE EIGHT CHAPTER deals with the experimental implementation of the control algorithm presented in chapter 4. The control algorithm has been developed on an Field Programmable Gate Array (FPGA) platform using National Instruments hardware in LabVIEW environment.

THE LAST CHAPTER presents the conclusions and possible future developments of the presented system.

1 STATE OF THE ART

1.1 MICROGRIDS

The awareness of climate change producible by the energy systems has driven the worldwide policies to promote a sustainable energy transition. In order to combine the growing energy demand together with a sustainable development, a significant support to the distributed energy production based on RES has been accomplished in these last years. This has led to the important growth of the RES in the past decade and this trend is foreseen to continue [10]. The share of the renewable in the world total energy production has been estimated as at least 26.5% at the end of 2017 [14]. In particular, the cumulative solar photovoltaic (PV) capacity installed worldwide in 2017 was of 402 GW.

It should be considered that this transition from the centralized and programmable energy generation to the Distributed Generation (DG), based often on non-programmable sources is challenging for the electric power system. Therefore, its structure and the control strategy used for the management of the electrical network are going to deeply change due to the increasing penetration of RES and DG systems. A flexible, continuous and real-time supply of the demand, which takes into account also the energy losses, is a required condition that should be satisfied by the power system.

Consequently, an intensive research is worldwide devoted to the development of new technologies, models, structures and control algorithms aimed at overcoming the critical aspects connected to the fast and rapid growth of RES and DG installations [15].

Among many technical solutions proposed in literature, the concept that appears prominent and feasible is related to the development of the energy Microgrids (MGs) [16–18]. A widely recognized definition of the MG has been formulated by the U.S. Department of Energy's Microgrid Initiative. It states that "*microgrid is a group of interconnected loads and distributed energy resources within clearly defined electrical boundaries that acts as a single controllable entity with respect to the grid. A Microgrid can connect and disconnect from the grid to enable it to operate in both "grid-connected or island-mode*" [19].

In Fig.5 a schematic of a Microgrid (MG) has been depicted.

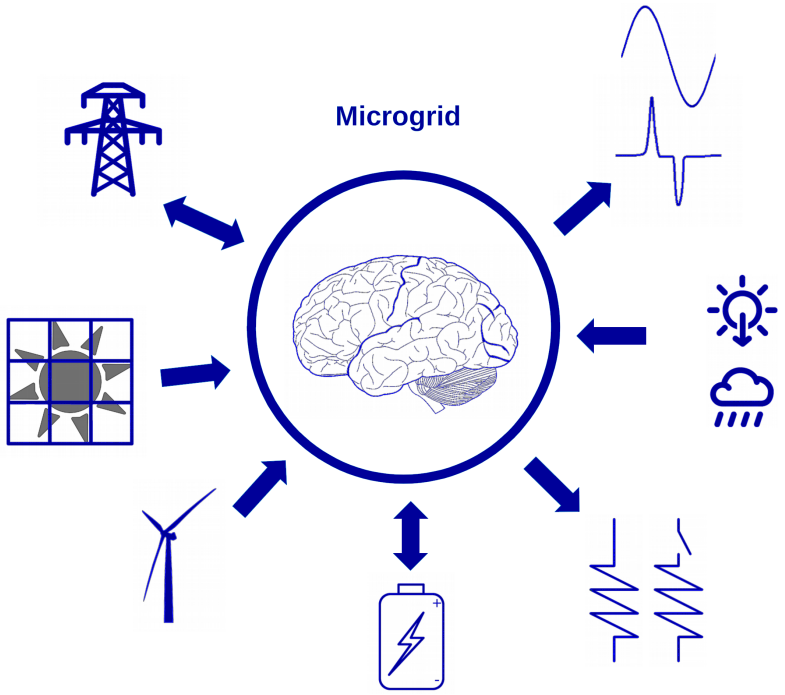

Figure 5: A schematic representation of a generic Microgrid.

In this novel energy configuration, the ESS and the local electricity generators supplied by RES represent key components. Particularly, the RES-based generators have to be properly sized to guarantee an electricity production able to support the average of the MG daily energy demand [18]. On the other side, ESSs have to support the MG energy management system by carrying out the time shifting of electricity generation and load demand, in order to be able to balance the power and energy mismatching occurring between demand and production [20–22]. In particular, the electrochemical batteries are currently considered one of the most efficient and versatile ESS technologies for the implementation of MG concept [23, 24].

Different procedures to define the control strategy and the energy management implementation are defined in the scientific literature, e.g. droop control, hierarchical control [25, 26].

The standard P-Q controls, related to the Synchronous Machine of the main power grid, is not suitable for high-quality energy management in Microgrids because of the presence of an high number of RES. In order to achieve the necessary stability and reliability, to avoid power oscillation and circulation of excessive reactive currents between power sources. The

MG has not an high impedance between generators like in main power grids, for this reason the problem of the reactive currents circulation has to be investigated. The droop control considering voltage and reactive current consists in reducing/increasing the voltage set point if the reactive current become more capacitive/inductive.

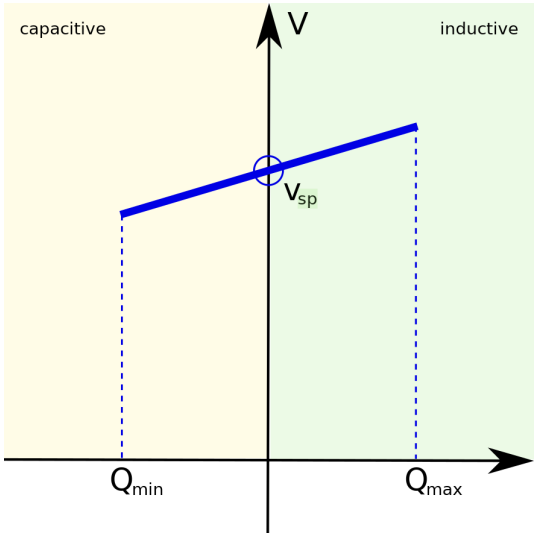

Figure 6: Voltage droop control schematic and voltage set point (V_{sp}), inductive area (cyan) and capacitive area (yellow).

In Fig.6 the schematic of the control is depicted.

The requirement to track the load variation with appropriate change in power, has consequences as errors in the frequency of the RES output generation. For this reason, the implementation of a power-frequency droop control at each source is suitable [27]. This event can occur especially during the transition from grid-connected to island mode, causing a reduction of the frequency value.

In Fig.7 is show an example of frequency variation after a load change. The two sources have different rated power (P_{1max}, P_{2max}). When the MG is connected to the grid, the two RES are working at P_{01}, P_{02} and at the grid frequency ω_0. If the load power demand changes, the droop control forced the two RES to move on another balance configuration corresponding to a lower frequency value, that must not be lower than the minimum frequency ω_{min}. In order to allow this type of control the two RES have work not at their maximum power. It is suitable to implement also a restoring algorithm in order to increase again the frequency after the transition. This

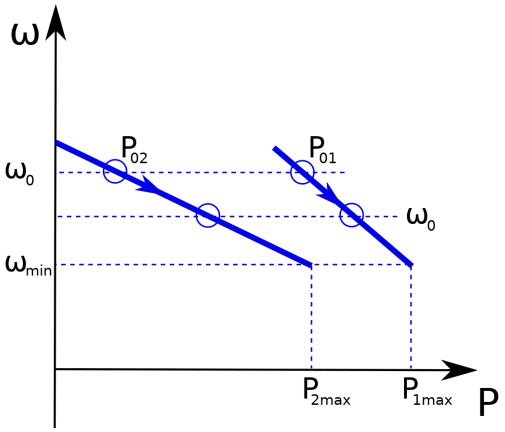

Figure 7: Frequency droop control schematic considering two different RES.

control operates also during island mode with the aim of redistributing the share of load [27].

Nevertheless, should be also considered that the lack of synchronous generator in MG make this architecture devoid of inertia, in fact, the other RES have slow response. A controlled storage could prevent this dynamics. Typical storage used for this purpose are batteries, supercapacitors, flywheels, connected on dc or ac side [27]. Another novel technology aimed to give inertia to a MG is the synchronverter [28].

In particular, the number of papers focusing on the integration, sizing and control of ESS in MG are is growing considerably, pointing out the importance and feasibility of DG supplied by RES [29–32]. Moreover, systems that considers the utilisation of series and/or parallel inverters in a MG have been investigated. A promising configuration consists of a first converter (series) used to perform harmonic compensation and to manage grid faults, a second converter (shunt) focused on voltage and load balancing [33]. This aspect is strongly related to the topic in section 1.3 and will be discussed in that section.

1.2 RES: CONCENTRATOR PHOTOVOLTAIC IN DEPTH

Because of the concentration photovoltaic power plant, in the structure where the Electric Energy Laboratory is located at Sardegna Ricerche, was used for a campaign of measures aimed at characterising the functioning

of a MG supplied by this technology, see 3, it was decided to dedicate this section to highlight its properties.

The rapid growth and development of technologies related to solar energy conversion have made the Photovoltaic (PV) one of the most reliable and efficient renewable generation system, especially suitable for MG. In particular, the concentrator photovoltaic is at the present time the most efficient solar energy conversion technology characterized by solar cell energy conversion efficiency that has reached 46% and there is still room for improvement [34, 35]. The energy conversion efficiency for commercial Concentrator Photovoltaic (CPV) systems is much beyond the highest obtainable efficiency of traditional Si-based PV modules. A typical CPV module is composed of optical elements, such as lenses or mirrors, which focus Direct Normal Irradiance (DNI) on small size solar cells, which generate current under the solar light. Usually, CPV modules are mounted on solar trackers which orient the modules' surface towards the sun during the day, in order to capture the direct component of solar irradiation [36, 37]. The worldwide experiences developed on this technology have demonstrated that CPV power plants represent a promising solution for renewable energy generation, particularly for those regions with high annual DNI values that makes the levelised cost of electricity of CPV equal to that of traditional PV but with a significant reduction of the collecting area involved [38]. Regions with high annual irradiation such as north and south Africa or Australia are suitable for making economically sustainable the CPV technology. As far as Europe is concerned, a CPV power plant can be implemented in southern areas, such as Spain, Italy, Greece or Cyprus, due to suitable annual DNI values [39]. The recent development of flat plate CPV technologies, characterised by the use of micro-motor used for moving the lens inside the flat CPV panel in order to integrate the tracker, make them similar to the traditional Si-based PV modules. In this future perspective, the CPV becomes an interesting solution for energy generation in domestic and building MGs too. Nevertheless, the CPV has also some important drawbacks. It is often mentioned that the modules require frequent cleaning, especially in some specific sites and that the tracking system has to be very accurate in order to guaranty the energy production. Moreover, as the CPV systems use only the direct component of the solar irradiation, strong variations in the energy production occur during the day, because the direct irradiation alterations are more frequent and marked respect to those of the global irradiation. For this reason, the CPV generates power characterised by high variability during a day, switching from

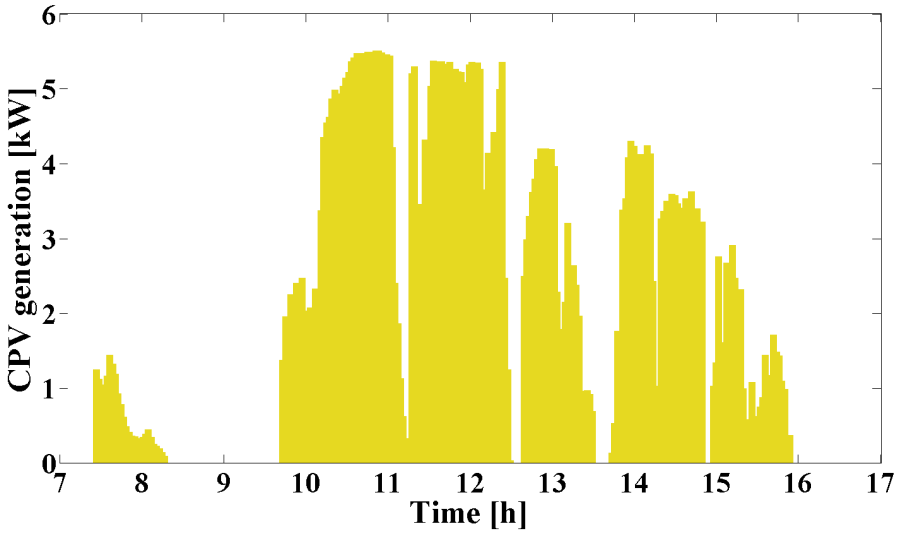

Figure 8: Monitored time evolution of the power generated by a CPV plant in Sardinia, Italy.

peak to zero values in a short time span. Fig.8 shows a typical daily CPV power generation profile registered in Sardinia, Italy. This intermittency is disadvantageous when the CPV is integrated into the main power grid.

Those fast variations in the power production are difficult to manage, above all in the case of MGs supplied by CPV, leading to significant fluctuations in the power supply. Consequently, a MG powered by CPV and operating in grid-connected mode should be strongly balanced with the contribution of the main grid. However, it can be a very challenging task to energetically balance a MG supplied by CPV when operating in island mode.

In order to mitigate this behaviour, and to optimize the demand response profiles within the CPV supplied microgrid, an implementation of an ESS coupled with CPV power plant could be considered as a solution. In fact, an ESS could, on one hand, support the microgrid in operating independently from the main power grid and, on the other hand, it would promote a stable and secure integration of CPV technology with the main grid. The employment of an ESS within a microgrid could be advantageous as, if properly managed, it could lead to an increment of the self-consumption rate of power generated by the CPV plant. Further, an implementation of an ESS would raise the cost-effectiveness of the renewable energy, bringing out also the possibility to offer services to the main grid.

1.3 MICROGRIDS POWER QUALITY: ACTIVE FILTERS

As highlighted in the previous chapters, the transition from a centralized to a distributed system drives the research on this topic to be oriented towards the development of novel technologies, models, structures and control algorithms aimed at overcoming the critical aspects connected to the integration, into the power grid, of a wide range of autonomous electricity systems supplied by RES.

The section 1.1 pointed out how Microgrids (MGs) can be considered very suitable solutions [40]. In this configuration the Energy Storage System (ESS) represents one of the most important components because it can cover several functions such as time shifting of electricity generation and load demand; the balance of the errors occurring in the forecast of local demand and production; errors in system modelling [41, 42]. In particular, electrochemical batteries are currently considered one of the most efficient and versatile ESS technologies for MG applications [43]. However, the intermittent and distributed characteristics of RES-based power generations joint with the demand transformation induced by the self-consumption, affect the power quality. This is due to the presence of unpredictable voltage and current variations on the electricity distribution system which is perceived by the front-end inverters as an apparent grid impedance variation. This leads to currents and voltage distortions and also instability events, connected to the origin of interaction phenomena occurring among the inverter LCL filters, the grid and the control algorithms used to manage the energy conversion processes [44].

Furthermore, the exploitation of 1-6kW roof-mounted PV power plants, characterised by the use of single-phase self-commutated voltage-source converters, contribute to magnify the time-varying and unbalanced conditions, relative to non-linear load, on the distribution electricity system. This gives rise to an increase in the Total Harmonic Distortion (THD) of currents (of line and neutral) which causes parallel and series resonance phenomena among the network, the DG and non-linear loads [45]. In this scenario, the use of harmonic compensation techniques is going to become a mandatory requirement in order to improve the efficiency, the power quality and to avoid the occurrence of instability phenomena during the implementation of the energy management in MGs. The use of shunt active power filters with 4L-VSI is considered at the present time one of the most accredited solutions to compensate current harmonic components, as well as unbalanced load conditions produced by non-linear and single-phase devices

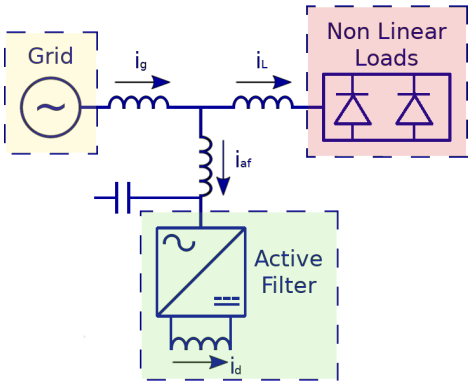

Figure 9: Shunt AFS based on CSI.

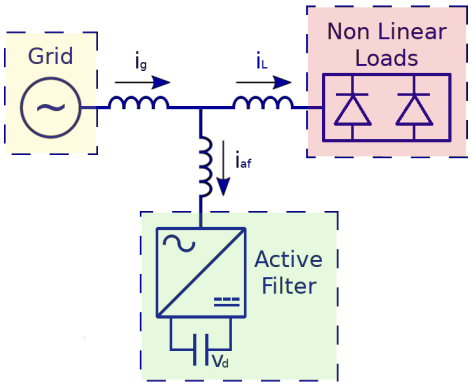

Figure 10: Shunt AFS based on VSI.

(loads and DGs) [46]. The most common configuration of AFS are depicted in Fig.9, Fig.10, Fig.11, Fig.12, Fig.13.

The first two configurations are constituted by a CSI or a VSI, connected in parallel with the main grid. The current sourced configuration needs a high value of AC power capacitor. The voltage sourced configuration has become more common because is cheaper, lighter and expandable to multilevel or multistep versions [47]. The configuration in Fig.10 is also a typical example of shunt active filter configuration.

On the contrary, Fig.11 shows a series active filter, connected to the main grid by means of a transformer.

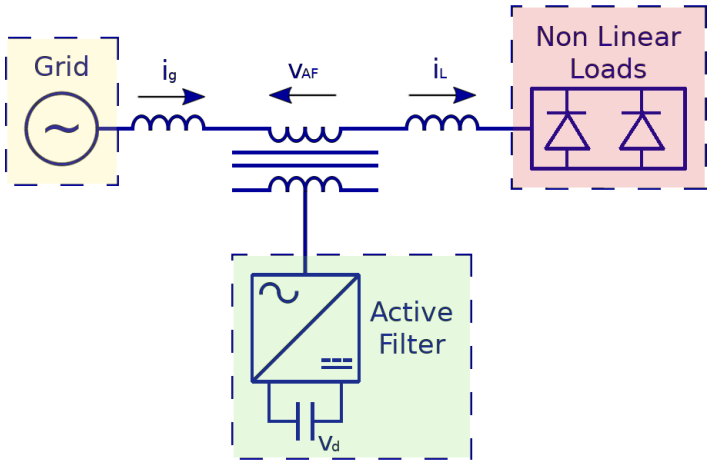

Figure 11: Series AFS based on VSI connected by a transformer.

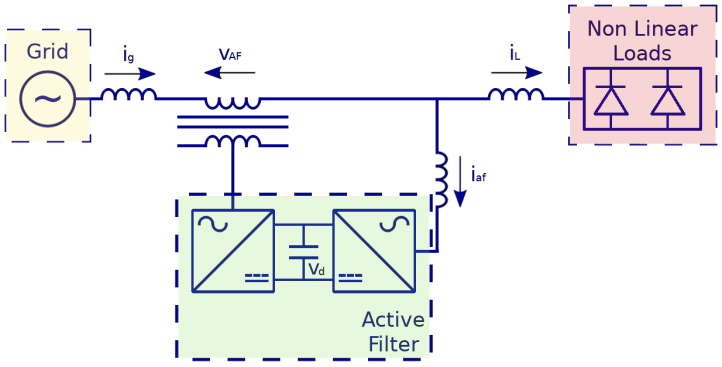

Figure 12: Series and Shunt AFS, this configuration is also known as UPQC.

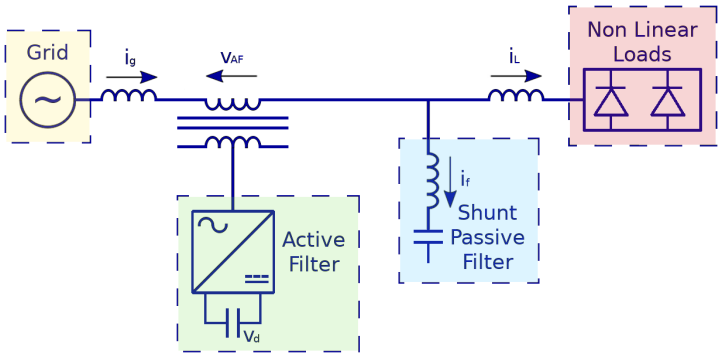

Figure 13: Series AFS based on VSI, connected by a transformer, in parallel with a shunt passive filter.

The coupling, within the same system, of a series active filter and a shunt one, is known as Unified Power Quality Conditioner (UPQC). The two converters can both be CSI or VSI and shares the same dc-link. The UPQC configuration is depicted in Fig.12. This is considered the best solution for active filtering but its main drawbacks are the high cost and the complexity of its control algorithm [47].

The high cost can be reduced by relying on the solution of Fig.13, in which a hybrid filter consisting of a series active filter and a shunt passive one is shown. This solution allows to highly reduce the size of the active filter and consequently its cost [47]. Normally the series configuration is used to eliminate voltage harmonics, spikes, sags, notches, etc., while the shunt one is mainly related to the elimination of current harmonics and the compensation of reactive power [47]. AFSs can be also classified as single phase (two wire), three phase (three wire), three phase (four wire). In this work, more attention was paid to the type of three phases, four wires. This particular configuration can be divided in three main different solutions: the first one is knows as Capacitor-midpoint topology and considers a neutral leg constituted by two capacitors of large value (Fig.14); the second one is the so called Four Switch-Pole topology, constitute by a four leg inverter in which also the neutral leg is modulated (Fig.15) [48]; the third one considers one inverter for each phase and is called Three-bridge four-wire shunt AFS (Fig.16) [47]. It is worth noting that the main differences are in terms of cost and accuracy.

One of the most important aspects of the implementation of an active filter is the control algorithm. In literature, this is normally divided into

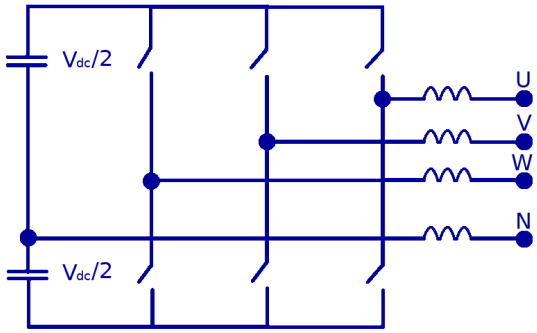

Figure 14: Capacitor-midpoint topology of a three phase, four wire active filter.

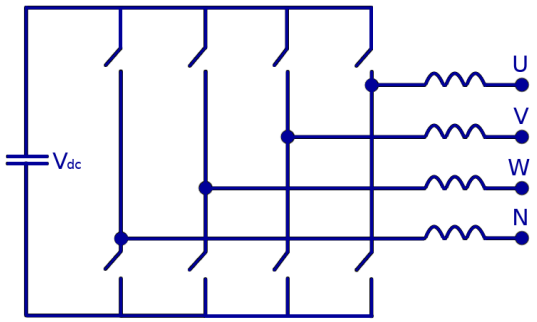

Figure 15: Four Switch-Pole topology of a three phase, four wire active filter.

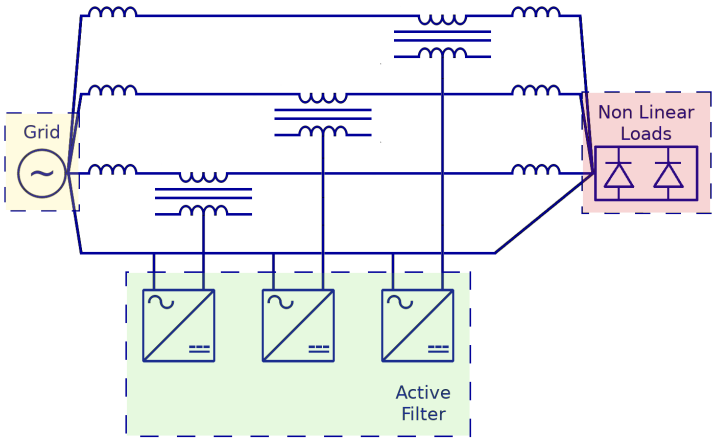

Figure 16: Three-bridge four-wire shunt AFS topology.

three distinct steps: acquisition, determination of compensating currents, generation of the gates control signals of the inverter. The determination of the compensating currents can take place in the frequency domain or in the time domain. The first type involves the Fourier analysis of the acquired signals to extract the value of compensating currents and with respect to the other one is the most exhaustively computational method. The second type concerns methods based on the calculation of the instantaneous powers, on the synchronous reference frame, on PI or sliding-mode controllers, on notch filter [47].

Furthermore, a common solution is to connect a series inductance to the output of the active filter. Its sizing is a very critical procedure because a too low value increases the ripple too much on the output signal, while a too high value does not allow suitable dynamics.

The present work concerns a shunt AFS based on the synchronous reference frame method and realised firstly in Matlab/Simulink environment (chapter 4), then in LabVIEW environment (chapter 8).

1.4 MICROGRIDS ENERGY STORAGE SYSTEMS

As discussed in chapter and section 1.1, the issues related to power fluctuations of RES generation as well as load variations on distribution system, require more flexibility and intelligence in the energy management, making the ESS a key component for the implementation of smart-based energy models [49].

At the present time, the different types of storage have features that make them suitable for different applications, either used individually or combined. Table 3 summarizes the main characteristics of the most common types of ESS.

1.4.1 *Lead-acid batteries*

Lead-acid battery technology is one of the oldest in electrochemical storage. They suffer particularly from the conditions of overcharge and overdischarge. The most common use of this type of batteries is related to application characterised by low energy density, limited life cycle and abuse tolerance as the automotive starting, lighting and Uninterruptible Power Supply (UPS) [50].

Table 3: Energy storage system typology [50].

ESS	Energy Efficiency (%)	Energy Density (Wh/kg)	Power Density (W/kg)	Life Cycle (Cycles)	Self (-)
Pb-Acid	70-80	20-35	25	200-2000	Low
Ni-Cd	60-90	40-60	140-180	500-2000	Low
Ni-MH	50-80	60-80	220	<3000	High
Li-Ion	70-85	100-200	360	500-2000	Medium
Li-polymer	70	200	250-1000	>1200	Medium
NaS	70	120	120	2000	-
VRB	80	25	80-150	>16000	Negligible
EDLC	95	<50	4000	>50000	Very High
Pumped Hydro	65-80	0.3	-	>20 years	Negligible
CAES	40-50	10-30	-	>20 years	-
Flywheel (steel)	95	5-30	1000	>20000	Very High
Flywheel (composite)	95	>50	5000	>20000	Very High
SMHB	85-90	>50	5000	>20000	Very High

1.4.2 *NiCd and NiMH batteries*

Nickel Cadmium (NiCd) batteries were most widely used between 1970 and 1990, after which they were gradually replaced by Nickel Metal Hydride (NiMH) and Li-ion in several applications. As highlighted in Tab.3 NiCd has lower energy density and life cycle than NiMH. Moreover, cadmium is toxic and requires complex processes to be recycled. The main drawback of NiMH is the higher self discharge.

1.4.3 *Li-ion batteries*

Li-ion batteries are characterised by high energy density, low self-discharge phenomena and the absence of memory effects. Their main applications are related to portable electronic devices and electric vehicles. One of the main drawbacks is the high cost and the need for a Battery Management System (BMS).

1.4.4 *NaS batteries*

Sodium Sulfur Batteries (NaS) are characterised by higher energy density than NiCd and NiMH, a comparable life cycle and medium self-discharge phenomena. Furthermore, this type of battery needs an external heater, but thanks to the materials it is made of, it still has a low cost.

1.4.5 *FBs batteries*

Zinc Bromide and Vanadium Redox are one type of so-called Flow Batteries (FBs). Their most important characteristic is the decoupling between energy and power. The structure of this battery technology is constituted of two tanks with the electrolytes that flow in a reactor. The power of the cell is a function of the reactor dimension and the flow rate, the energy capacity instead is related to the size of electrolytes tanks. Thanks to this structure FBs are easily adaptable to different applications, have a high life cycle and negligible self-discharge. Moreover, instead of inverting the reaction they offer the possibility to fast recharge by simply substituting electrolytes empty tanks with full ones. Last but not least materials used for FBs are not toxic.

1.4.6 *EDLC storage systems*

Electrochemical Double-Layer Capacitors (EDLCs) are high performance capacitors characterised by high capacitance values. This storage has high energy efficiency and very high power density. The lack of chemical reaction increase their life cycle. It is worth noting that EDLCs suffers high self-discharge.

1.4.7 *CAES storage systems*

Another type of storage involves compressing and decompressing air. Compressed Air Energy Storage (CAES) is a technology that is particularly used for network support services. The main issue of CAES is related to heat exchange during the process. The three main types derive from the three different solutions adopted to tackle this problem: isothermal, adiabatic and diabatic systems. At the present time CAES are mostly used in peak shaving applications.

1.4.8 *Flywheel storage systems*

Flywheels are designed to properly store rotational energy. This give them the intrinsic characteristic to supply very high peak power. This storage has high energy efficiency, high power density and a very high life cycle. As downside Flywheels suffers high self-discharge. Applications that required high charging/discharging cycles are the most suitable for this kind of technology.

1.4.9 *HESS storage systems*

The above-described storage systems do not necessarily represent a solution to be adopted individually depending on the required performance, indeed the combination of different storage types not only allows to increase the overall system performance but also to optimize the management of individual systems by exploiting their complementarities. For this reason, HESSs are studied with interest by the scientific community. The currently most studied combinations involve the association of batteries with EDLCs, CAES and Flywheel Energy Storage Systems (FESSs). In particular, in the present thesis work, the Battery + EDLCs solution was analysed. The next section, describe HESS in more detail. Furthermore, in the 7 chapter an FBM for the control of a HESS based on this configuration is discussed.

The previous list of the most common types of storage systems has highlighted that batteries, and therefore electrochemical systems, represent a very important section of this sector. In fact Electro-chemical Energy Storage System (E-ESS)s, due to their versatility, power scalability, efficiency and dynamic characteristics, are able to support the power system in providing the power, current and voltage compensations in presence of unexpected and unpredicted fluctuations [42, 43]. In energy and mobility sectors, lead-acid, lithium-ion, vanadium redox and sodium-sulfur (NaS) systems are currently the most consolidated electrochemical technologies for providing storage services [23, 51]. However, their use in stationary energy storage applications is limited owing to different factors. For instance, as described above, lead-acid batteries suffer from limited life cycle, the toxicity of lead and low energy density, whereas high energy cost as well as thermal and safety management issues are the challenges related to lithium-based technologies. Furthermore, NaS batteries still face several obstacles due to safety problems and risk of incidents. Therefore, alternative

battery technologies could be taken into consideration in order to provide successful storage requirements such as high energy density, low cost, high safety, increased life cycle and environmental compatibility. Moreover, the expected growth of E-ESS demand requires to pay attention to the availability of materials required to their production. In this context, the high temperature Sodium Metal Halides Battery (SMHB) are considered one of the most interesting novel E-ESS technologies. In chapter 5, SMHB main characteristics and a model implementation method are discussed in depth.

1.5 HESS MANAGEMENT

As shown in the previous section (1.5) HESSs represent a very promising solution for increasing MG performances in the next future [52, 53]. This is because the issues rising from the use of only one type of ESS can be overcome by employing two or more complementary storage technologies jointly. In this regard, the combination of batteries and supercapacitors has shown superior performances compared to other hybrid solutions, from both technical and economic points of view [54–57]. Particularly, batteries are more suited than capacitors for providing energy services [42, 58], such as load levelling and peak shaving, due to their higher energy density. Whereas supercapacitors are characterised by much higher power density compared to batteries [59, 60], revealing them as a suitable choice for providing power services (power quality, short-term forecasting error compensation, etc.). Consequently, the power split criterion is fundamental in order to exploit the HESS to the maximum extent. Several strategies for HESS energy management in MGs have been proposed in the literature [61–70]. The most popular approach consists of identifying low-frequency and high-frequency harmonic contents of the overall HESS power profile by means of low/high pass filters [61–64]. The low-frequency HESS power profile has to be tracked by a battery, which does not compensate for high-frequency power fluctuations in order to preserve its performances and life cycle. High-frequency HESS power profile can thus be handled by a supercapacitor safely, also because it is generally characterised by a relatively poor energy content. However, frequency-based management approaches are not able to account for the battery energy constraints properly, thus they are generally combined with rule-based and/or fuzzy logic algorithms in order to take into account HESS operating constraints [65–68]. In this context, a novel Frequency Based energy Management (FBM) suitable for

HESS to be installed in MGs is presented in this thesis. It is developed with the aim of enabling the HESS to provide both energy and power services, namely peak shaving and power quality. Adequate peak shaving capability is achieved by the battery through a management algorithm. This identifies suitable power thresholds based on forecasted MG profile over a given time horizon in order to guarantee the compliance with both battery energy and power constraints. In addition, the frequency-based power split criterion prevents the battery from coping with sudden power fluctuations, which are handled by the supercapacitor successfully due to their poor energy content. The proposed FBM is validated through numerical simulations, which have been performed referring to real MG data of the German island of Borkum. The results are presented in chapter 7.

DETAIL

2

ESS MANAGEMENT: CASE STUDY

In this chapter, the results of a ten months monitoring campaign of a MG supplied by a photovoltaic generator, and operating in the Mediterranean sea area, have been presented. The analysed MG architecture and the adopted control strategy have been described. Further, the analysis of the energy exchange between the MG and the main grid has been pointed out. A particular attention has been given to the optimisation of the renewable energy management in order to supply MG loads and consequently, to increase the photovoltaic energy self-consumption rate. This has been made possible thanks to the implementation of an energy storage system coupled with the photovoltaic generator. Results obtained demonstrate the technical feasibility of the MG, highlighting how the introduction of storage system improves the photovoltaic energy management. Moreover, it has been shown how the MG improves the integration of the photovoltaic system with the main grid. An economic evaluation of the costs incurred, for the development and maintenance of the MG, has been also carried out. The analysis has been reported also in terms of levelized cost of energy. The results show that the cost-effectiveness of the MG is increasing with the system operation lifetime.

2.1 THE MICROGRID INFRASTRUCTURE

The MG described in this chapter is a part of the Technology Park of Sardinia, a research centre situated in southern Italy. Currently, the centre's electric infrastructure has been organized in three different MGs, each of them fed by a dedicated PV generator. The generators have been realized in different PV technologies: monocrystalline-Si with a rated power of 10.3 kWp, amorphous-Si with a rated power of 7.8 kWp and CPV with a rated power of 6.2 kWp. Such a variety is caused by research nature of the activities carried out in the centre. One of them is the long-term comparison among the performances of the different types of PV generators. There are also two ESS that support PV generators, the first ESS is interfaced with the amorphous field and the second one with the CPV field. Additional RES

Table 4: Technical specification of amorphous modules SCHOTT ASI 86.

	Stabilised value	**Initial value**
P_{nom}	86 Wp	105 Wp
V_{mpp}	17.2 V	19 V
I_{mpp}	5 A	5.50 A
V_{oc}	23.3 V	24.3 V
I_{sc}	5.92 A	6.10 A
Efficiency	5.9	5.9

plants and ESSs are to be implemented within the centre's infrastructure in order to create a network of MGs, that work simultaneously and in a controlled manner, as to optimise the supply of the Technology Park loads.

Tab.4 shows the specifications of the installed amorphous modules.

Since the currently installed RES power plants are insufficient to fully cover the load demand, the Technology Park is grid connected and, when required, powered also from the main grid. In order to facilitate the future development of the control strategies that address the demand of the whole centre and take into consideration the limits of RES generators and ESSs, it is crucial to know the performances of single MGs installed in the centre. In the following paragraphs, the results of the monitoring of one of the MGs working in the centre are presented.

2.1.1 *MG configuration*

The MG is grid-connected and is composed by a photovoltaic generator, an inverter, a current measurement sensor, an electrochemical storage system and loads. The block diagram of the MG under tests together with the main components are presented in Fig.17. The PV generator is developed in amorphous-Si technology and composed of 90 modules, installed in three arrays of 30 modules. Two arrays are south-east oriented and one is south-west oriented. The rated PV generator power is of 7.8 kWp. The PV plant is connected to a three-phase inverter, which is also coupled with the ESS. The ESS is realized with Lithium Iron Phosphate battery characterized by a total capacity of 9.6 kWh.

The MG demand is typical of loads used in public administration offices and is represented by PCs, printers, fax, server and lighting. The MG

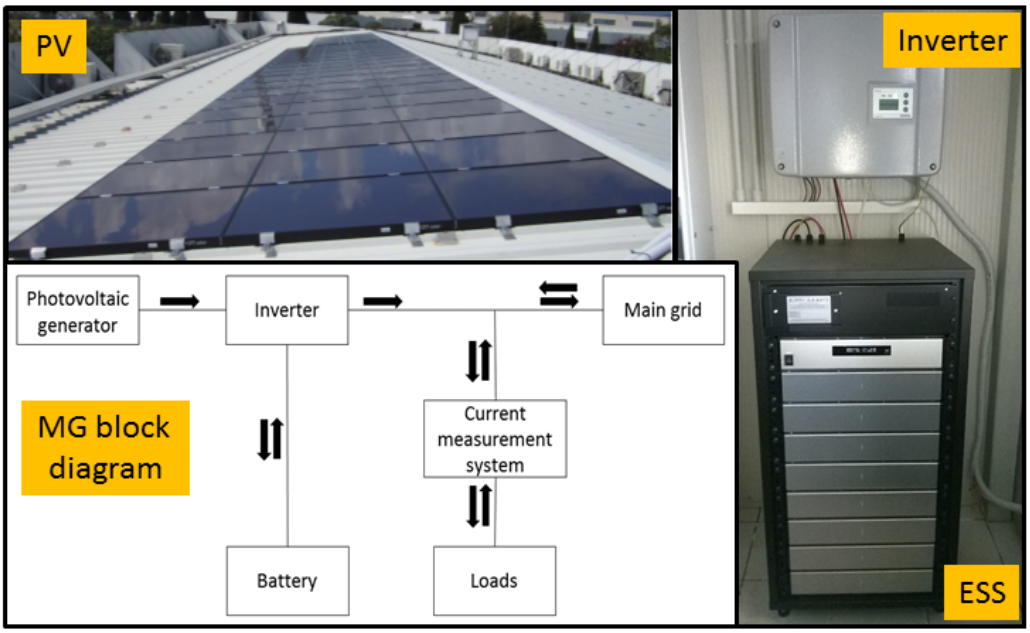

Figure 17: PV generator (top), ESS and inverter (right), Block diagram of the analysed MG(bottom).

consumption is continuously monitored by means of the current and voltage measuring probes. These parameters are recorded and instantaneously used by the MG control system to manage the energy fluxes. The control system is integrated inside the inverter and the energy transactions are managed in order to maximize the self-consumption in the MG referring to the energy generated from the PV.

2.1.2 *Mg load profile*

Fig. 18 depicts some typical load evolutions registered in the MG. As can be observed, the power demand never drops to zero value and there are differences between the profiles of a working day and non-working day. During non-working days the profile is flat and constant (blue colour). The load profiles registered during working days (red and green colour) show several variations corresponding with the labour time. For some days, which are represented by the case marked with the red colour, a peak of consumption occurs in the evening. For the analysed MG, which

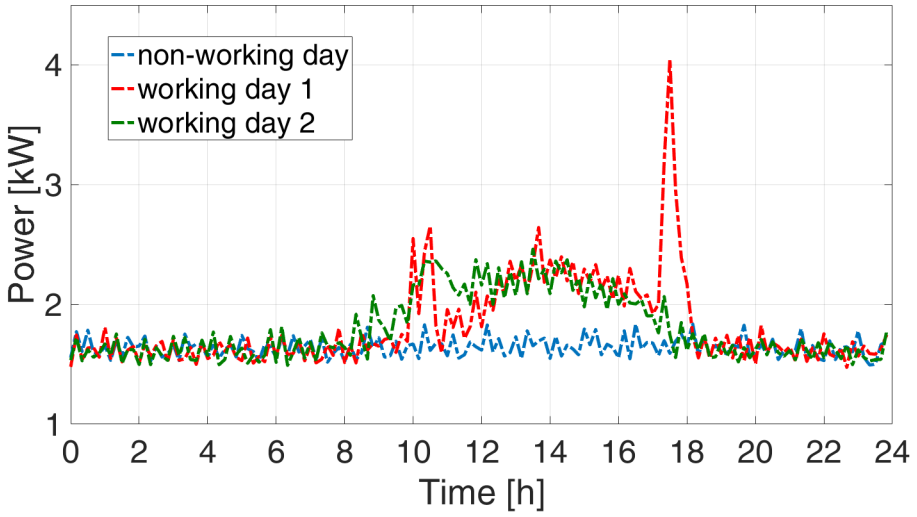

Figure 18: MG load evolution during three sample days.

is grid-connected, it influences the energy exchange between the MG and the main grid and has an impact on the economic aspects.

2.2 MG ENERGY MANAGEMENT: CASE STUDIES

The control strategy of the MG under test can be modified according to chosen priorities. In the case study described in this chapter, the preference has been given to maximizing of the PV self-consumption within the MG. In every moment, the balance condition of the MG in (1) has to be satisfied:

$$P_{grid} = P_{PV} + P_{ESS} + P_L; \tag{1}$$

where P_{grid} is the power exchanged between the MG and the main grid, P_{PV} is the power generated from the photovoltaic generator, P_{ESS} is the power drawn by/to the battery and P_L is the power related to the loads demand. Further, the lowest imposed battery State of Charge (SoC) is 10% in order to preserve its long duration. Finally, when the battery SoC reached the 90%, the charging process chages from current mode to voltage mode. Following these considerations, three different conditions of the MG operation can occur:

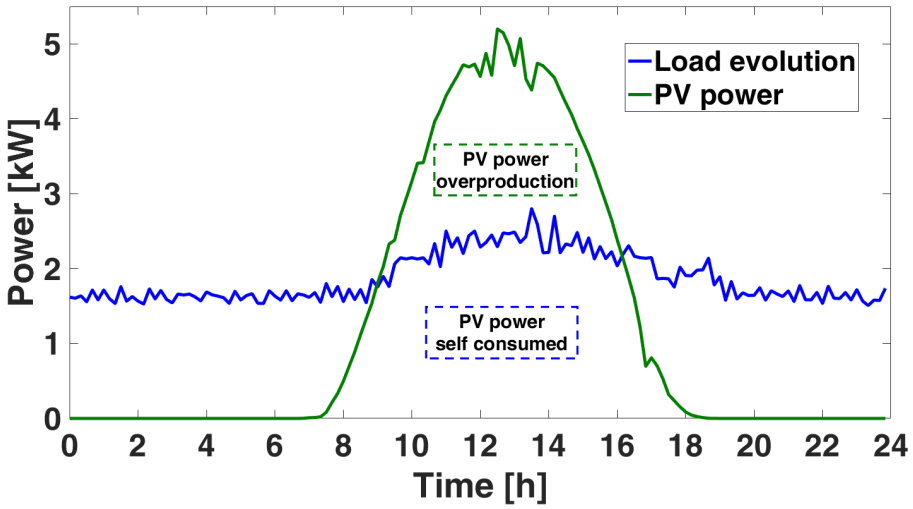

Figure 19: Daily PV power production and load evolution on a sunny day.

- If $0.1 \leqslant SoC \leqslant 0.9$ and $|P_{PV} + P_L| < max(P_{ESS})$, the balance condition in (1) becomes $P_{grid} = 0$ and the battery charging occurs;

- If $0.1 \leqslant SoC \leqslant 0.9$ and $|P_{PV} + P_L| > max(P_{ESS})$, $|P_{ESS}| = max(P_{ESS})$ due to battery constraint, the balance condition in (1) becomes $P_{grid} = P_{PV} + P_L - P_{ESS}$ and the battery discharging occurs;

- If $SoC \leqslant 0.1 \vee SoC \geqslant 0.9$ the balance condition in (1) becomes $P_{grid} = P_{PV} + P_L$ and the load demand is covered from the main grid.

2.2.1 *MG operation during the sunny day*

In Fig.19 the electricity load demand and the PV production time evolutions, for a sunny day (blue and green curves respectively), are presented. It can be observed that starting from 9 a.m. up to 4 p.m. the PV power production is higher than the power demand. In such a situation, if the battery was not present, all the PV energy surplus would be fed into the main grid, which is the main issue for these weather conditions. This is disadvantageous for the MG, because of the renewable energy loss. Moreover, it is also a drawback for the main grid, which is provided with the amount of an uncontrollable energy.

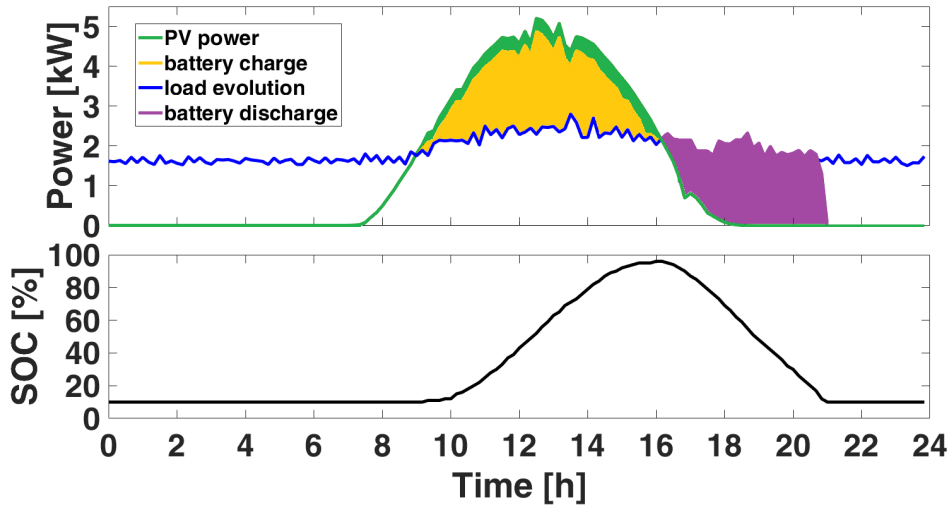

Figure 20: MG operation during a sunny day when ESS is implemented.

However, in the case of the MG under test, a surplus of the generated energy was applied to charge the battery, which was graphed with a yellow area in the Fig.4. It can be seen how the storage contributes to the PV peak shaving.

While the battery is charging, a part of PV energy surplus is dissipated because of the losses caused by the energy conversion and charging (green area), however for the analysed day it was only 3% of the overall daily production. Further, starting from the 4 p.m. when the PV power is not sufficient to cover the demand, the energy stored inside the battery starts to power the MG load. The corresponding battery SoC evolution has been graphed in the lower part of the Fig.20. When the PV power plant was not able to produce electricity and the battery was discharged, the load demand was covered by the main grid. For the analysed day the total daily load demand was of 45 kWh, of which 18.3 kWh were fed instantaneously by the PV generator, 7.5 kWh were stored and supplied, shifted in time, by the battery. Finally, 19.1 kWh were drawn from the main grid. The MG was energy self-balanced for about 13 hours.

2.2.2 *MG operation during a cloudy day*

During a cloudy day, the PV power curve is characterised by sharp variations which result in an occurrence of peaks and lows. In such weather

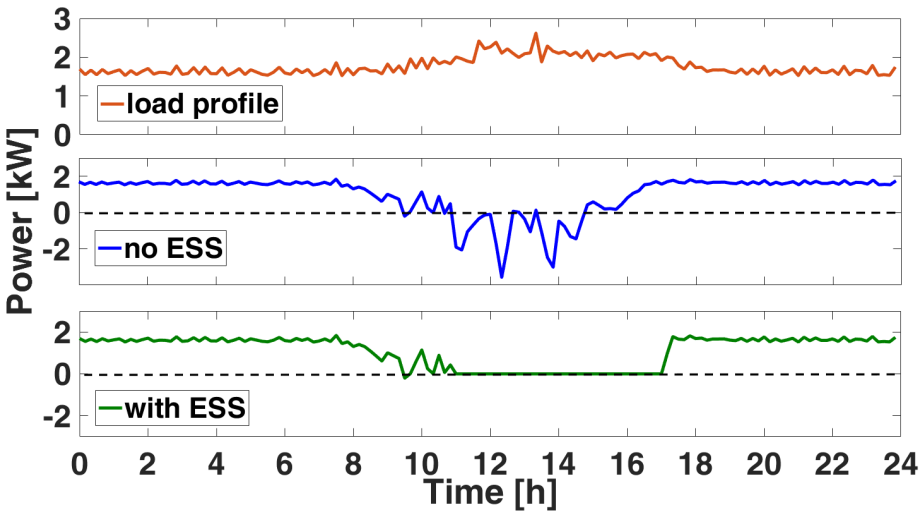

Figure 21: Load profile and the energy exchange between the MG and the main grid with and without the ESS.

conditions, the impact of PV generator on main grid has been shown in the Fig.21. The load profile has been graphed with the orange curve. The blue line demonstrates the power exchange between MG and main grid that occurs when no storage is implemented. The positive values represent the power drawn from the main grid, while the negative ones, the power fed into the grid. As expected, during the central day hours when the PV generation is high, the renewable energy exceeds the instantaneous demand and energy surplus occurs.

However, due to cloudy sky conditions, the energy generation is not constant, which causes transitions of the residual power through the zero value. Such alterations in the energy absorption and delivery, from and to the main grid, negatively affect the power quality. The green line in the lowest part of the Fig.21 demonstrates the condition obtained within the analysed MG. The implementation of ESS allows smoothing of the residual power curve since the PV power surplus is no longer fed into the main grid, but it is drawn by the battery in the charging process. It can be hence observed the positive impact that the MG has on the integration of the RES with the main grid.

The more detailed picture of the energy fluxes within the MG during the cloudy day has been illustrated in the Fig.22. The PV power surplus that has been fed to the ESS is marked with the yellow area in the upper part.

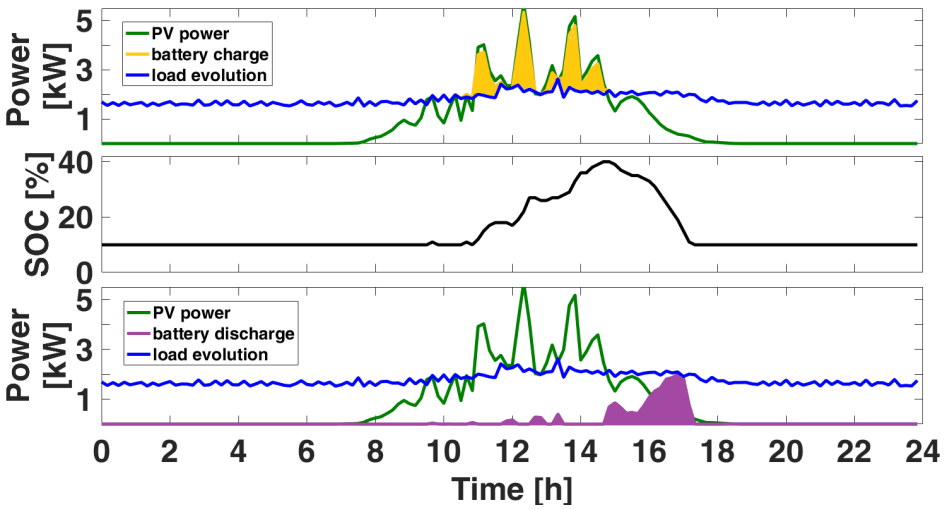

Figure 22: MG operation during a cloudy day when ESS is implemented.

The battery discharged when the PV generation was not sufficient to cover the load, which was depicted with the purple colour in the lowest part. The corresponding variations of the SoC can be observed in the central part. It can be noted that during the analysed day the battery SoC has not exceeded the 40%. The total load demand was of 42.6 kWh of which 12.6 kWh supplied by PV, 2.8 kWh fed from the battery and 27.1 kWh powered from the main grid. The MG was self-balanced for about 6 hours.

2.3 LONG TERM RESULTS

The MG under test has been monitored since November 2016. The measurement campaign concerns load profile, PV generation, battery charging and discharging. A particular attention has been paid on the impact that the ESS has on the system and on the PV peak shaving. Moreover, the energy exchange between the MG and the main grid has been monitored. It is worth to underline that, due to different research activities carried out in the Technology Park, some interruptions in the MG operation have occurred. During the monitoring period the data have been collected for 164 days. The obtained results have been described below.

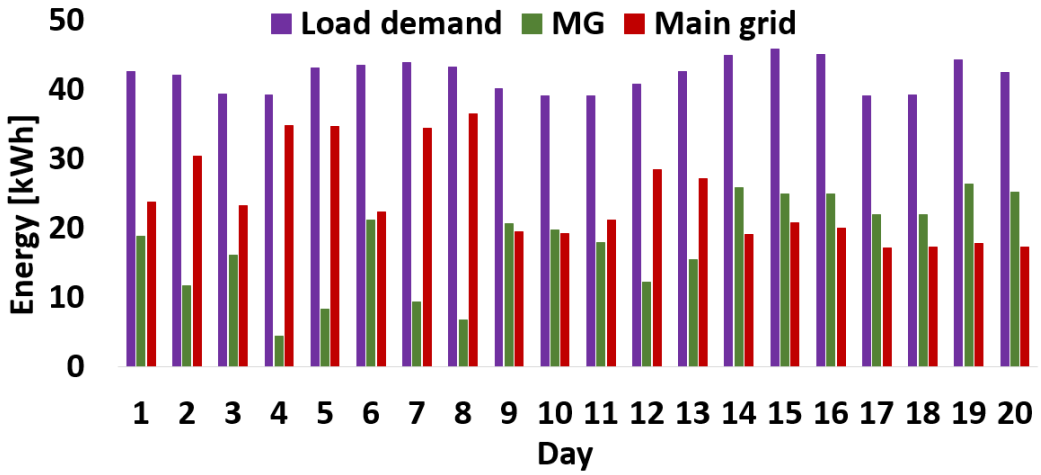

Figure 23: Bar graph representing the MG daily load demand (in purple) covered by the MG sources (PV+ESS, in green) and by the main grid (in red). Data sampled for February 2017.

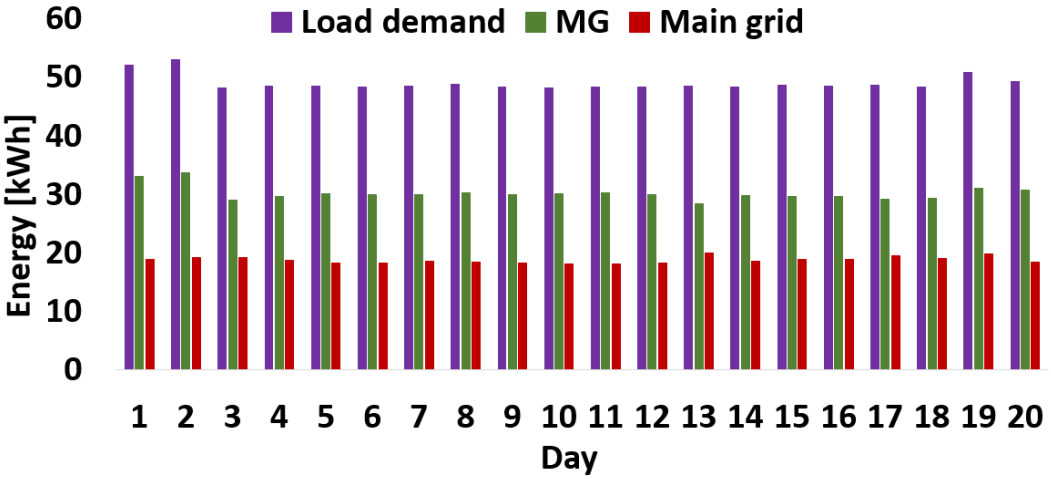

Figure 24: Bar graph representing the MG daily load demand (in purple) covered by the MG sources (PV+ESS, in green) and by the main grid (in red). Data sampled for August 2017.

Month	N° of days sampled	Load demand supply source [%]		
		PV	Battery	Main grid
November 2016	8	28	13	59
February 2017	27	32	11	57
March 2017	30	41	15	44
April 2017	30	43	16	51
May 2017	31	50	15	35
June 2017	18	50	14	36
August 2017	20	46	15	38

Table 5: Percentage of the MG load demand covered by PV, battery and the main grid for different months.

2.3.1 *MG performance*

In Fig.23 and Fig.24 the MG performance has been presented for 20 days of February 2017 and of August 2017 respectively. Two distinct seasons have been chosen to better illustrate different energy conditions. Purple bars represent the total daily load for each of the sampled days. Green bars represent the amount of total load covered by MG taking into account the energy driven directly from the photovoltaic generator or from the battery, which however was charged from the same photovoltaic plant. Red bars indicate the amount of total load supplied from the main grid. It can be noticed that for both months the daily load demand values are repetitive. It can be observed that for February the quotes of energy supplied within the MG and from the main grid varies significantly from day to day. The optimization of the MG control strategy in such conditions is challenging and request an accurate weather forecasting.

For the sampled month, the MG load was covered for 43% from the renewable source (photovoltaic generator supported by the battery) and the remaining 57% of the demand was supplied by the main grid. It is worth to note that if the battery was not present, the photovoltaic generator would have covered only 31% of the demand. As far as August is concerned, a very stable condition of the load supply has been recorded. For each of the sampled days, the rate of the energy generated and consumed within the MG has exceeded the energy absorbed from the main grid. In fact, 61% of the load demand was internally satisfied by the MG sources and the main

grid fed the load only in 38%. The results of the long-term monitoring for the percentage of the MG load covered by different sources have been presented in Tab.5. The percentage covered by PV and ESS has been presented separately in order to better point out the impact of the storage, yet the battery was always charged by the PV source. It can be noticed that the percentage of the load supply from the battery has not varied significantly for different months. On the contrary, the contribution of PV has undergone significant variations, from 28% for November up to 50% for May and June.

Consequently, the main grid has contributed to loads supply mainly in winter months, reaching the peak value of 59% in November. On the other hand, the lowest percentage of demand covered by the main grid was registered in May, with the value of 35%. On the basis of these considerations, the possibility of the planning of services that the MG could offer to the main grid, and energy exchange among the analysed MG and other MGs of the Technology Park could be evaluated.

2.3.2 *PV self-consumption and MG self-sufficiency*

The PV self-consumption indicates the amount of the energy generated by PV that is consumed internally within the MG and hence, not fed into the main grid. In particular, for the analysed case, if the self-consumption was 100%, all the PV energy would have been applied to power the MG loads or to charge the battery.

In Fig.25 and Fig.26 the PV self-consumption rates have been presented respectively for February and August. The blue bars represent the PV self-consumption for the analysed MG, where the ESS has been implemented, and are based on effectively measured data. The red bars report the estimated data for the same MG without considering implementation of the ESS. It can be noticed that, due to lower solar irradiation, the average monthly PV self-consumption quote for February (95%) was significantly higher than the one for August (67%). Such high rates were possible thanks to the implementation of the storage system. In the conditions when no ESS was implemented, the corresponding PV self-consumption quotes would be of 70% and 49%. Analogous data have been presented for every sampled month in Tab.6.

The obtained results demonstrate that the MG supported by ESS allows better integration of the PV power plant with the grid. Moreover,

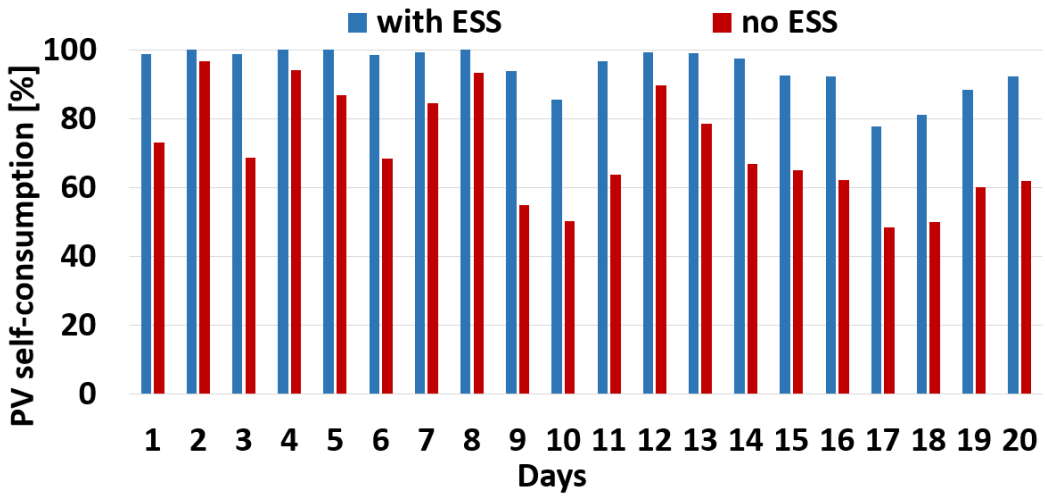

Figure 25: PV self-consumption quotes with and without ESS. Data sampled for February 2017.

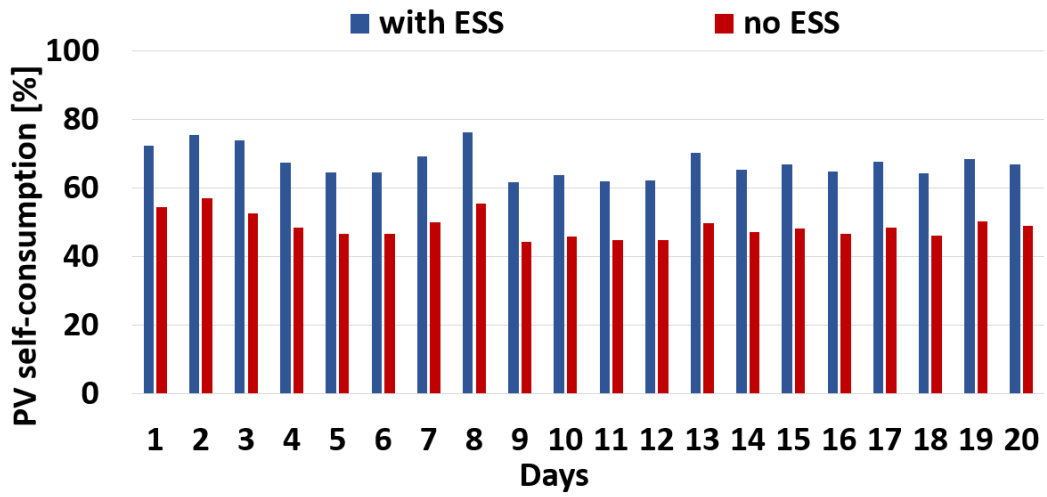

Figure 26: PV self-consumption quotes with and without ESS. Data sampled for August 2017.

Month	N° of days sampled	PV S-C rate [%]		MG S-S degree [%]	
		with ESS	no ESS	with ESS	no ESS
November 2016	8	99	70	41	28
February 2017	27	95	71	43	31
March 2017	30	81	58	56	41
April 2017	30	76	54	59	43
May 2017	31	71	53	65	50
June 2017	18	68	52	65	50
August 2017	20	67	49	62	46

Table 6: PV Self-Consumption (S-C) rate and MG Self-Sufficiency (S-S) degree for sampled months.

the high self-consumption rates within the analysed MG confirm a correct sizing of the PV power plant with respect to the load. Except for the self-consumption, Tab.6 reports the second parameter relative to the MG operation efficiency, which is the self-sufficiency degree, defined as the percentage of the load demand that was possible to cover by internal MG resources (PV supported by ESS). The higher self-sufficiency is, the less energy MG has to draw from the main grid. The highest average monthly values have been recorded for May, June and August (65%, 65% and 62% respectively). As expected, the values calculated for the same MG without the support of ESS have been lower and never exceeded the 50%. These results could be applied for the scheduling of the MG operation time in the islanded mode, which could be planned especially for the months when the MG self-sufficiency rate exceeds 60%.

2.4 ECONOMIC EVALUATION OF THE MG

The economic feasibility is the factor that goes beyond the technical aspects and strongly affects the MGs development. There are different ways to evaluate the MG cost-effectiveness, which may vary with the MG scale, power generator type and rated power, load profile, storage technology and size. Moreover, the incentives, feed-in tariffs or financing programs could significantly modify the perception of the economic profitability of the MG. The considerations presented in this chapter are limited exclusively to the MG of the case study. It is worth to underline that the evaluation is based

exclusively on the incurred costs and the energy savings, without considering any incentive tariff.

In the analysed period of 164 days, the total load demand was of 7680 kWh. The MG sources (PV, ESS charged from PV) have supplied 4404 kWh. The remaining 3276 kWh were covered from the main grid, mainly from the evening to the morning hours. This means that, thanks to the development of the MG, the costs of the net energy purchased from the grid have been reduced of 57%. The initial investment cost of the infrastructure is mainly given by a PV generator, ESS, inverter and the MG management system. It is important to point out that the PV generator has to be sized by taking into account not only loads, but also the additional power needed to charge the battery. At the end of 2016 the Si-based rooftop PV power plant turnkey cost was of 1270 € per kW for the plants characterised with the rated power below 100 kWp [71]. According to International Renewable Energy Agency the Li-ion batteries cost in 2017 is of 300 € per kWh [72]. Cost of the 10 kVA inverter able to manage the energy within the MG together with the current-voltage probes is of 1300 €. Following these considerations, at present, the initial investment for the infrastructure presented in this chapter could be estimated for about 15000 €, of which the PV generator constitutes the main cost share. A convenient methodology to compare the effective cost of different energy generation technologies is a Levelized Cost Of Energy (LCOE), calculated as the summary cost of the infrastructure over its lifetime, divided by its total energy produced in the life cycle. The summary cost of the plant takes into account not only the initial investment, but also costs of the maintenance, assistance and operation during the life cycle [73]. Considering the value of the annual global solar irradiation available in the southern Italy, which is of 1600 to 1700 kWh/m2 [74], the LCOE of the PV generated electricity for the residential plants is reported to be in range between 0.0853 – 0.1268 €/kWh [75]. On the basis of the available data obtained from the monitoring of the MG and the lessons learned during its maintenance, the LCOE of the MG has been evaluated. Two scenarios of the MG lifetime have been assumed, 20 and 25 years respectively, deriving from the normally expected life cycle of the PV power plant. The first LCOE analysis takes into account exclusively the presence of the PV generator. The second analysis considers the integration of the PV power plant with the ESS within the MG. The details of the costs taken into account for the LCOE calculation have been presented in the Tab.8.

It is worth to underline that the price of the inverter in the case of MG is higher. It is due to the energy management system that is comprised

Month	N° of days sampled	PV S-C rate [%]		MG S-S degree [%]	
		with ESS	no ESS	with ESS	no ESS
November 2016	8	99	70	41	28
February 2017	27	95	71	43	31
March 2017	30	81	58	56	41
April 2017	30	76	54	59	43
May 2017	31	71	53	65	50
June 2017	18	68	52	65	50
August 2017	20	67	49	62	46

Table 7: Costs incurred for the realisation and O&M for the PV power plant and for the MG. Two different temporal scenarios have been considered.

within the inverter, except of its normal function of AC/DC converter. In both cases, the replacement of the inverter after 15 years of performance has been assumed. The PV power plant degradation rate has been assumed as 1% per year. This results in the energy production values of 179416,3 kWh and 218912,6 kWh respectively over 20 and 25 years of the PV operation. The PV cleaning price used for the calculation is of 0.61 €/m2 and it is the real cost sustained currently by the Technology Park to clean the plant manually. Moreover, the maintenance cost over the PV plant lifetime has been estimated as 1% of the total plant cost, while for the case of MG the respective cost has been assumed as 2%, due to higher technological complexity of the system. Finally, for the MG case the cost of the MG in terms of Li-ion battery has been considered and the replacement after 6000 cycles, which correspond with 15 years of operation, has been assumed.

2.5 CONCLUSIONS

The results obtained in this chapter reveal the potentiality of an MG characterised by the presence of the PV generator, Li-ion battery ESS and the energy management system. In particular, the implementation of the ESS permits MG to be largely independent of the main grid, especially in the case of sunny days, when the battery charging from the PV generator can fully take place. Moreover, the developed MG has demonstrated also a better integration of the PV power plant with the main grid, since it extends the time span when the energy exchange between the MG and the main

Cost item	**LCOE of the PV power plant**		**LCOE of the MG (PV + ESS + EMS)**	
	20 years	**25 years**	**20 years**	**25 years**
PV plant	9906	9906	9906	9906
Inverter	2x1000€	2x1000€	2x1300€	2x1300€
ESS	-	-	2x4000€	2x4000€
PV cleaning	6393€	7991	6393	7991
O&M	1191€	1191€	4101€	4101€
LCOE [€/kWh]	**0.1086**	**0.0963**	**0.1728**	**0.1489**

Table 8: Costs incurred for the realisation and O&M of PV power plant and MG. Two different scenarios have been considered.

grid does not occur. Several months of the monitoring have revealed also the significant improvement of the PV energy self-consumption rate when the generator is a part of the MG. The analysis of the system performance demonstrates its feasibility, the economic evaluation, however, reveals that the cost of development and maintenance of the MG might be still an important impediment for the wide implementation of this technical solution. Nevertheless, the cost of the Li-based storage system has undergone a significant decline in the past years and it is expected that this trend is going to continue, which can have a positive impact on the MGs development. Moreover, the MG could offer services to the main grid or support other MGs, which brings out the possibility of the economic income. Finally, the analysis of the case study has demonstrated that the LCOE of such an MG decreases with the increase of the system lifetime, despite the costs of operation and maintenance.

3

MICROGRID POWERED BY CPV SYSTEM: CASE STUDY

The Concentrator Photovoltaic (CPV) technology, due to its high energy conversion efficiency, represents a promising solution for supporting the growth of Microgrid (MG) concept in the domestic and public buildings, especially in sunny regions. The intermittent characteristic of photovoltaic power production, magnified in CPV power plants, can be mitigated by means of properly sized implementation of Energy Storage System (ESS) that permit, at the same time, the improvement of MG energy management and power quality. In order to evaluate the control and sizing criteria of CPV and ESS within MGs, considering the different time evolution of load profiles, a test bench suitable to analyse MGs powered by CPV has been developed. The functionality of such an MG has been monitored in real operating conditions. The experimental results have revealed that the proposed test bench is a useful tool to validate the design and the control algorithms of MG components considering different daily time evolution of electricity demand. Moreover, it allows the development of innovative solutions for larger scale systems as smart grids.

Regarding the RESs, the rapid grow and development of technologies related to solar energy conversion, has made PVs one of the most reliable and efficient renewable generation system, particularly suitable for MG. In particular, the concentrator photovoltaic is at the present time the most efficient solar energy conversion technology characterised by an efficiency that has exceeded 43% and there is still room for improvement [34, 35]. The commercial energy conversion efficiency for CPV systems is much beyond the highest obtainable efficiency of traditional Si-based PV modules. A typical CPV module is composed of optical elements, such as lenses or mirrors, which focus DNI on small size solar cells, that generate current under the solar light. Usually, CPV modules are mounted on solar trackers which orient the modules surface towards the sun during the day, in order to capture the direct component of solar irradiation [36, 37]. The worldwide experiences developed on this technology have demonstrated that CPV power plants represent a promising solution for renewable energy generation, particularly for those regions with high annual DNI values that makes the levelized cost of electricity of CPV equal to that of traditional PV,

but with a significant reduction of the collecting area involved [38, 76]. Regions with high annual irradiation such as north Africa, south Africa, or Australia are suitable for making economically sustainable the CPV. As far as Europe is concerned, a CPV technology can be implemented in southern areas, such as Spain, Greece, Cyprus or Italy (e.g. Sardinia) due to suitable annual DNI values. The recent development of flat plate CPV technologies characterised by the use of micro-motor, adopted for moving the lens inside the flat CPV panel, in order to have the tracker integrated into the panel and make them similar to the traditional Si-based PV modules. In this future prospective the CPV becomes an interesting solution for energy generation in domestic and building MGs too. Nevertheless, CPV has also some important drawbacks. It is often mentioned that the modules require frequent cleaning, especially in some specific sites and that the tracking system has to be very accurate in order to guaranty the energy production. Moreover, as the CPV systems use only the direct component of the solar irradiation, strong variations in the energy production occur during the day, because the direct irradiation alterations are more frequent and marked respect to those of the global irradiation. For this reason, also the generated power from CPV tends to vary a lot during a day, switching from peak to zero values in a short time span.

Fig.8 shows a typical daily CPV power generation profile registered in the southern Italy. This intermittence is disadvantageous when the CPV is integrated with the main power grid. Also for the MG fed with CPV, such rapid variations in energy generation are difficult to manage, leading to significant fluctuations in the power supply. Consequently, the MG powered by CPV and operating in grid connected mode should be strongly balanced with the contribution of the main grid. However, it can be very challenging task to energetically balance MG supplied by CPV when operating in islanding mode.

In order to mitigate this behaviour and to optimise demand response profiles within the CPV supplied microgrid, an implementation of an ESS coupled with CPV power plant could be considered as a solution. An ESS could on one hand support the microgrid in operating independently from the main power grid, on the other hand it would promote a stable and secure integration of CPV technology with the main grid. The employment of an ESS within a microgrid could be advantageous as, if properly managed, it could lead to an increment of the self-consumption rate of power generated by CPV plant. Further, an implementation of an ESS would raise the cost effectiveness of the renewable energy, bringing out also the possi-

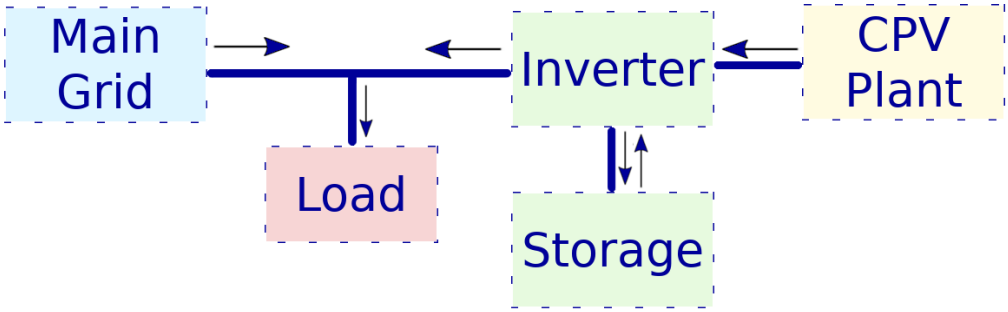

Figure 27: Block diagram of the developed microgrid test bench.

bility to offer services to the main power grid. In order to be able to verify the control algorithm and the sizing criteria of MG supplied by CPV a test bench characterised by the possibility of imposing different time evolution of daily load profile is mandatory. This chapter reports on the characteristic of test bench developed for the assessment of a microgrid supplied by a CPV power plant and supported by a Lithium Iron Phosphate battery. In order to highlight the flexibility of the designed test bench, are reported the experimental results regarding different time evolution of daily load and considering the real CPV power plant production.

3.1 TEST BENCH DESCRIPTION

The proposed test bench has been designed with the aim of achieving a flexible experimental platform, suitable for evaluation and validation of novel MG energy management control algorithm. In particular, the test bench has been adapted in order to assess the performance of MG supplied by an integrated system consisting in a CPV and electrochemical ESS.

3.1.1 *Test bench configuration*

The test bench has been developed at the Technology Park of Sardinia where a 6.2kWp CPV power plant has been installed. The CPV generator has been interconnected with a 9.6kWh electrochemical ESS.

Fig.27 shows the block diagram of the developed test bench where the marked arrows show the allowable energy transactions. In order to experimentally reproduce within the test bench the different time evolution of load profiles, a programmable AC electronic load has been installed.

Figure 28: CPV power plant (top) and MG test bench (bottom).

The adopted configuration allows to evaluate the operation of microgrid test bench components as well as the stability and reliability of the whole system. The final configuration of the installed test bench is shown in Fig.28.

The technical data of main components are reported in Tab.9.

On DC-side the inverter is coupled both with the CPV power plant and the ESS. The ESS is composed of Iron Lithium Phosphate batteries. It is worth to underline that the test bench is connected to the main grid, in order to guarantee the load supply even if the energy generated from CPV and stored in the battery is not sufficient to cover the demand. In addition, if the instantaneous power generated by CPV is greater than the load demand, the battery charge can occur depending on its SoC. Otherwise, the MG energy surplus is delivered to the main grid. The energy management of MG is performed by means of voltage, current and power measurement developed by appropriate sensors, properly installed and interfaced with the control board.

CPV	
P_{mpp} evaluated at $850 W/m^2$	6 kWp
I_{sc}	8.5 A
V_{oc}	800 V
I_{mpp}	7.6 A
Efficiency	23.5 %

ESS-Lithium Iron Phosphate battery	
Total Capacity	6 kWh
N° of cycles (@ 80% rest capacity)	6000
Max output power	4.9 kW
Rated voltage	410 V

Inverter	
Max input DC PV power	6.6 kW
Max input DC voltage	950 V
Min input voltage	180 V
Max input current	2 x 12 A
Power rating	6 kVA
Max efficiency	96.1 %

Three-phase electronic load	
Rated power	30 kVA
Rated current	3 x 40 A
AC max rated voltage, CH-N	0-277 V_{rms}
Frequency fundamental current	10-400 Hz

Table 9: Technical specification of the main components of the presented test bench.

3.1.2 *Control strategy*

The control strategy adopted by the inverter is the same as described in Chapter 2 Section 2.2 considering, in this case, the value of P_{CPV} instead of P_{PV}.

3.2 EXPERIMENTAL VALIDATION: CASE STUDIES

The Power Quality impact of the proposed mg configuration on the main grid, related to the integration between CPV power plant and lithium ESS, has been evaluated with the developed test bench. Tests have considered different time evolutions of the mg load demand, representative of different case studies.

The daily power evolution of each case study has been depicted in Fig.29, in which the legend shows the values of daily energy consumption associated to each Case A (42 kWh) and Case B (57 kWh).

3.2.1 *Case study A: public building*

The case study A has been defined by referring to the load profile recorded in the building hosting the test bench. In particular, in the case study A the

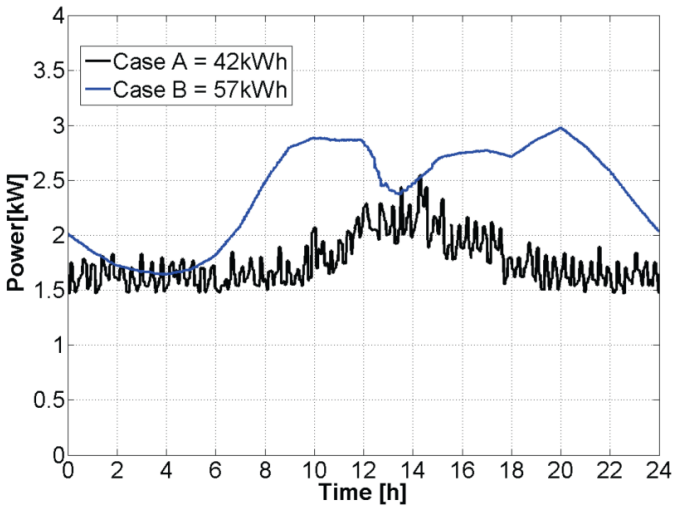

Figure 29: Daily time evolution of power demand for the tested case studies.

electricity demand has been set in order to replicate the load time evolution of a typical working day in an edifice hosting both offices and laboratories. It can be observed that the load profile is very rough. The daily demand is characterised by a peak value of 2.6 kW. Moreover, the power consumption never drops to zero value, even during the night, due to the presence of lighting systems and other types of equipment that require a continuous supply. The monitoring of the test bench, reproducing the MG in this operating condition, has pointed out different effects on the power quality of the grid depending on the combination among time evolutions of CPV, battery and load power profiles. In order to investigate the above-mentioned effects for case A, two days with different CPV production conditions (a clear sunny day and a partially cloudy day) are reported and discussed.

In Fig.30 the power daily evolution of CPV and load measured during a sunny day with clear sky are reported. As can be observed, in the presence of solar resource, the total load demand is covered by the CPV generation. However, only 40% of the daily generated energy is self-consumed in the MG. The remaining 60% of daily CPV production is fed into the main grid. On the other hand, if the ESS of the test bench is activated the CPV overproduction is partially stored.

In Fig.31 the CPV overproduction (evidenced by a green area), that is used for charging the battery with the corresponding SoC variations are

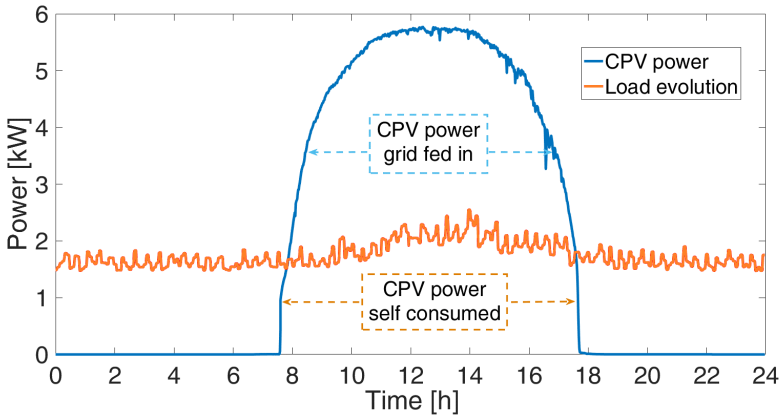

Figure 30: Daily CPV power production and load evolution on a sunny day.

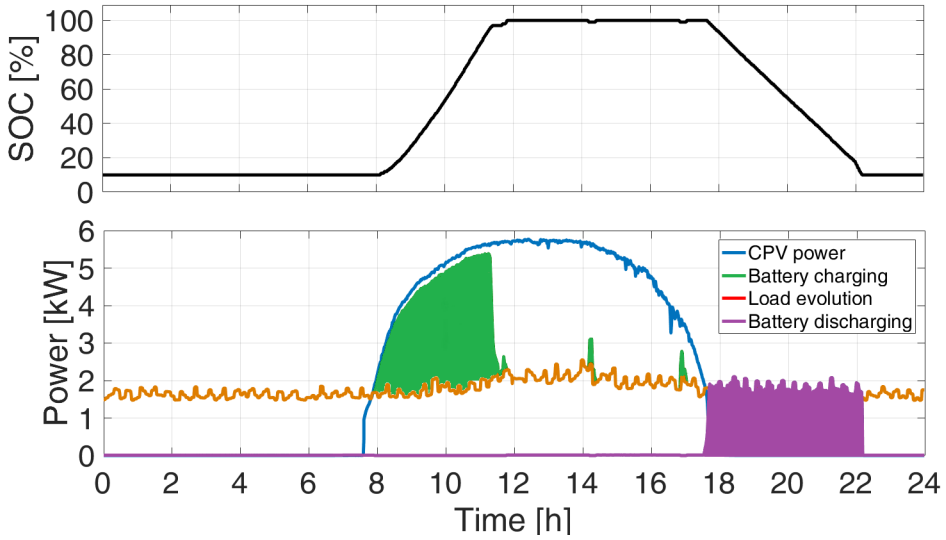

Figure 31: Daily battery SoC time evolution on a sunny day (top), CPV power profile and load evolution, with battery charging and discharging power profile (bottom).

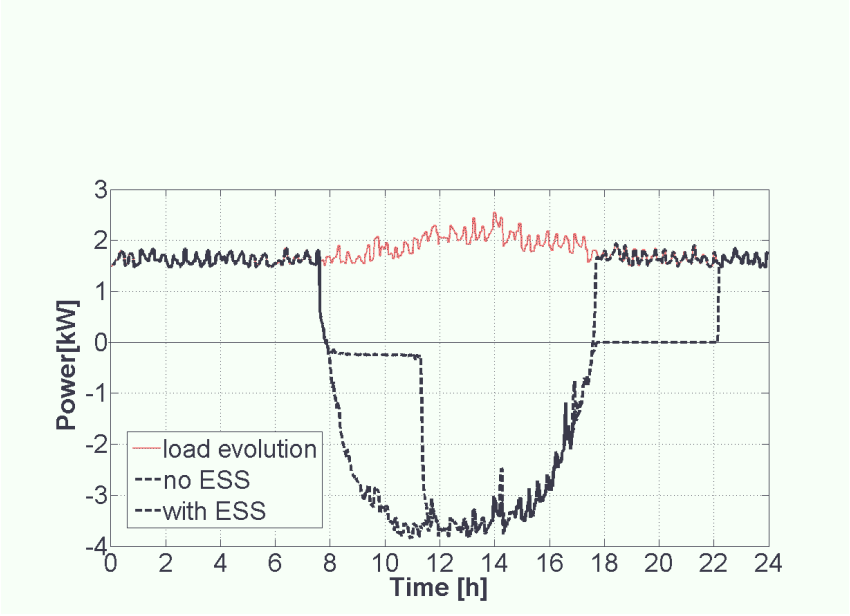

Figure 32: Daily residual power exchanged between MG and the main grid, with and without the presence of ESS.

shown. In such weather conditions, the ESS takes about two hours to charge the battery from the SoC value of 10% to SoC of 100%. The energy stored in the battery is further used to power the load after the sunset for an additional four hours as shown in Fig.31 by the battery discharging curve (evidenced by a purple area).

Nevertheless, it is worth to underline that in such weather conditions, only the 56% of total CPV energy production has been self-consumed. Therefore the remaining 44% has been fed to the main grid. In order to analyse the effects of the MG on power quality, the residual power representing the exchange between MG and the main grid have been recorded and reported in Fig.32. Particularly, in order to compare the MG behaviour in term of power quality, the residual power of MG with and without the ESS are reported (black and blue dotted curve respectively) .

Positive values represent the instantaneous power provided by the main grid, while negative values represent the delivered one. It can be observed that the power production can easily cover the load demand during sunny hours and there is still a high percentage of generated energy available for feeding in. Regarding the power quality, the comparison between the MG residual power with and without ESS, shows an improvement when the

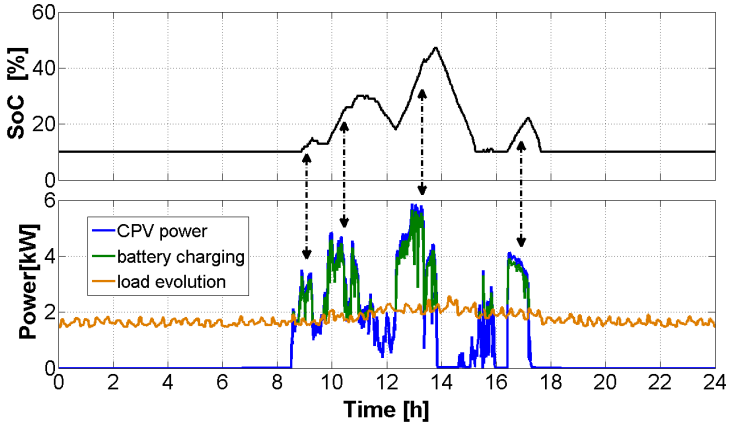

Figure 33: Daily SoC time evolution (top) and CPV production (bottom), on a partially cloudy day.

residual power assumes a zero value due to the reaching of the neutral condition of the MG. However, when the ESS SoC reaches its limit values (10% & 90%) the MG behaves as if it would not have any ESS. The situation changes for different weather conditions.

Fig.33 reports in the lower part the daily evolution of the CPV, battery and load power profiles measured during a partially cloudy day. Whereas the corresponding SoC evolution is reported in the upper part. In this case, the MG self-consumption is around 11 kWh, representing the 60% of the total daily energy CPV production. The remaining 8 kWh of the daily CPV production led to a partial charge of the battery, as can be observed in Fig.33 by the rising of SoC.

The grey areas highlighted in Fig.34, represent the part of the stored energy that has been used for covering the load demand when the energy from CPV was not present or not sufficient. The amount of load consumption covered by energy stored in the battery is 5.1 kWh, while 1.7 kWh has been fed in by the main grid. If the ESS was not present, in the same weather conditions, the total amount of 8 kWh overproduction would be grid fed in and the self-consumption quote would be of 64%. The implementation of the battery storage increased the self-consumption quote up to 91%. Similar considerations, on the variation of the quote of self-consumption, have been made on all available days of the monitoring by

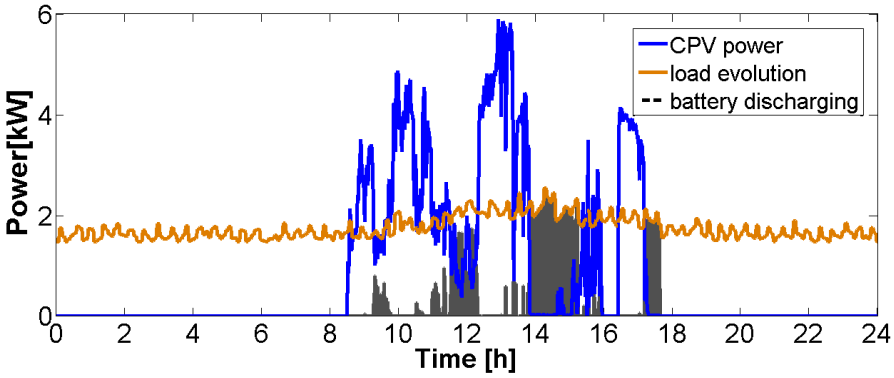

Figure 34: Daily CPV power production, demand and battery discharging evolution on a partially cloudy day.

considering the profile of case study A. Data related to these considerations are discussed in section 3.3 of this chapter.

Finally, in Fig.35 are shown the comparison among the energy exchange between the MG and the main grid with and without ESS (blue and black curve respectively), as well as the evolution of the load profile (orange curve). Such representation highlights the improving effect of the ESS on power quality. In fact, the residual power of MG without ESS presents many transitions through zero, that mean many changes between absorbing and delivering energy condition that negatively affects the power quality. On the other hand, the residual power of MG with ESS is much more smooth at least between 8.OO a.m. and 3.00 p.m. Even if the positive effect of the ESS can be observed, the experimental results indicate that the control strategy of the system can be optimized.

3.2.2 *Case study B - Typical italian load profile*

The power profile of case B reproduces a typical load profile recorded in Italy. As can be observed, higher power values are present between 9.00 a.m. and 12.30 p.m. Starting from 6.00 p.m. another increase is registered up to a peak value of 3 kW.

Fig.36 shows the daily evolution of the CPV power and load evolution of case study B during a partially cloudy day in the lower part, the corresponding SoC evolution in the upper part. The total CPV production of the day was of 32 kWh, of which 60% has been used for covering the daily power demand and the remaining 30% led to a partial recharging of the

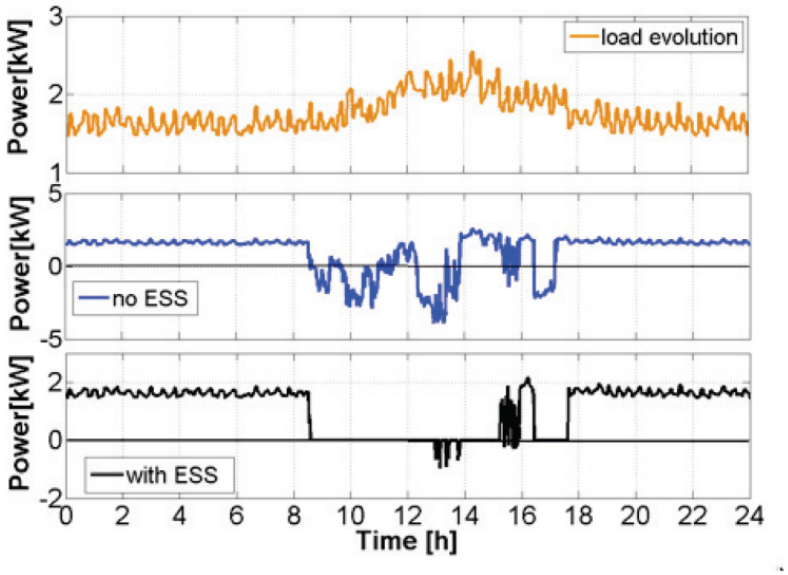

Figure 35: Daily energy exchange between the MG and the main grid with and without ESS.

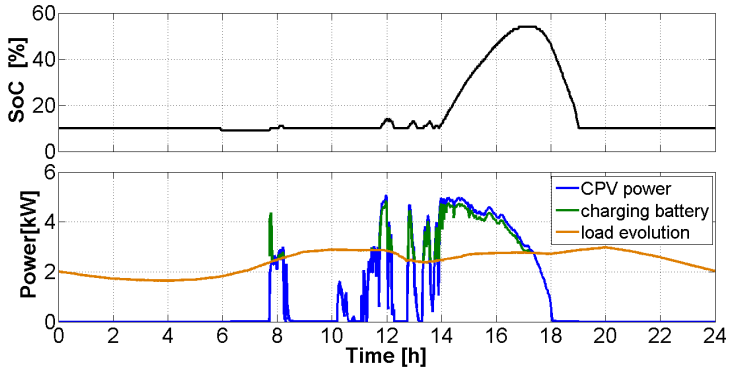

Figure 36: SoC evolution (top) and daily CPV power production together with load and battery charging evolutions (bottom) on a partially cloudy day.

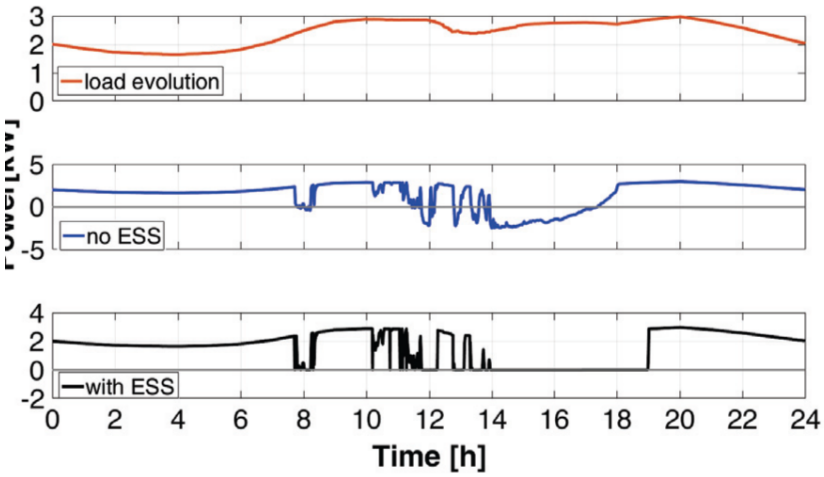

Figure 37: Daily residual power between the MG and the main grid with and without ESS (blue dotted line and black dotted line respectively, during a partially cloudy day.

battery up to SoC value of 54%, as shown by the SoC evolution in the upper part of the same figure. The total self-consumption calculated for this case with and without ESS are 63% and 86% respectively.

Fig.37 compares the energy exchange between the MG and the main grid with and without ESS (blue and black curve respectively). As can be observed the blue and the black dotted curves appear to be nearly overlapped up to 12.00 p.m. In fact, the very low power production of the CPV is not sufficient to charge the ESS in the first part of the day, so the load demand is totally covered by the main grid also in the case of active ESS. After 12.00 p.m., when the CPV production increases, a partial charging of the battery occurs. The power transitions through zero, remarkable in the case without ESS and shown in the blue curve of Fig.37, are not present in the residual power measured with the MG supported by ESS. This demonstrates the mitigation of the negative effect of alterations in the CPV power production on the main grid.

3.3 LONG TERM MONITORING OF CPV-ESS MICROGRID

In order to better understand the impact of the ESS on the MG supplied by CPV, a monitoring campaign of several days in the spring period

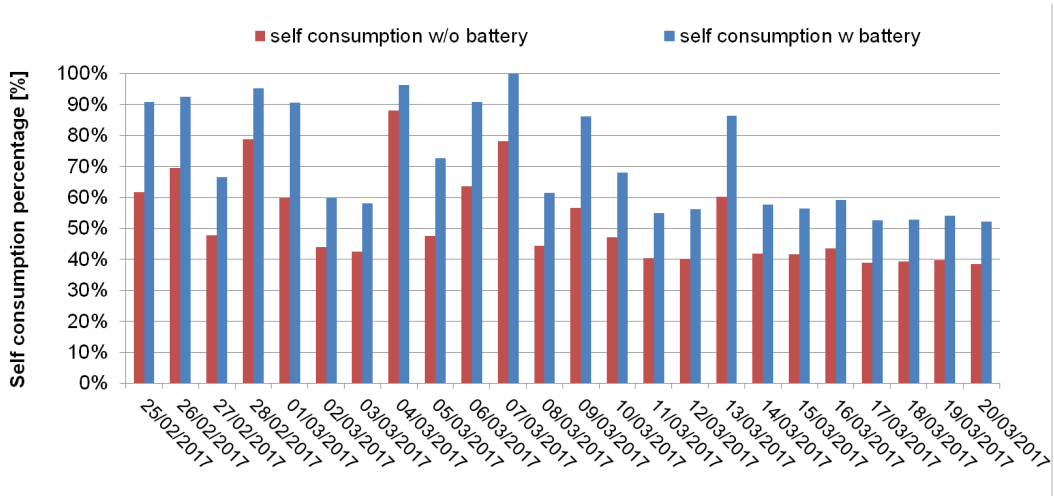

Figure 38: Comparison among the daily self-consumption quote without ESS (red bars) and with ESS (blue bars), calculated for teh same days.

has been carried out. This approach allowed the evaluation of the MG operation in different weather conditions, especially regarding the solar irradiance and consequently the daily energy production from the CPV generator. During the monitoring, the load profile presented in case study A has been applied. The impact resulting from the implementation of the ESS can be evaluated by calculating the quote of self-consumption ($SP_{\%}$) according to (2):

$$SP_{\%} = \frac{EP_{CPV} - E_{FIN}}{EP_{CPV}} \cdot 100; \tag{2}$$

where the EP_{CPV} is the daily energy production from the concentrator photovoltaic generator, and the E_{FIN} is the amount of energy which was not consumed within the MG, and so was fed into the main grid. For each of the test days, the EP_{CPV} has been calculated for both MG configurations: without ESS and with ESS. The results of the calculation of the daily self-consumption quotes are shown as bars of different colours in Fig.38.

The blue bars represent the daily self-consumption calculated considering the support of ESS to the MG, while the red bars are the calculated self-consumption percentage when the ESS was not implemented. As expected, the ESS implementation determines an increase of the self-consumption quote, and such an increase ranges between the 8% and the 31%.

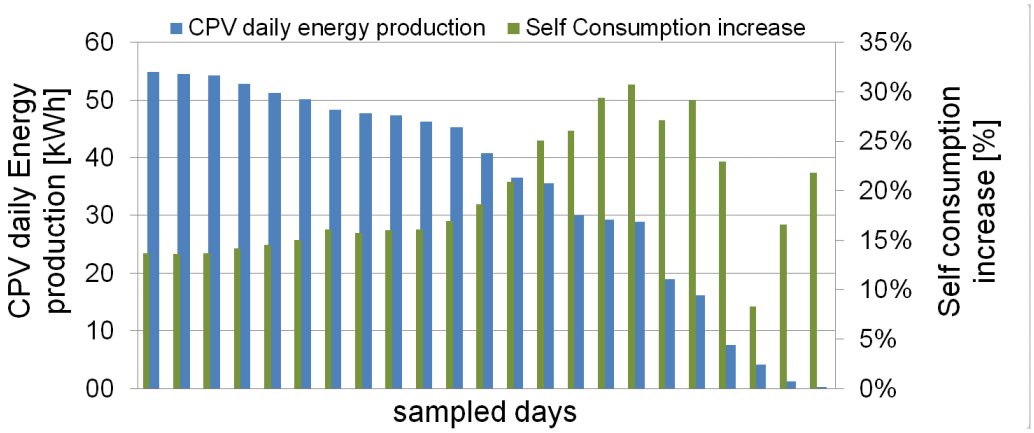

Figure 39: CPV daily energy production (blue bars) with the increase of the daily self-consumption quote, due to the implementation of ESS (green bars).

Fig.39 shows the percentage increase of self-consumption caused by the implementation of the ESS in MG and its correlation with the CPV production. The data are presented by ordering the EP_{CPV} values in decreasing order. The analysis points out that the highest increase in self-consumption has not been registered in the days with higher energy productions but in the partially cloudy days. This confirms the importance of integration between ESS and CPV to improve self-consumption and power quality when the partially cloudy condition occurs. Hence, it is of crucial importance the correct balance between the CPV rated power and the ESS nominal capacity, taking into account also the expected load demand mostly considering the partially cloudy conditions.

3.4 CONCLUSION

In this chapter, a test bench developed for the assessment of MG supplied by CPV generator has been presented. The integration between a CPV system and a Lithium Iron Phosphate ESS has been analysed. Different load profiles have been experimentally reproduced by an electronic load in order to evaluate the energy behaviour of an MG characterised by 6.2 kWp CPV generator and an ESS of 9.6 kWh rating capacity, with regard to the different weather conditions. The effectiveness of the integration between CPV and ESS has been observed both in partially cloudy and sunny days with different daily load profiles. The analysis of different load evolutions

in different CPV power generation conditions highlighted the important role played by the ESS. It has been observed how the presence of an ESS could, mainly in presence of an irregular and low CPV power generation profile, mitigate the negative impact of such CPV production on the grid. The presented test bench proved to be a useful tool for the experimental validation of sizing procedure of the MG components and for testing innovative energy management control algorithm. These considerations were possible thanks to the monitoring of test bench in the real working conditions, where different factors affecting the system operation were observed. However, as to give more details regarding the operation of the CPV supplied and ESS supported microgrid, at least one full year of monitoring would be advisable.

4

ACTIVE FILTERING SYSTEM

In this chapter a specific configuration of energy storage system able to provide, at the same time, the compensation of higher current harmonic components and the management of energy balance between the demand and the generation in MGs, has been presented. In particular, a control algorithm based on a instantaneous power approach has been implemented referring to a 4L-VSI with the aim of integrating the battery energy management with the current harmonic compensation.

The proposed configuration of energy storage system integrated with shunt active filter function is introduced. The control algorithm developed for the management of energy balance and harmonic compensation has been described as the modulation technique used for the 4L-VSI. The battery modelling is discussed in chapter 5. The effectiveness of the proposed approach is tested referring to a non-linear case of study.

4.1 ESS-ACTIVE FILTER CONFIGURATION

Control algorithms used for Energy Management System (EMS) of MG require to decide upon which energy and electrical quantities are necessary to the management. Usually, the electrical reference quantities are measured at the PCC, which represents the interface between MG and power grid. The power quality in this point influences MG's performances [44].

In order to better highlight the effects produced by a wrong management of power quality, in Fig.40 and 41 are shown respectively power and THD measurements referred to PCC of the MG installed in Technology Park of Sardinia (Italy). The building hosts traditional offices and laboratories, which are characterised by a significant presence of non linear electric loads and generators, such as PV plants whose overall rated power is equal to 25kW_p. The monitoring campaigns conducted on the PCC during a sunny day revealed a high correlation between the evolution of MG currents THD indexes and the residual active power. In particular, it has been observed that the worst situation, in terms of THD indexes, occurs during self-balancing energy conditions. This reveals the presence of interaction

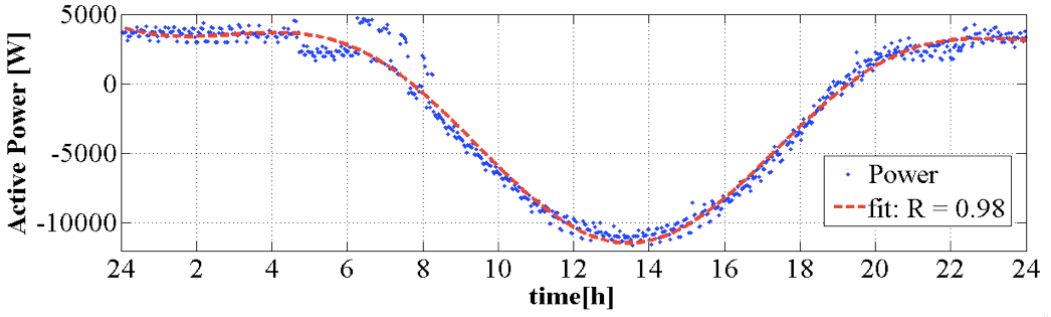

Figure 40: Residual power evolution during a sunny day in the MG of the Technology Park of Sardinia (Italy)

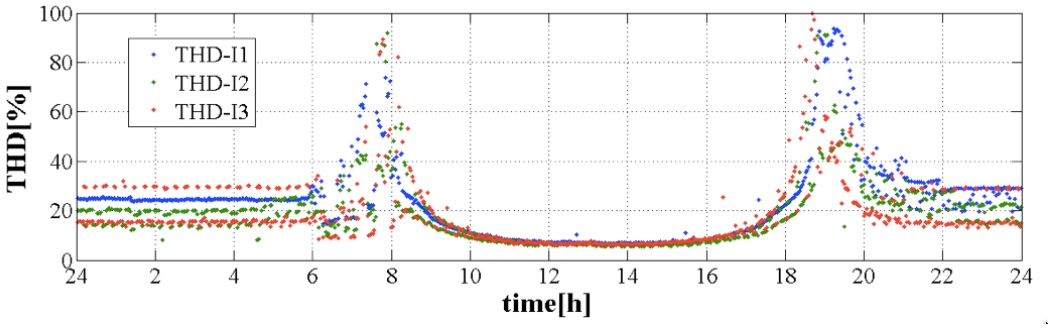

Figure 41: THD evolution during a sunny day in the MG of the Technology Park of Sardinia (Italy)

phenomena strictly connected to the power quality issue, that assume significant importance in proximity of self-consumption, a condition towards which EMS, proposed in technical literature, steered MGs[77].

Hence, harmonic compensation assumes a particular importance for guaranteeing the expected performance in MG when occurs the self consumption condition because of it prevents electric pollution and allows the linearisation of MG behaviour on PCC. This chapter presents an integrated configuration of ESS and shunt active filter.

The aim of this ESS-AFS is to impose equivalent linear load conditions on the PCC, assuring an high quality voltage and power evolution while performing the energy management strategy by means of the ESS.

The ESS proposed in characterised by the use of an electrochemical battery, interfaced to the main grid by means of an energy conversion system made up of two elements: a DC/DC converter used to manage the energy and power flow between the battery and the capacitor DC Bus (or LC

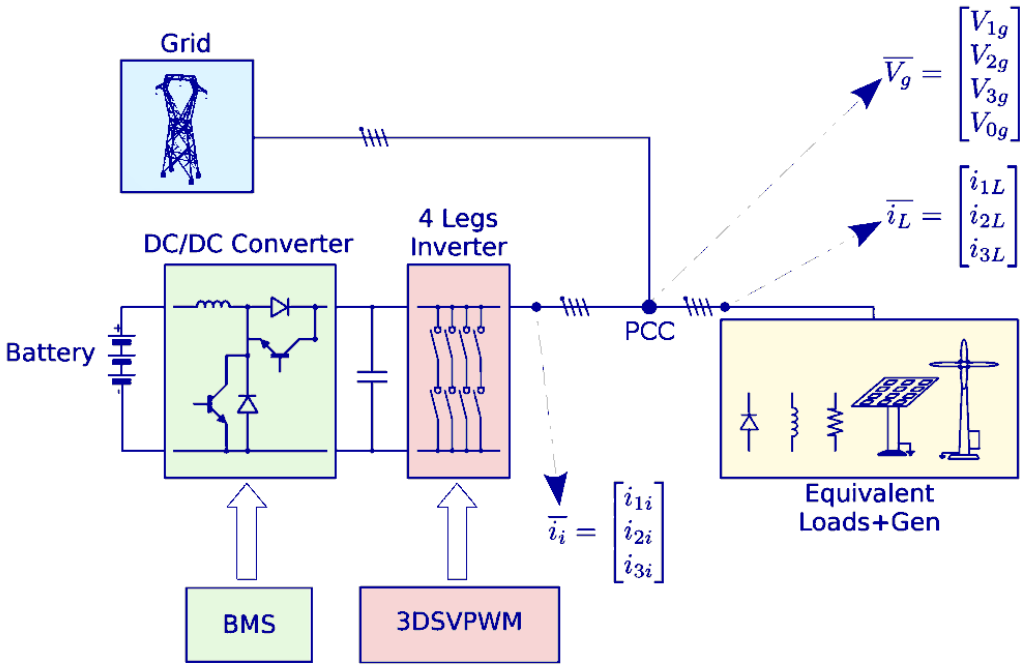

Figure 42: Block diagram of the proposed integrated ESS-AFS

filter, as explained in chapter 6); a four-leg DC/AC power converter. In particular, the use of this kind of inverter is a mandatory choice due to the necessity of developing a system able to both operate as active filter and as energy balancing system, also in presence of three-phase unbalanced MG loads and/or distributed generators [46, 47]. The structure of the above described configuration is reported in Fig.42.

In order to the proposed system manage to perform the above described functions, it has to be properly controlled. For this reason a decoupling control between the functions of active filtering and battery energy managing has been developed. This has been achieved by resorting to an instantaneous power approach, which allows the separation between the active power and the reactive and oscillating one. Based on considerations reported has been implemented the following control strategy.

4.2 INTEGRATED CONTROL OF ESS AND AFS

The control algorithm of the proposed ESS-AFS configuration takes advantage of the intrinsic energy decoupling that exists between the current

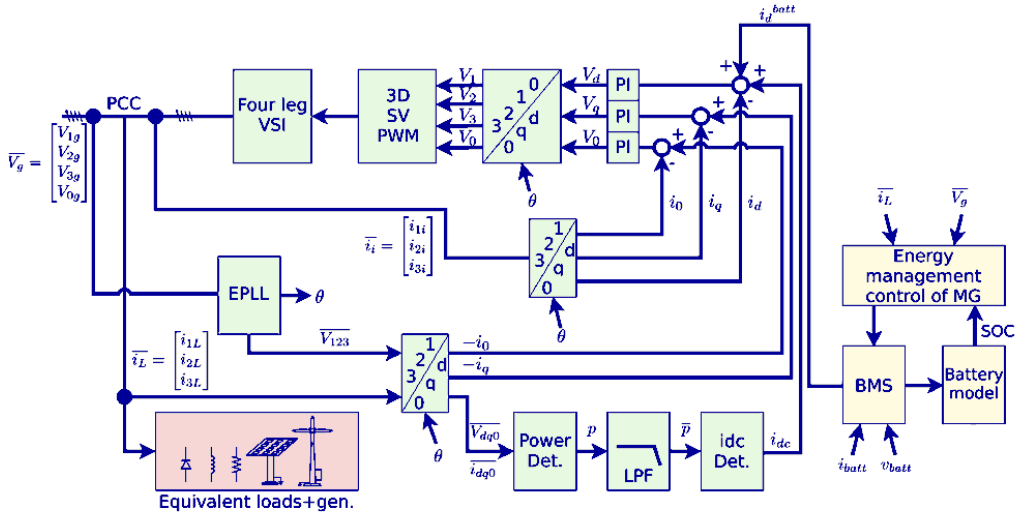

Figure 43: Block diagram of the control algorithm developed in the proposed ESS-AFS

harmonic compensation process and the battery energy management one, when the instantaneous power control approach is applied. As a matter of fact, the implementation of a control algorithm based on Synchronous Reference Frame (SRF) theory and Instantaneous Reactive Power (IRP) management, allows the compensation of current harmonics resorting to the capacitor connected to the DC bus for the IRP balancing. The control of the ESS-AFS is schematically described in Fig.43.

The control algorithm is based on the identification of the instantaneous active and reactive power of the MG at the PCC. This is performed referring the SRF. In particular, has been considered the utilisation of an Enhanced Phase-Locked Loop (EPLL) that allows the accurate determination of the power system voltage phase θ. This allows to apply the Clarke power invariant coordinate transformation in (3) and the Park one in (4) from the stationary reference frame $[a_1 a_2 a_3]^T$ to the SRF $[a_d a_q a_0]^T$, can be performed [78].

$$\begin{bmatrix} a_\alpha \\ a_\beta \\ a_0 \end{bmatrix} = \sqrt{\frac{2}{3}} \cdot \begin{bmatrix} 1 & -\frac{1}{2} & -\frac{1}{2} \\ 0 & \frac{\sqrt{3}}{2} & -\frac{\sqrt{3}}{2} \\ \frac{1}{\sqrt{2}} & \frac{1}{\sqrt{2}} & \frac{1}{\sqrt{2}} \end{bmatrix} \cdot \begin{bmatrix} a_1 \\ a_2 \\ a_3 \end{bmatrix} \tag{3}$$

$$\begin{bmatrix} a_d \\ a_q \\ a_0 \end{bmatrix} = \begin{bmatrix} \cos\theta & \sin\theta & 0 \\ -\sin\theta & \cos\theta & 0 \\ 0 & 0 & 1 \end{bmatrix} \cdot \begin{bmatrix} a_\alpha \\ a_\beta \\ a_0 \end{bmatrix} \tag{4}$$

The application of the Clarke-Park transformation to the measured MG voltages $[v_{1g}v_{2g}v_{3g}]^T$ and currents $[i_{1L}i_{2L}i_{3L}]^T$ allows the evaluation of instantaneous active power p, reactive power q and the homopolar one p_0 as shown in (5).

$$\begin{aligned} p &= v_d i_d + v_q i_q = \bar{p} + \tilde{p}; \\ q &= v_q i_d - v_d i_q = \bar{q} + \tilde{q}; \\ p_0 &= v_0 i_0 = \bar{p_0} + \tilde{p_0}. \end{aligned} \tag{5}$$

The identification of MG average active power $\bar{p}$ is obtained by properly filtering p. Then, it is possible to define on the SRF the compensating current that the AFS has to generate, $[i_{di}i_{qi}i_{0i}]^T$. In (6) the equations to determine the compensating currents are shown. In particular, i_{qi} and i_{0i} are equal to the corresponding components of the MG currents but with inverted sign. In order to calculate the d-current set-point "i_{di}", the $\tilde{p}$ has to be calculated from (5), considering that $v_q = 0$ is equal to zero. The recalled procedure allows to define the compensating set-points of the d-q-o current loops, as expressed in (6).

$$\begin{aligned} i_{di} &= \frac{\bar{p}}{v_d} - i_{dL}; \\ i_{qi} &= -i_{qL;} \\ i_{0i} &= -i_{0L}. \end{aligned} \tag{6}$$

It is worth noting that the average instantaneous active power provided by the ESS-AFS with the current set-points above mentioned, is equal to zero. Moreover, the power exchanged between the MG and the battery can be managed by means of a proper set-point i_d^{batt}, applied to the d-current loop. The evaluation of i_d^{batt} is developed considering the energy

management strategy of the MG and is synthesised taking into account the battery energy and power constraints and its model. The FBM described in chapter 7 is an example of a suitable method for calculating this battery set-point. Subsequently, the d-q-o current set-points are compared to the corresponding MG measured currents and processed by PI regulators. The output of PI regulators define the voltage vector that has to be modulated by the 4L-VSI on the PCC, in order to achieve the imposed MG control strategy.

4.3 FOUR LEG VSI 3D MODULATION

The ESS is interfaced to the PCC by means of a three phase Four-Leg Voltage Source Inverter (4L-VSI). The PWM technique used to control this particular converter topology is the 3D-SVPWM [79]. This approach is based on the definition of the reference voltage $\bar{v}$ by its projection in the $(\alpha - \beta - 0)$ stationary reference space frame, obtained considering the o-axis orthogonal to the $(\alpha - \beta)$ plane. Hence, the reference vector is expressed as

$$\bar{v} = [v_\alpha v_\beta v_0]^T. \tag{7}$$

The four leg switching pattern defines sixteen vector in this space frame (four bits): two zero voltage vectors e fourteen non-zero voltage vectors. Their component on the o-axis are defined by the inverter voltage constraint, represented by the bus voltage V_{bus}. The fourteen non-zero voltage vectors define a space region, hexagonal-prism-shaped and centred in the axes origin. Any different reference vector $\bar{v}$ is generated applying a precise combination of non-zero voltage vectors and zero voltage vector, which depends on the chosen modulation typology, and is associated to a different switching pattern. Hence, the procedure aimed to associate the correct switching pattern to the reference vector $\bar{v}$, starts with the identification of the region in which $\bar{v}$ is located. For this purpose, the hexagonal prism is firstly split in six main triangular prisms that have the o-axis in common. Considering sub-regions bounded by non-zero voltage vectors, each triangular prism can be split in four tetrahedrons, obtaining twenty four regions. Each of the twenty four tetrahedrons define one of the above mentioned switching pattern [79].

Therefore, the identification of the i^{th}-tetrahedron, where the reference vector $\bar{v}$ is located, is fundamental for determining which non-zero voltage

	$\sqrt{(}3)v_\alpha \geqslant v_\beta$	$\sqrt{(}3)v_\alpha < v_\beta$
$v_\alpha \geqslant 0 \wedge v_\beta \geqslant 0$	1	2
$v_\alpha \geqslant 0 \wedge v_\beta < 0$	6	5
$v_\alpha < 0 \wedge v_\beta < 0$	4	5
$v_\alpha < 0 \wedge v_\beta \geqslant 0$	3	2

Table 10: Prism identification cases.

vectors have to be modulated, the resulting switching pattern and for evaluating duty cycles. The sequential procedure for tetrahedron determination is structured as follows. The first step consists in the triangular prism identification. The aim is locating in which sector of the $(\alpha - \beta)$ plane are the $\bar{v}$ components. This is performed by means of a comparison between the above mentioned $\bar{v}$ components v_α and v_β, according to:

$$\sqrt{3}\|v_\alpha\| > \|v_\beta\| \tag{8}$$

Studying the relation in (8) and the sign of v_α and v_β components, allows to identify the prism in which the reference vector $\bar{v}$ is located. Table shows all different cases with the associated prism.

After having determined in which prism the reference vector is located, the next step is the i_{th}-tetrahedron identification. his is performed by analysing the polarity of the set-point voltages in the three phase stationary reference frame $[v_{1n}v_{2n}v_{3n}]^T$. It is worth noting that the grid voltages $[v_{1n}v_{2n}v_{3n}]^T$ are refereed to the neutral point.

Every i_{th}-tetrahedron has been associated to a 3x3 matrix, built considering the projection of the reference vector $\bar{v}$ onto the related non-zero switching vectors. By means of this matrix it is possible to calculate the duty ratios of each non-zero switching vectors as shown in .

$$\begin{bmatrix} d_1 \\ d_2 \\ d_3 \end{bmatrix}_i = \frac{1}{V_{bus}} \cdot \begin{bmatrix} a_{11} & a_{12} & a_{13} \\ a_{21} & a_{22} & a_{23} \\ a_{31} & a_{32} & a_{33} \end{bmatrix}_i \cdot \begin{bmatrix} v_\alpha \\ v_\beta \\ v_0 \end{bmatrix} \tag{9}$$

The relation between reference voltage, duty ratios and non-zero switching vectors is reported in (10).

$$\bar{v} = d_1 \cdot \bar{v_1}^i + d_2 \cdot \bar{v_2}^i + d_3 \cdot \bar{v_3}^i \tag{10}$$

Regarding the duty ratio of the zero switching vectors, it is determined as shown in (11).

$$d_0 = -d_1 - d_2 - d_3 \tag{11}$$

Finally, knowing all duty ratios it is possible to define their distribution inside the modulation period according to the chosen configuration. Table highlights their distribution in the case of a symmetrical configuration, that is the typology chosen for the simulation.

The symmetrical switching pattern associated to each i_{th}-tetrahedron is reported in Tab.12.

4.4 SIMULATION RESULTS

With the aim of highlighting the achievable performance of the proposed ESS-AFS, a simulation in Matlab-Simulink environment has been performed. The sampling time T_s for developing currents and voltages measurements, for performing the overall control algorithm and the 3D-SVPWM is set to 200µs. The DC voltage V_{bus} of the 4L-VSI is set equal to $650V_{DC}$. The proposed ESS-AFS has been tested considering severe load conditions characterised by high currents harmonic content and by a significant relative value of neutral current. For this purpose, it has been considered a three single-phase half-bridge rectifier, supplying DC loads characterised by different demand of DC power. Firstly, the current harmonic compensation process has been evaluated considering equal to zero the average active power delivered by the ESS-AFS.

The simulations have revealed a good behaviour of the proposed control algorithm. In Fig.44 are depicted the PCC phase voltage, the MG phase current before the compensation and the same current after the compensation, all expressed in per unit. It is worth noting the improvements achieved in term of current THD and reduction of neutral current.

Subsequently, the system has been simulated considering two more different working condition of the proposed ESS-AFS. The compensating algorithm starts running at 0.1s. The currents set-points are initially defined

$\frac{d_0}{4}$	$\frac{d_1}{2}$	$\frac{d_2}{2}$	$\frac{d_3}{2}$	$\frac{d_0}{2}$	$\frac{d_3}{2}$	$\frac{d_2}{2}$	$\frac{d_1}{2}$	$\frac{d_0}{4}$

Table 11: Duty cycle configuration for a symmetric 3D-SVPWM.

Table 12: Symmetrical 3D-SVPWM switching pattern.

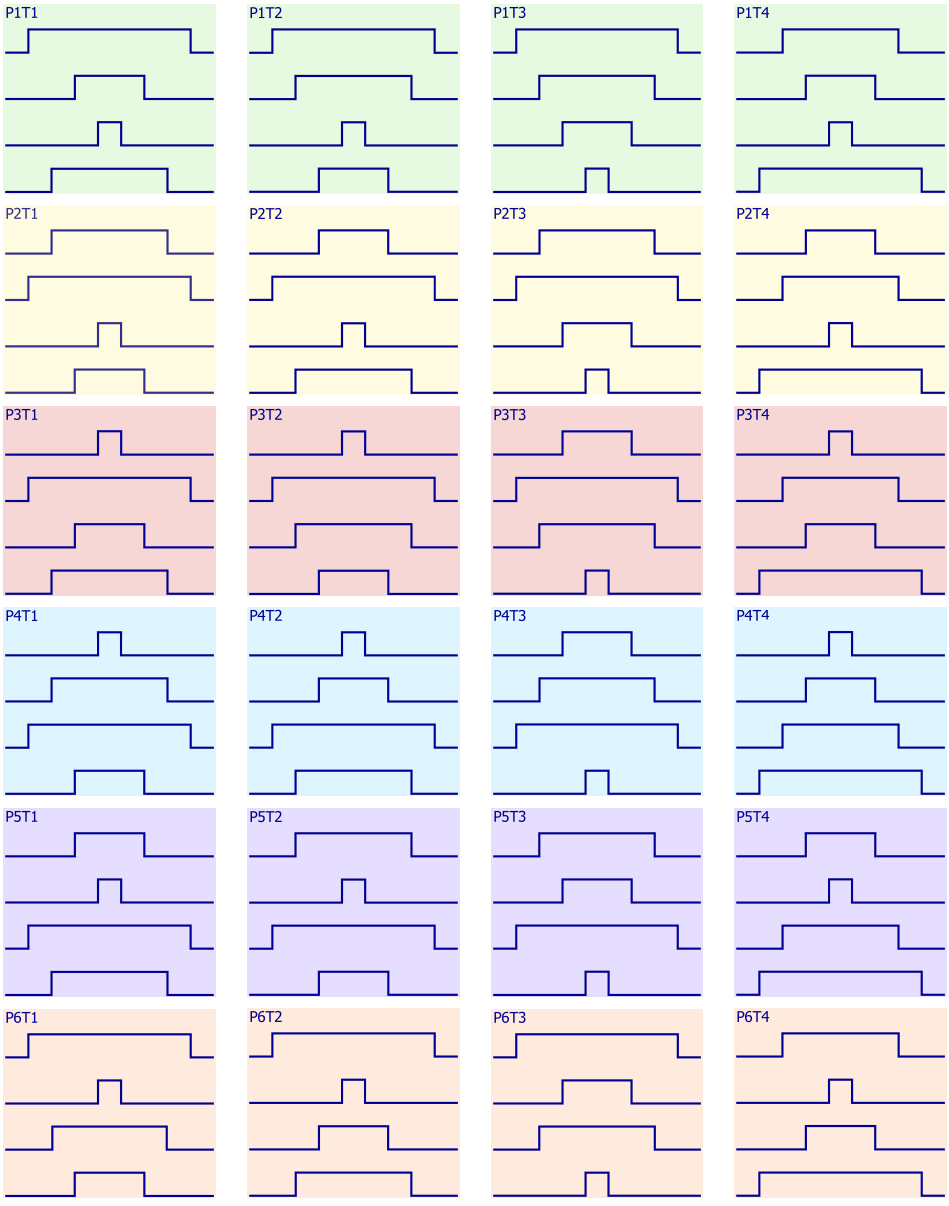

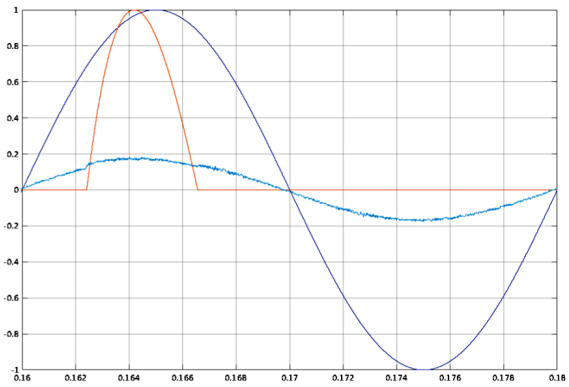

Figure 44: Phase voltage (blue), load phase current (red) and grid phase current (cyan).

for compensating the unbalanced, non-linear loads of the MG. The MG EMS imposes the self-consumption at 0.14s and the delivery of electricity from MG to the power grid at 0.18s.

The time evolutions of the loads currents in the MG, the compensating currents provided by the 4L-VSI and the currents measured at the PCC, during the above reported working profile are shown in Fig.45. Finally, in order to highlight the good performance in term of power quality and power management of the proposed configuration, the corresponding evolution of instantaneous active power, supplied by the power system to the MG during the simulation, is reported in Fig.46.

4.5 CONCLUSION

In this chapter, performances achieved by the integration of active filtering function in a stationary storage system, for energy and power quality management of microgrids, have been analysed. In particular, the proposed solution assumes relevance in the microgrid control due to the problems connected to the interaction among single-phase non-linear Microgrid devices (loads and generators) and three-phase power systems. At this aim, a four-leg voltage source inverter has been considered. A control system, able to integrate the battery energy management and the compensation of current with higher harmonic components, has been proposed and simulated.

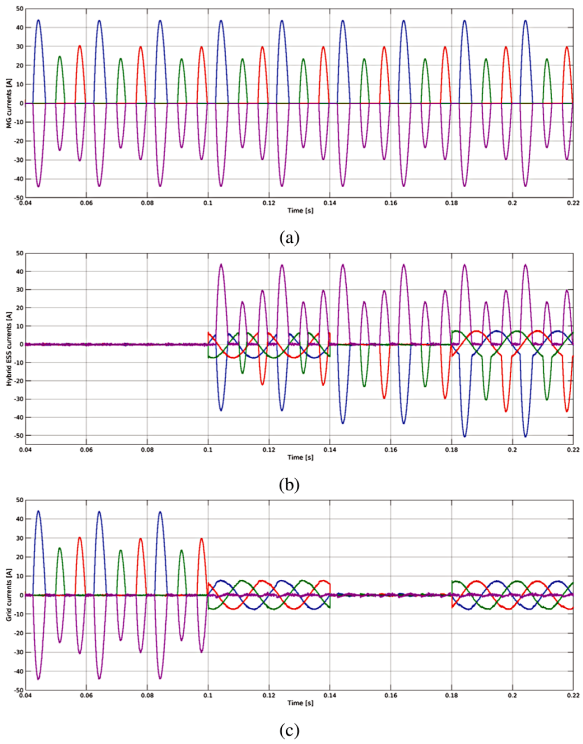

Figure 45: Evolution of load currents of the MG (a), output currents of the proposed hybrid ESS (b) and grid currents (c). Blue curve i_1, green curve i_2, red curve i_3 and magenta curve is the neutral current i_N.

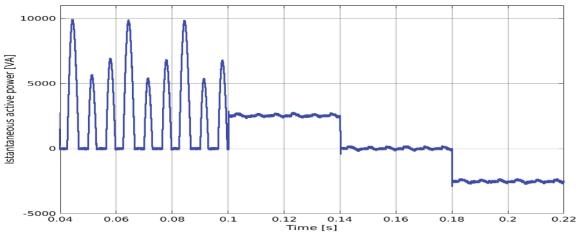

Figure 46: Evolution of instantaneous active power dispatched by the power grid on PCC to the MG before and after the insertion at 0.1 s the AFS.

The results have highlighted the feasibility of the proposal, also in presence of severe load conditions, pointing out the improvement obtainable in term of efficiency and exploitation of RES in microgrids.

5

SODIUM METAL HALIDES BATTERY MODELLING

In this chapter, a model suitable for representing the electrical dynamic behaviour of Sodium Metal Halides Battery (SMHB)s has been reported. In particular, the Thévenin circuit approach has been investigated considering the equivalent circuit parameters as dependent on the State of Charge (SoC). The proposed SMHB model has been developed referring to the experimental tests conducted on a commercial module. In order to identify the Thévenin circuit parameters, a numerical analysis based on measurements of physical quantities of the SMHB under test has been carried out and discussed in detail. An improved iterative fitting procedure, that considers battery physical constraints, has been implemented based on measured data. Subsequently, an optimisation procedure of the fitting results has been implemented. The proposed approaches allow both a significant reduction of steady-state errors with respect to the standard numerical fitting procedure. Finally, the optimization of the first step identification process has been performed obtaining a very small variation in the values of the identified parameters by means of the proposed approach. The comparison between the experimental and simulation results has confirmed the good accuracy of the proposed model in a defined SoC range.

These procedures do not yet reach the desired accuracy for SoC values under 40%. This is due to the non-linearity introduced by the iron reactions occurring in the battery for low SoC values.

Hence, an improved modelling of Sodium Metal Halides Batteries (SMHBs) that considers the effects associated to the iron doping, is presented in the second part of this chapter. The proposed non-linear electrical configuration has been developed analysing both the electrochemical phenomena, occurring during the discharging and charging processes, and the experimental tests performed on a SMHB. The parameters of the proposed electrical model have been determined by referring to step-current tests, specifically designed for their identification and performed on a commercial SMHB. In order to point out the improvements achieved, the comparison between the experimental and the simulation results is presented. In particular, the voltage time-evolutions during step currents application are shown. These are evaluated considering both the proposed SMHB Thévenin model and that

recently reported in the technical literature. Results obtained improves the possibility to mimic the behaviour of SMHB especially at low values of SoC, opening new opportunity in the exploitation of this class of electrochemical batteries.

5.1 INTRODUCTION ON SMHB

In chapter 1 the high temperature SMHB has been mentioned as one of the most promising solutions for E-ESS. SMHBs are indeed characterised by large availability of their materials (sodium chloride and nickel) and a high discharge rate, fast response to power demand, immunity to ambient temperature, unitary coulomb efficiency and intrinsic safety, are thus considered one of the most interesting E-ESSs to provide ancillary services in transmission and distribution systems [80], [81],[82] , [83], [84].

One of the most attractive properties of SMHB technology is the capability of providing high peak power pulses at any SoC (for a limited discharge duration) [82], [84]. This uncommon result is achieved by adding iron to the cathodic active material and consequently forming a second sodium/iron cell that takes part in the discharge reactions. Nevertheless, this increases the complexity of battery behaviours determining difficulties in modelling properly the battery when low SoC values occur. In order to overcome these difficulties, the BMS is set to limit the SoC in a range between 80% and 20% reducing consequently its potential exploitation. Moreover, the particular complexity and the non-linearity of the electrochemical reactions occurring at low SoC do not allow the implementation of SoC observer, forcing towards the usage of coulomb counting method that requires periodically a complete recharge of the SMHB to reset the integrator offset.

In this background, the development of accurate models of SMHB, able to reproduce correctly the battery behaviour at low SoC, represents an important target to extend the battery capacity range and to develop novel BMS, based on SoC observers. This typology of BMS could extend the battery life or/and avoid the necessity of resetting the SoC. Hence, the development and implementation of models able to simulate accurately SMHBs behaviour is an important topic to spread this technology at both a technical and an economic point of view. So far, a variety of battery models have been proposed with different degrees of complexity and accuracy, being basically grouped into three classes: electrochemical, mathematical

and electrical [85]. The first provides high accurate modelling of the electrochemical reactions inside the battery. For this reason, its use is mandatory in the analysis of physical energy conversion processes oriented to batteries design and optimisation. However, this type of modelling requires a high computational effort to solve complex partial differential equations, which make its implementation unsuitable for real-time applications. The second, the mathematical modelling approach, uses the experimental current-voltage characteristics related to the steady-state condition, with the aim of deriving a model based on runtime instructions by applying statistical modelling [86]. Nevertheless, these models do not take into consideration the battery dynamics. Finally, electrical models describe batteries as electric circuits with parameters representing some physical internal phenomena. This approach is widely implemented because requires low computational time and memory, it is simple to be realised and provides accurate dynamic behaviour of the battery. Electrical models are additionally divided into two major categories: impedance-based and Thévenin-based models. The former are determined considering a frequency domain analysis of the current-voltage behaviour of the battery. Their parameters are extracted based on electrochemical impedance spectroscopy. Whereas, the latter are constituted of elements as resistors, capacitors, voltages sources, connected in such way as to represent the correct behaviour of the battery compared to experimental current and voltage characteristics. Such circuit-based models are therefore the most suitable for runtime estimations and for BMS implementation, offering different degrees of accuracy depending on the complexity of the implemented circuit.

Concerning the SMHB technology, the models presented in the literature are based on Thévenin circuit approach [87], [88], [89], [90]. An electrical circuit model of the sodium-nickel chloride battery is proposed in [88], which consists of an ideal voltage source and a dynamic equivalent internal resistance, that is a function of the SoC and the temperature. Such an approach is appropriate for the long-term management of this kind of storage but presents inaccuracies in modelling the slow and fast dynamics of the battery. A similar model of SMHB related to the steady-state condition is reported in [89]. In particular, in this case, the equivalent electric circuit is characterised by an Open Circuit Voltage (OCV) and a resistance, which are expressed as a function of Depth Of Discharge (DoD) or SoC for discharging and charging stage respectively. The model is developed in the Simulink environment and parameters values are determined using a look-up table built based on experimental measurement. Moreover,

in the development of the model has been taken into account also the dependence of the battery internal resistance by current rate during discharge. This model is particularly suitable for steady-state analysis, indeed it shows voltage estimation errors during step current transients. A non-linear dynamic second-order model of SMHB based on the Thévenin circuit modelling approach is reported in [90]. In particular, a two RC-branches electrical model of a nickel-sodium chloride battery has been proposed. The parameter identification has been performed using sequences that alternate current steps and relaxation periods, for different SoC values. The investigation has revealed some critical in the identification of the equivalent circuit parameters. Moreover, the optimisation process for the parameter identification has been developed to minimize the error without taking into account the physic constraints associated with the electrochemical process.

In the first part of this chapter, a first model of battery is presented whose parameters are determined through a fitting procedure that takes into account the physical constraints of the battery itself. This is compared to a second model obtained through a standard fitting procedure and an optimisation procedure. The above-mentioned procedures show inaccuracy for the SoC values lower than 40%, because of the presence of non-linearity introduced by iron reactions. For this reason, an improved SMHB battery model, that considers also the presence of iron reactions, has been implemented and is presented in the second part of this chapter.

5.2 THE SODIUM METAL HALIDES BATTERY

The Sodium Metal Halides Cell (SMHC) is a secondary type of electrochemical battery able to develop the charging and discharging processes using as charge carriers the sodium-ions Na^+, providing a complete reversible electrochemical reaction, reported in (12), at an OCV of 2.58 V.

$$NiCl_2 + 2Na \leftrightarrows 2NaCl + Ni \qquad @OCV = 2.58V; \tag{12}$$

The symbols ($\rightarrow$) ($\leftarrow$) reported in (12) point out the discharge and charge reactions respectively. The SMHC requires a specific design to accomplish these reactions as reported in the following.

In particular, the SMHC has a solid positive electrode, made of nickel chloride in a matrix of nickel. In the middle of the positive electrode, a nickel strip is immersed in a secondary liquid electrolyte of sodium chloral-aluminate ($NaAlCl_4$) that serves as a current collector. The neg-

ative electrode is composed of liquid sodium, separated from the positive one by a primary solid ceramic electrolyte made of β-alumina. The solid ceramic electrolyte, permitting just the migration of sodium-ions between electrodes, allows that the reactions reported in (12) take place and guarantees, at the same time, the electrical insulation between anode and cathode. With the aim of having sodium in a liquid phase the cell temperature, after the process of sodium liquefaction, has to be kept in a range between 260-350°C.

One of the main feature to focus on in the battery design is the power density. In the SMHC, different solutions oriented to increase power density have been proposed. Two of them are currently used in commercial batteries. The first one is the enhancement of the active surface per cell volume of the solid electrolyte, resorting to a quadrilobate section. The second one is the iron doping of the positive electrode. The iron in the cathode, indeed, reacts in the same manner of nickel, as shown in (2), but at an OVC equal to 2.35V.

$$FeCl_2 + 2Na \leftrightarrows 2NaCl + Fe \qquad @OCV = 2.35V \tag{13}$$

This means that the iron reaction occurs when the voltage reaches values lower than that of the nickel one. The different design geometry of solid ceramic electrolyte and the iron doping, have the main effects of increasing the cell pulsing current and the reducing the inner cell resistance, determining consequently an increase in power peak. This result is achieved because, during the discharging process, the battery current flow generated by the nickel reaction can determine a cell voltage drops, that leads the output voltage below the characteristic OCV value related to the iron reaction. This activates the iron in the cathode so that both the reactions reported in (12) and (13) take place at the same time, contributing to the output current. When the current demand decreases, the output voltage rises up and the iron-sodium reaction inverts its evolution. For this reason, a recovery of the $FeCl_2$ occurs near the surface of the β-alumina, until iron is completely consumed. The electrochemical reactions reported in (13), involving Fe and $FeCl_2$, are faster than the nickel ones modifying consequently the dynamic evolution of the output voltage.

As a consequence of the above depicted single cell reactions, the modelling of SMHB is particularly complex and assumes a non-linear behaviour depending on the SoC, on the temperature and on the current rate. In particular, the current rate can activate the iron electrochemical reactions,

	Unit	Value
Rated discharge power	kW	7.8
Rated voltage	V	620
Electrical stored capacity	kWh	23.5
Volumetric energy density	kWh/m^3	280
Gravimetric energy density	Wh/kg	140
Nominal temperature	$°C$	270
Calendar life @ 80% DoD	$years$	15
Cycle-life @ 80% DoD	$cycles$	4500

Table 13: SMHB module characteristics of FIAMM SoNick ST523

which are difficult to reproduce considering just the nickel-based model reported in the technical literature. Therefore, the definition of a simplified model that represents correctly the dynamic evolution of the phenomena occurring in the battery, is fundamental for the management of SMHB.

5.2.1 *SMHB module under test*

The model and the experimental results of SMHB reported in this paper refer to the FIAMM SoNick ST523. This battery is characterised by the connection in series of 240 cells enclosed in a metallic container. The modules include an electric heater for the battery temperature management which is controlled by the BMS. Moreover, the BMS provides other functions, as charge regulation, monitoring and diagnostics, which are developed through the measurements and elaboration of battery current, voltage and temperature. The main operating data of the SMHB module under test are reported in Tab.13.

5.3 THE FIRST MODEL PROPOSED

The electrical models are based on a Thévenin equivalent circuit, whose general structure is reported in Fig.47. The equivalent circuit of the battery presents a controlled voltage source V_{OC}, an internal resistance R_0 and a variable number RC branches connected in series. The more RC circuits connected in series there are, the higher the model accuracy is; however, the simulation time also increases. Two parallel RC circuits in series are

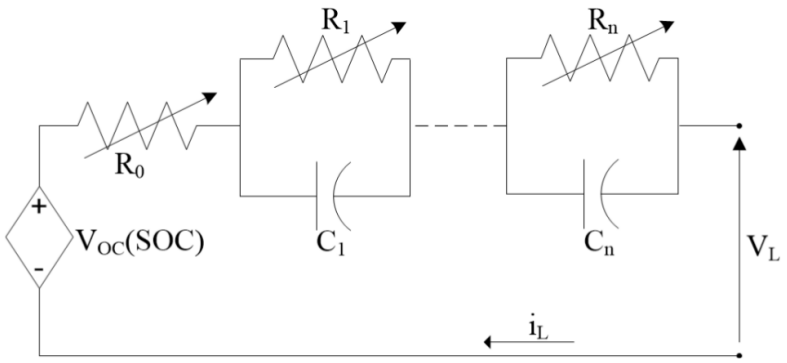

Figure 47: The Thévenin equivalent circuit used for the first modelling approach.

usually considered the most appropriate compromise in battery modelling [91].

The parameters of the battery equivalent circuit generally are characterised by a non-linear dependence by the SoC, temperature and the current rate. These dependencies are strictly related to the electrochemical characteristic of the cell used in the battery [85], [92], [24].

During the development of the equivalent circuit some assumptions, based on the analysis of technical literature, has been done and reported in the following [15], [16]:

- The OCV (V_{OC}) has been expressed just as a function of SoC during charging and discharging stages;
- The temperature dependence on OCV has been considered negligible due to the temperature control of the module, which guarantees an operating range within 260°C and 300°C;
- Resistances and capacitors, reported in the SMHB equivalent circuit, depend just on the SoC;
- The internal resistance dependence on the current rate has not taken into account directly.

Moreover, the electrical circuit configuration has been developed referring to the electrochemical and physical phenomena occurring in the battery. In particular, V_{OC} is the equilibrium potential of the battery; R_0 is the ohmic internal resistance of solid ceramic electrolyte and interconnecting

metal; the two RC branches reproduce the transient response of the battery. In particular, R_1 and C_1 are associated to the fast battery dynamics related to reaction kinetics and surface effects on the electrodes arisen from the double-layer formation, whereas R_2 and C_2 represent the slower dynamics typical of diffusion processes in the electrolyte and active materials. All the above-described phenomena have a different evolution depending on the SoC of the battery. Consequently, all the equivalent circuit parameters are subject to a variation during the charging and discharging processes that are generally summarised expressing them as a function of the SoC. Hence, for the correct implementation of the battery modelling, a SoC estimator is required. It can be simply implemented by applying the coulomb-counting method as in the following reported:

$$SoC(t) = SoC(0) + \frac{1}{C_B}\int_0^t i_L(t)dt \tag{14}$$

where C_B represents the nominal battery capacity and i_L is the battery current.

Based on the above assumptions and considering the non-linear characteristic of the proposed battery model, the following equation can be used to model the battery terminal voltage $v_L(t)$:

$$v_L(t) = v_{OC}(t) - v_0(t) - v_1(t) - v_2(t) \tag{15}$$

where v_{OC} and $v_i, i \in \{0, 1, 2\}$ are the instantaneous evolutions of OCV, of voltage drops on R_0, R_1C_1, R_2C_2 branches respectively. In the time domain, this model takes also into account the circuit parameters dependence on the SoC. However, the parameters which are dependent on SoC, have a dynamic evolution that, in first approximation, can be considered slower than that of the battery terminal voltage. Hence, when fast transient phenomena occur, in the proposed model, parameters of the equivalent circuit can be considered constant or quasi-constant. Therefore, the Laplace transform can be used to determine the analytic solution of the battery terminal voltage evolution, when step currents are applied. Under this hypothesis, the Laplace transformation of (15) is reported in (16).

$$V_L(s) = V_{OC}(s) - V_0(s) - V_1(s) - V_2(s) \tag{16}$$

Considering the application at the time instant t_r of a step current from I_L to zero, the application of Laplace transform allows the evaluation of

each element of (16) as reported in (6) where $\tau_i = R_i C_i, i \in \{1,2\}$ are the time constants of the corresponding RC-branch.

$$\begin{aligned} V_0(s) &= R_0 I_L \left(\frac{1 - e^{-t_r rs}}{s} \right) \\ V_1(s) &= \left(\frac{\tau_1}{1+\tau_1 s} \right) v_1(t_r) + R_1 I_L \left[\frac{1 - e^{-t_r s}}{s(1+\tau_1 s)} \right] \\ V_2(s) &= \left(\frac{\tau_2}{1+\tau_2 s} \right) v_2(t_r) + R_2 I_L \left[\frac{1 - e^{-t_r s}}{s(1+\tau_2 s)} \right] \end{aligned} \tag{17}$$

When a step current from I_L to zero on the equivalent battery circuit has been applied, the inverse Laplace transform of (16) allows determining the analytic solution of transient evolution of the terminal voltage. This assumes the form reported in (18) where the parameters K_a, K_b, K_2, K_3 are related to the parameters of the equivalent circuit and to the initial current and voltage condition as reported in (19), where $\delta - 1$ represents the unit step function (Heaviside function). Similarly, when a step current from zero to IL occurs, the transient terminal voltage can be determined.

$$v_L(t) = \underbrace{K_a + K_b}_{K_1} + K_2 e^{-\frac{t}{\tau_1}} + K_3 e^{-\frac{t}{\tau_2}} \tag{18}$$

$$\begin{aligned} K_a &= -R_0 I_L [1 - \delta_{-1}(t - t_r)] \\ K_b &= v_{OC}(t_r) - (R_1 + R_2) I_L [1 - \delta_{-1}(t - t_r)] \\ K_2 &= R_1 I_L \left[1 - \delta_{-1}(t - t_r) e^{-\frac{t_r}{\tau_1}} \right] - v_1(t_r) \\ K_3 &= R_2 I_L \left[1 - \delta_{-1}(t - t_r) e^{-\frac{t_r}{\tau_2}} \right] - v_2(t_r) \end{aligned} \tag{19}$$

5.4 PARAMETER IDENTIFICATION METHOD

The method generally used for identifying the equivalent circuit parameters in the Thévenin circuit modelling is based on the numerical analysis of the battery physical quantities measured. In particular, the battery terminal voltage is acquired and saved, during discharging and charging pulse tests,

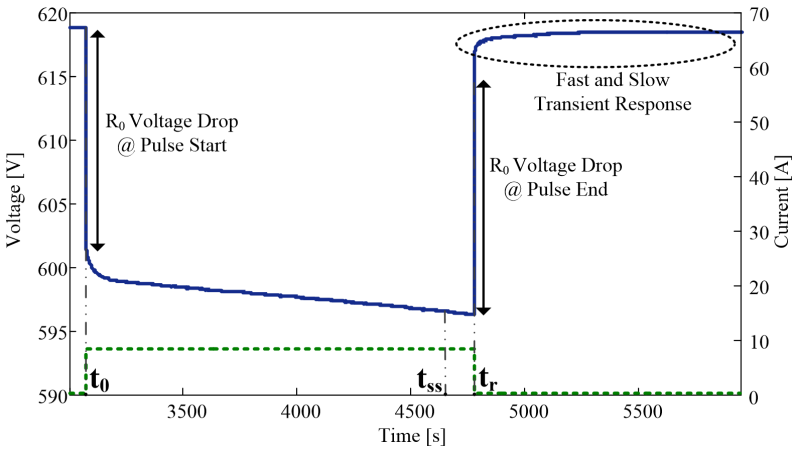

Figure 48: Qualitative battery voltage response (blue) to a step current event (dashed green).

in order to be later examined. The above-mentioned pulse tests consist of a sequence of constant current pulses aimed to obtain, for set SoC values, the corresponding terminal voltage time evolutions. Between each pulse, a defined rest-time interval is set, allowing the battery voltage evolution to reach the DC steady state. The battery voltage response to a generic current pulse assumes the qualitative time evolution reported in Fig.48.

As a first step, the internal resistance Ro is calculated by (20), after the preliminary identification of the associated voltage variation (ΔV) when the current step is beginning or ending (ΔI):

$$R_0 = \left| \frac{\Delta V}{\Delta I} \right| \tag{20}$$

This methodology requires a perfect synchronisation between the measurement and the step current application in order to be able to correctly evaluate the step voltage variation. Moreover, it is necessary to decouple the fast dynamic of the battery voltage from the slow one. It is worth noting that it is difficult to satisfy this condition and for this reason, the identification of R_0 suffers from evaluation errors. Referring to the Fig.48, the next step of the identification process is the evaluation of OCV, at the value of SoC corresponding to the instant t_r. It can be determined by considering the value of the terminal voltage reached after the relaxation phase. Finally, the time constants of RC-branches, as well as the capacitor voltages, can be determined by means of a numerical fitting procedure applied to the equation in (18), considering only the portion of the curve after the instant t_r.

Unfortunately, the error estimation in R_0 introduces an error in the definition of the initial voltage v_1 and v_2 at the instant t_r. This determines consequently an error in the identification of time constants τ_1 and τ_2. Therefore, in order to optimise the parameter identification and minimise the modelling error, a numerical optimisation toolbox is generally used. To improve the accuracy of the parameter identification process during the fitting procedure, an integration of the above-described procedure has been proposed. The model reported in (18) and (19) has been used to determine the parameter of the equivalent circuit, but taking into account also the constraints associated with the value of the internal resistance. Assuming that the internal resistance is equal to the sum of the three resistance reported in the Thévenin circuit, it can be experimentally determined by considering the OCV measurement after the relaxation time $t_r + t_{rx}$. Considering that the steady-state condition is reached at the instant t_r, the relation (10) allows the estimation of the global internal resistance of Thévenin equivalent circuit at the same instant:

$$(R_0 + R_1 + R_2)_{t_r} = \frac{v_L(t_r) - v_{OC}(t_r + t_{rx})}{I_L(t_r^-)} \tag{21}$$

An iterative procedure, subdivided into the R_0 evaluation and the fitting procedure application, was carried out in order to minimize both the internal resistance estimation error and the fitting procedure one.

5.5 SMHB TEST BENCH

The characterization of the SMHB module has been performed by using the experimental set-up depicted in Fig.49. Discharging processes are managed by a programmable DC electronic load (EL-9750- 75 HP by Elektro-Automatik), which features a maximum current, voltage and power of 75A, 750V, and 7.2kW, respectively. A DC power supply EA PSI-81500-30-3U is used during charging. It can operate in controlled voltage mode or current source mode with an output voltage and a current range equal to $0 - 1500V$ and $0 - 30A$, respectively. Furthermore, its maximum output power is 15kW. A National Instruments cDAQ-9172 equipped with an NI-9205 module is used to acquire battery current and voltage. All equipment is controlled and managed by means of Virtual Instruments (VIs) specifically developed in the NI-LabVIEW environment. All measurements can be monitored online from the host computer through the VIs Graphical

Figure 49: The battery test-bench: 1) SMHB module, 2) DC Power Supply, 3) DC Electronic load, 4) Data acquisition system, 5) Host PC.

User Interface (GUI). The program is able to set the acquisition sampling time and to receive specific measurements from the electronic load and power supply, such as the Ah counter and elapsed time data. Discharging and charging processes are managed by properly coordinating the VIs and the BMS software. This allows to check the status of the battery pack, control the warm-up and SoC-reset charge as well as empower charging/discharging tests depending on battery temperature, SoC and voltage levels. The measurements from VIs and BMS are combined and merged in order to get a uniform data structure and consequently extract all the relevant information for the battery modelling and characterisation.

5.6 RESULTS

By the two fitting procedures described in section 5.4, the identification of circuit parameters has been implemented. In particular, the results related to the proposed one are reported in Tab.14, in which the look-up table representing the evolution of parameters in relation to SoC variation, has been presented. The corresponding two simulations of the SMHB model, under the same step current pulse application, have been developed.

The comparison among the experimental result and the simulation ones are reported in Fig.50. It is worth noting that the proposed iterative fitting method achieves better results for all SoC range. In particular, the use of an iterative method, based on a constraint on the internal resistance, al-

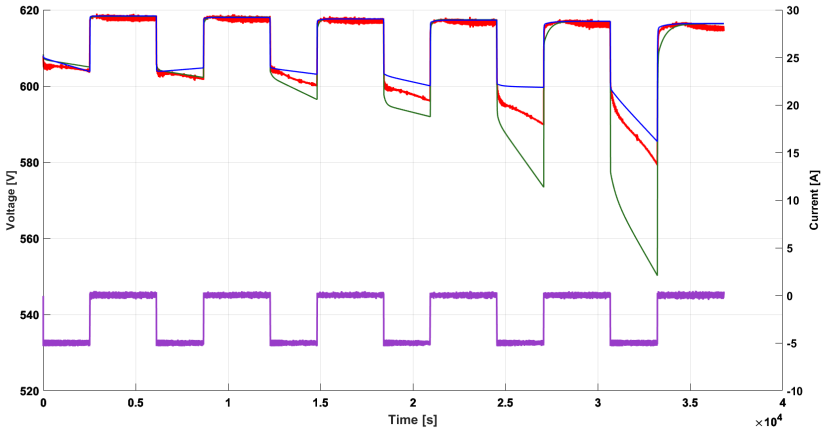

Figure 50: Comparison among the SMHB module voltage evolution (red), measured during discharging phase characterised by step current pulses of 5A (purple), and the simulation results of the Thévenin circuits based on the look-up tables evaluated by using the fitting procedure reported in the literature (green) and the proposed one (blue).

SoC	$V_{OC}[V]$	$R_0[\Omega]$	$R_1[\Omega]$	$R_2[\Omega]$	$C_1[F]$	$C_2[F]$
90%	618.5	2.1269	0.0796	0.0502	62.8378	1818.1
80%	618.4	2.8693	0.1467	0.0542	23.8582	1844.3
70%	618.0	2.4778	0.2075	0.0679	21.6867	2161.7
60%	617.6	2.6730	0.2638	0.0999	17.0584	2001.2
50%	617.3	3.1706	0.3181	0.1273	28.2930	2055.0
40%	617.0	2.9809	0.4656	0.1804	32.2165	2431.8
30%	616.4	4.2541	2.0440	0.2705	7.7348	1629.9

Table 14: Parameters identified by the proposed fitting procedure.

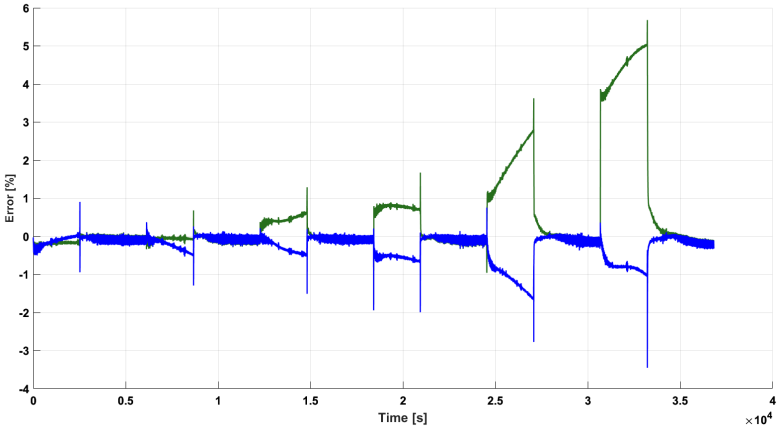

Figure 51: Evolution of the error related to the comparison between the measured voltage and the one evaluated by the fitting procedure reported in the literature (green trace), and the error related to the comparison between the measured voltage and the one evaluated with the proposed procedure (blue trace). In both cases the dischargine phase is characterised by step current pulses of 5A.

lows the reduction of voltage errors during both steady state and transient stages, which assume significant values for low SoC. This is pointed out in Fig.51 where the comparison between the battery terminal voltage errors, evaluated respect to the experimental results, is presented.

Based on these results and with the aim of verifying the goodness of the identification performed by means of the proposed fitting procedure, an optimisation toolbox for the Thévenin circuits parameters identification has been implemented. The results of the parameters identification performed by the Matlab-Simulink optimisation toolbox are reported in Tab.15.

The comparison between of the data reported in Tab.14 and Tab.15 confirms that the proposed fitting procedure allows the identification of a set of parameters that are very close to the optimal one. Fig.52 depicts the comparison between the measured voltage evolution and the one determined by a simulation run with the set of optimal parameters. The evaluation of the estimation error evolution is reported in Fig.53.

A Thévenin circuit approach, considering a two RC-branches electrical model, suitable for modelling the dynamic behaviour of a Sodium Metal Halides Battery (SMHB) has been investigated. The proposed SMHB model

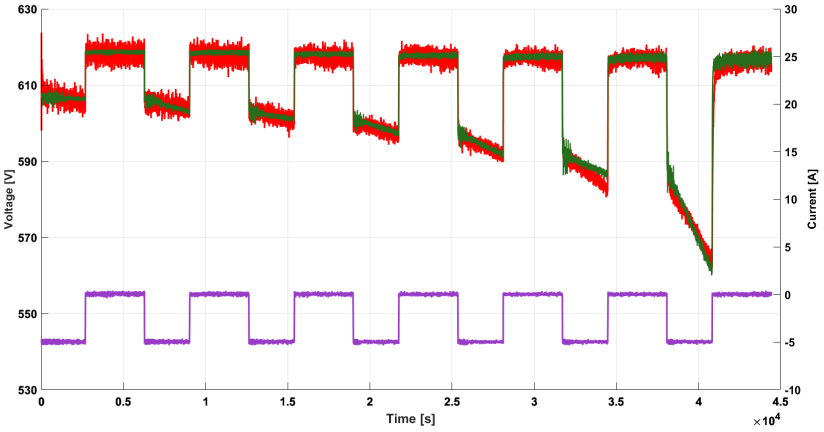

Figure 52: Comparison between measured voltage evolution, on SMHB module (red trace), and simulation results of the Thévenin circuit based on the look-up table evaluated by means of the optimisation procedure (green trace), when a discharging phase characterised by step current pulses of 5A (purple trace).

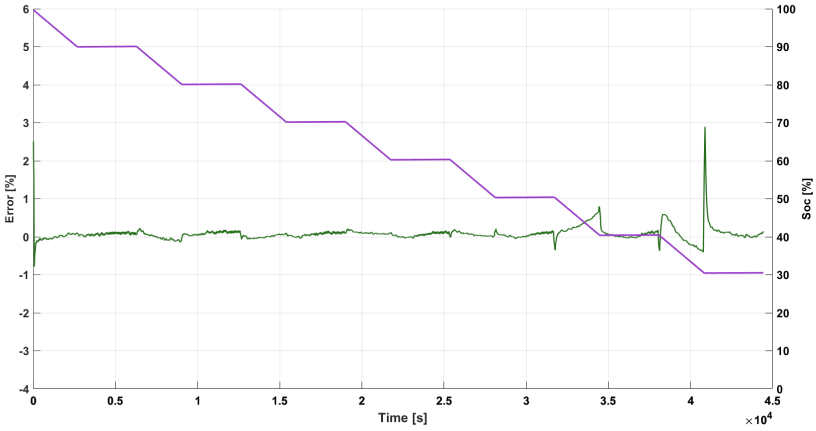

Figure 53: Percentage error (green trace) between experimental and the simulation results, obtained applying the look-up table determined by the optimisation procedure, and the corresponding SOC evolution (purple trace), during a discharging phase characterised by step current pulses of 5A.

SoC	$V_{OC}[V]$	$R_0[\Omega]$	$R_1[\Omega]$	$R_2[\Omega]$	$C_1[F]$	$C_2[F]$
90%	618.5	2.3263	0.0798	0.0502	62.8220	1817.9
80%	618.4	2.9228	0.1469	0.0542	23.8590	1844.2
70%	618.0	3.1394	0.2101	0.0685	21.6850	2159.6
60%	617.6	3.7187	0.2802	0.1008	17.0580	1999.8
50%	617.3	4.7105	0.3424	0.1328	28.2920	2041.5
40%	617.0	5.4863	0.5050	0.1874	32.1680	2392.1
30%	616.4	8.0521	3.0803	0.2844	7.7910	1630.4

Table 15: Parameters identified by the proposed optimisation procedure.

has been developed referring to a commercial module with a capacity of 23.5kWh and a rated discharge power of 7.8kW. The aim of the proposed activity is providing a model that can be used to validate the use of the SMHB technology for smart grid applications and evaluate its performance for stationary systems. The model parameters identification method, as well as the measurement tests carried out for their evaluation, are reported and described. The numerical processing of the specific measurements of an SMHB test-bench, considering the dynamic analytic solution of Thévenin circuit battery voltage, has been proposed taking into account an additional physical constraint related to the internal battery resistance.

The comparison among the experimental results and the fitting procedure proposed and that presented in the technical literature has been reported, confirming the goodness of the proposed approach. The results demonstrate good performances in the 90%-40% SOC range, but also show inaccuracies at lower SoC due to the mixed iron/nickel cathode. These aspects will be investigated in the next sections.

5.7 THE IMPROVED MODEL

As explained in the previous section, the model based on Thévenin equivalent circuit characterised by two RC-branches suffers from low precision at low SoC values, due to the effects of iron reaction. Therefore, this model does not match the experimental measurements despite the implementation of optimization algorithm during the parameters identifications of the Thévenin equivalent circuit [93].

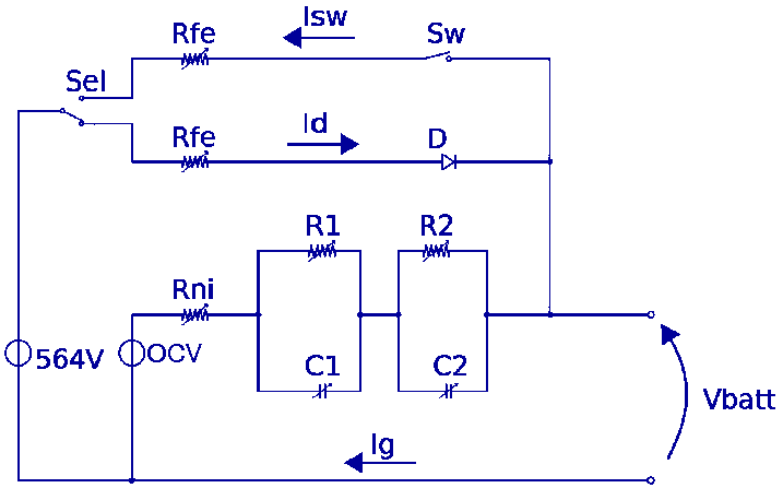

Figure 54: Proposed improved electrical model of SMHB.

In order to reproduce the iron effects in SMHB, the classical two series RC parallel Thévenin equivalent circuit has been modified introducing another parallel branch. In particular, referring to the commercial module described in section 5.5, the configuration of the proposed equivalent circuit is shown in Fig.54.

The nickel reaction is modelled in the equivalent circuit through a branch composed by a voltage generator, a resistance R_{ni} and two RC parallel branches in series : the first resistance represents the resistive contribute of nickel and the RC branches introduce two time-constants that represent the voltage transient due to current variation during the charge and discharge phases. The iron branch is composed by a voltage generator and a resistance R_{fe}: the voltage generator has been set with a constant value of 564V, that represents the minimum threshold below which the iron reaction takes place, and a resistance R_{fe} that represents the iron resistive contribute.

The iron branch has been duplicated and two controlled switches have been introduced, as shown in Fig.54, to represent the reversible behaviour of iron reaction. In particular, by means of two switches, the current flux into the iron branches is managed as explained in the following. The Sel switch is placed between the constant voltage generator and the iron branch and its task is to let the current flow in one of the two iron branches. When the output voltage V_{batt} is lower than the iron threshold level (564V), the current flows towards the battery terminals and an integrator counts the amount of charge that flows in that direction; while if the output voltage is higher than 564V, the current flows in reverse direction and an-

other coulomb counter measures the charge flowing. The switch Sw is controlled by a digital signal obtained considering the difference between two coulomb counters. In particular, when the charge related to the iron reaction and associated with the discharge stage is equal to that of the charging one, and thus the difference is zero, the switch is open. This considers that the current flux in reverse direction can not be greater than the flux in the forward direction.

All parameters in the equivalent circuit proposed are related to the battery SoC. In the model shown in Fig.54, the output voltage V_{batt} is expressed as reported in (22) and (23), obtaining the equation in (24).

$$V_{batt}(t) = OCV(t) - V_{ni}(t) - V_1(t) - V_2(t) \tag{22}$$

$$V_{batt}(t) = 564 - V_{fe}(t) \tag{23}$$

$$2V_{batt}(t) = OCV(t) + 564 - V_{ni}(t) - V_{fe}(t) - V_1(t) - V_2(t) \tag{24}$$

The use of Laplace transform, with the application of a step-current, allows analytic estimation of the output voltage time-evolution reported in (25) where the parameters k_1, k_2 and k_3 are the model variables and τ_1, τ_2 are the time-constants related to both RC branches.

$$V_{batt}(t) = k_1 + k_2 e^{\frac{-t}{\tau_1}} + k_3 e^{\frac{-t}{\tau_2}} \tag{25}$$

In order to identify the parameters evolution with the SoC specific tests, with 10% charge and discharge rate of SoC, has been performed using the hardware described in section 5.5 and depicted in Fig.49.

During tests, each 10% charging and discharging phase is characterized by the following step current: a first interval with a constant current of $5A$ reduce the SoC of 9%; a second interval with a constant current of $10A$ reduce the SoC of 1%. An analogous subdivision was made during the charging phase. After each step, the current is imposed equal to zero during all the relaxation time, the duration of which has been chosen to reach the steady-state of the battery. In particular, for lower SoC values during the discharge phase, the relaxation time has to be longer because the dynamic evolution is slower. Similarly, the same happens for higher SoC values during the charge phase.

The output current of the battery during each 10% variation of SoC is shown in Fig.55. The parameters estimation at different values of SoC has

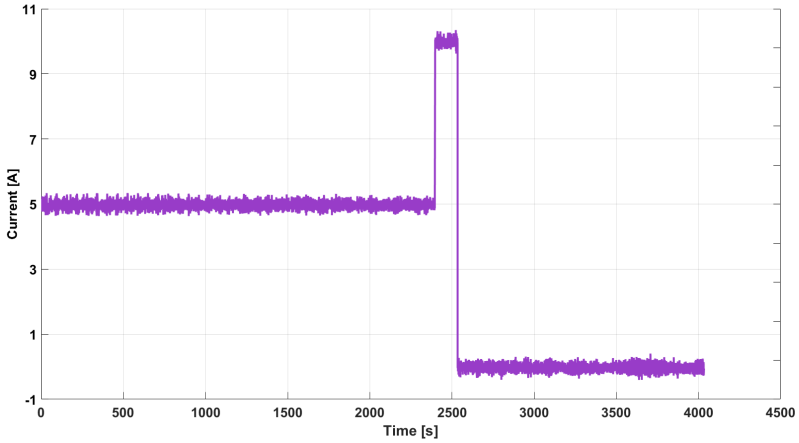

Figure 55: The step current evolution during each SoC step of 10%.

been obtained applying the fitting operation on the equation (25), using the Matlab tool and imposing the experimental voltage. In particular, the presence of two voltage drops, corresponding to the step-current from 5A to 10A and from 10A to 0A, allows detecting with more precision the Rni. The time-constants related to both RC branches are detected considering only the curve section corresponding to the relaxing time (step-current set to 0A) in the curve fitting procedure.

The method adopted to calculate the R_{fe} is described in the following. During the step from 5A to 10A, the voltage drop does not decrease under the limit threshold of 564V, so it is possible to evaluate R_{ni} as the ratio between voltage and current because it can be assumed that the current is just function of the R_{ni}. It is worth noting that during this step the current flows only through the nickel branch. Whereas, during the step 10A to 0A the voltage drop decrease under the threshold, so it is possible to determine R_{fe} as the ratio between voltage and current, based on superposition principle and assuming R_{ni} as constant throughout the entire step. The battery voltage evolution during discharge and charge tests is reported respectively in Fig.56 and Fig.57.

The same procedure used to determine the parameters during discharge phase has been used also throughout the charge one. Discharge and charge parameters results are shown in Tab.16 and Tab.17 respectively.

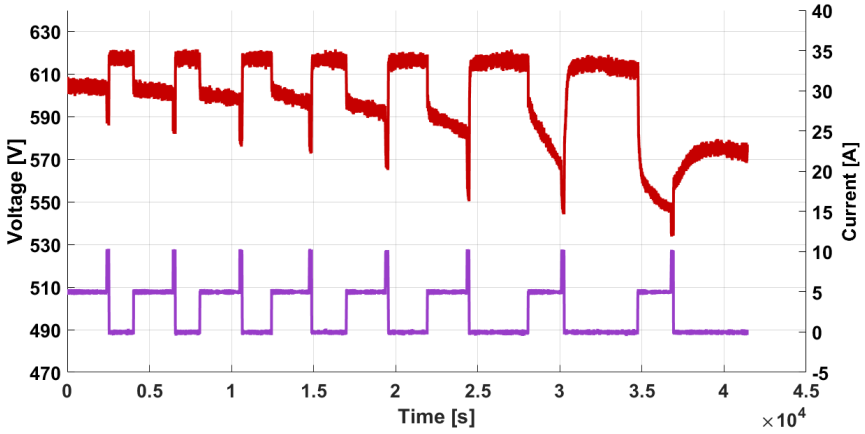

Figure 56: Time evolutions of the voltage (red trace) and current (purple trace) on SMHB during the discharge test.

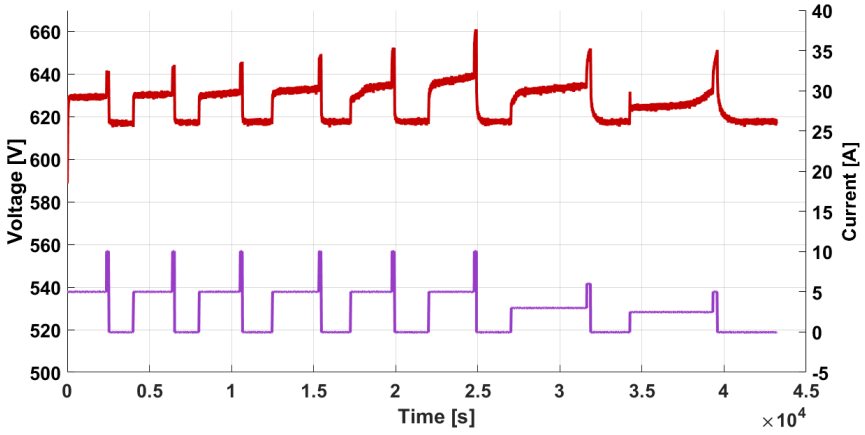

Figure 57: Time evolutions of the voltage (red trace) and current (purple trace) on SMHB during the charge test.

SoC	OCV[V]	$R_{ni}[\Omega]$	$R_{fe}[\Omega]$	$R_1[\Omega]$	$R_2[\Omega]$	C_1[F]	C_2[F]
90%	617.9	2.4	-	0.0611	0.1233	1181.7	25.25
80%	617.7	2.55	-	0.0804	0.2759	952.74	6.071
70%	617.5	2.62	-	0.0979	0.5357	1570.5	3.6065
60%	617.3	2.65	-	0.1351	1.107	1221.3	1.7886
50%	616.8	2.66	-	0.1827	1.463	846.74	1.6261
40%	616.6	2.39	-	0.2216	2.521	1430.5	2.3937
30%	616.4	2.48	4	0.2743	4.024	2155.3	5.7033
20%	614.4	2.82	4	0.5068	4.73	2.48	28.54
10%	576.7	2.7	4	0.2795	2.02	4.9517	438.86

Table 16: Circuital parameters of the discharge phase.

SoC	OCV[V]	$R_{ni}[\Omega]$	$R_{fe}[\Omega]$	$R_1[\Omega]$	$R_2[\Omega]$	C_1[F]	C_2[F]
20%	616.8	2.12	-	0.2698	0.1392	23.94	1301.7
30%	617.3	2.14	-	0.3938	0.1371	17.58	946.75
40%	617.7	2.13	-	0.4431	0.1702	16.92	420.21
50%	617.8	2.25	-	0.5033	0.334	14.01	177.99
60%	617.8	2.29	-	0.6709	0.4489	14.62	183.47
70%	617.8	2.49	-	0.9602	0.852	16.34	144.01
80%	617.6	2.91	-	1.2282	1.7817	19.92	112.14
90%	617.6	3.15	-	1.6366	2.126	29.02	163.64

Table 17: Circuital parameters of the charge phase.

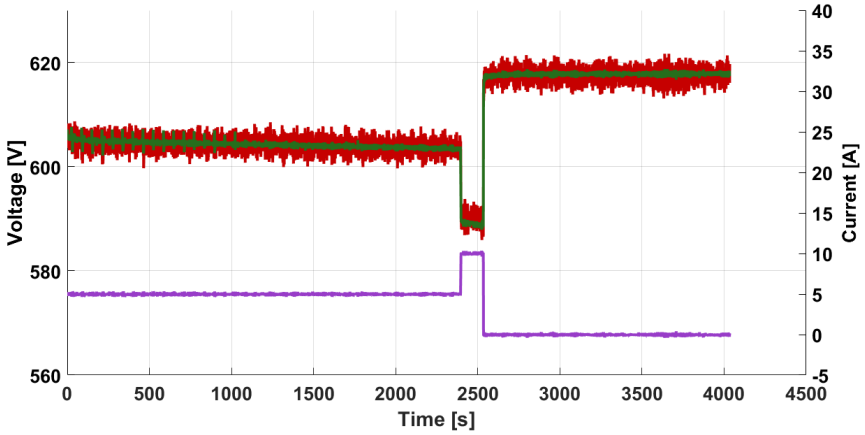

Figure 58: Comparison between the experimental voltage (red trace) and the one simulated with the improved model (green trace), related to step-current (violet trace) during a discharge test from 90% to 80% of SoC range.

5.8 SIMULATION RESULTS OF THE IMPROVED MODEL

The identified parameters allowed to develop a model to simulate the battery voltage time evolution during tests. A comparison between the model response and experimental curves has been investigated to verify the accuracy of the proposed model. The discharge test from 90% to 80% of SoC range and related to a step-current (violet trace), is shown in Fig.58. In this interval of SoC, the iron does not intervene, because the output voltage is over 564V during the entire test. The proposed model (green trace) follows the experimental voltage evolution (red trace), as confirmed by the error evolution shown in Fig.59, where can be seen that the percentage error is below 0.5%.

The discharge test from 40% to 30% of SoC range and related to step-current (violet trace), is shown in Fig.8. In this interval, the iron effect starts influencing the battery dynamic. In this case, the proposed model (green trace) results to be coherent with experimental voltage evolution (red trace), as shown in Fig.9, where can be seen that the error presents an approximately constant value during tests and remains below 2%.

In order to highlight the improvement obtained, a comparison with a model without the iron modelling has been reported in Fig.62. It shows the experimental curve (red trace) compared to the time evolution of the

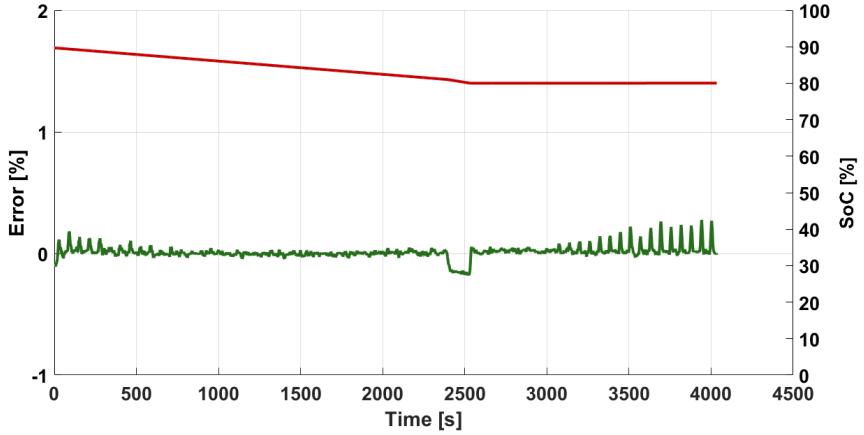

Figure 59: Error evolution in the 90%-80% SoC range. Green trace represents the evolution of the percentage error considering iron effects (improved model); red trace represents the SoC evolution.

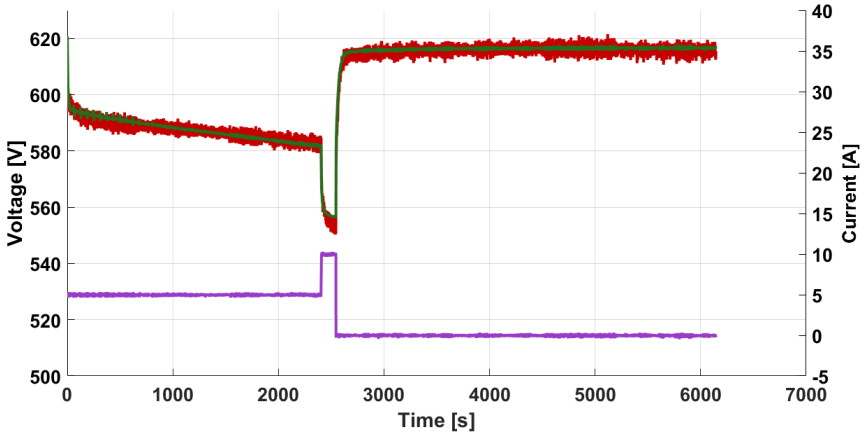

Figure 60: Comparison between experimental voltage (red trace) and the simulated voltage determined by the improved model (green trace), related to the depicted step-current (violet trace) and during a discharge test in the 40%-30% SoC range.

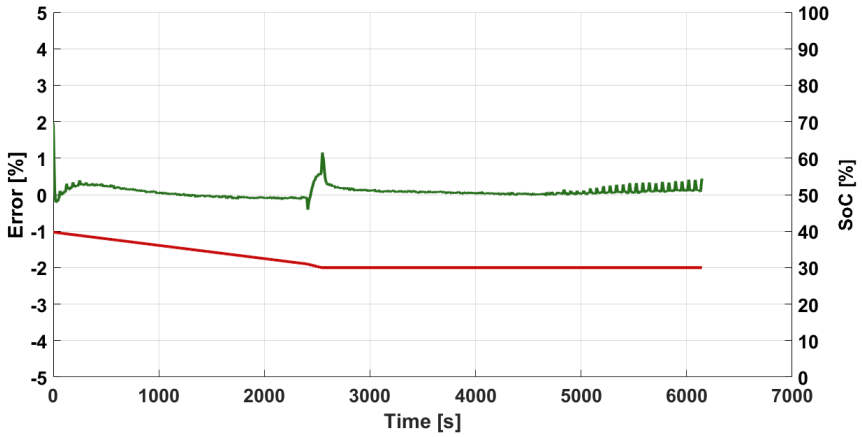

Figure 61: Error evolution related to 40%-30% SoC range. The green trace represents the percentage error considering iron effects (improved model); the red trace represents the SoC evolution.

simulated voltage, determined with the improved model (green trace), and the voltage without the iron modelling (blue trace), during the discharge phase in 90%-10% SoC range. The percentage error during the discharge phase in the same SoC range has been depicted in Fig.63. The error of the model without iron effect (blue trace) stands out more than the one of the improved model (green trace). This confirms the improvement obtained by taking into account the iron effect, especially at low SoC (red trace). The step current chosen allowed to identify more accurately the R_{ni}, and that explains the enhancement between the proposed model and the original one.

All the tests performed in the discharge phase, have been proposed, by the same method, to evaluate the model during the charge phase. The charge test from 30% to 40% of SoC range related to step-current (violet trace) is shown in Fig.64. The proposed model (green trace) results to be coherent with experimental voltage evolution (red trace), as shown in Fig.65, where can be seen that the error presents an approximately constant value during the test and remains below 0.5%. A comparison between the experimental curve (red trace) and the time evolution of the simulated voltage generated with the improved model (green trace), during the charge phase from 10% to 90% of SoC range, has been shown in Fig.66. The corresponding percentage error (green trace) during the charge phase is shown in Fig.67 and presents an approximately constant value during the test, re-

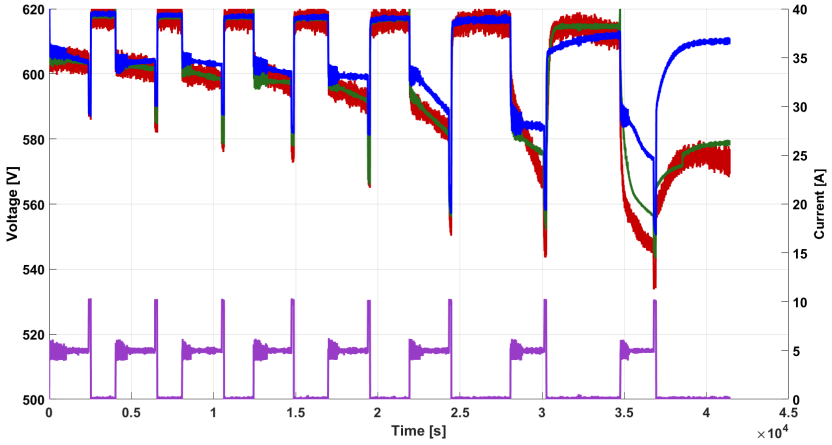

Figure 62: Comparison between experimental voltage (red trace), simulated voltage with proposed model (green trace) and simulated voltage without iron effect (blue trace) to step-current (violet trace) during the discharge from 90% to 10% of SoC.

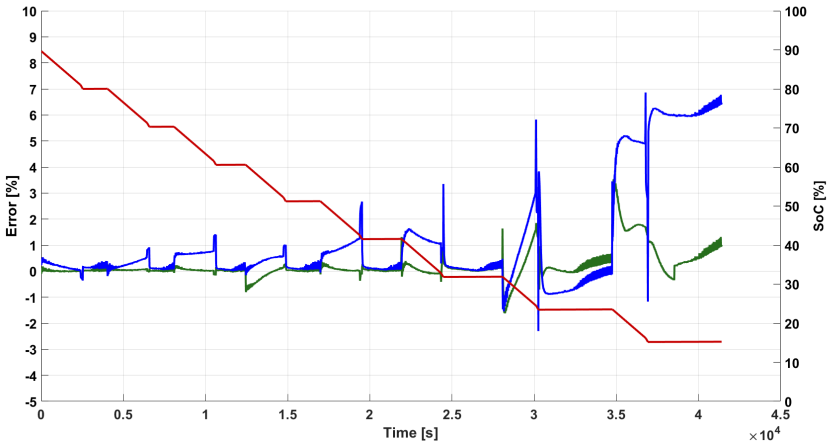

Figure 63: Percentage error evolution in the 90%-10% SoC range. Red trace represents the evolution of the SoC, green trace represents the evolution of the percentage error considering the iron effect and the blue trace represents the percentage error without considering iron effect.

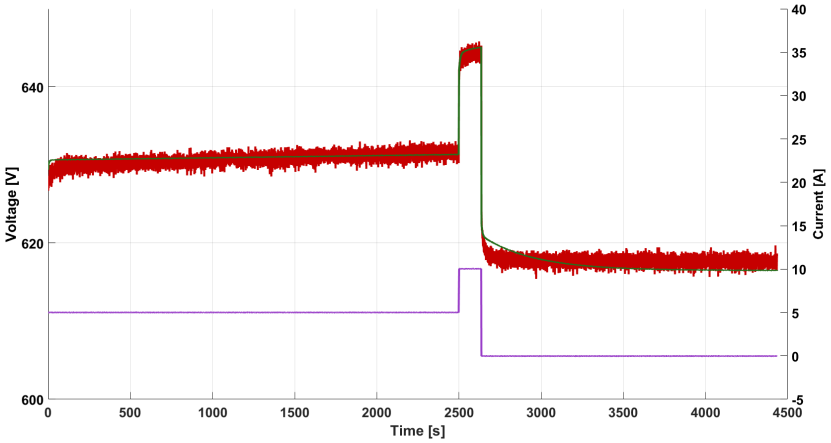

Figure 64: Comparison between experimental voltage (red trace) and the simulated voltage determined by the improved model (green trace), related to the depicted step-current (violet trace) and during a charge test in the 30%-40% SoC range.

maining below 1% until the 80% of SoC and thus confirming the accuracy of the proposed model also in a charge phase.

A discharge test with a power profile of a typical application of a battery with different currents has been implemented. In this test, the battery has been discharged from 90% to 10% of SoC. A comparison between experimental evolution (red trace), improved model (green trace) and model without iron effect (blue trace) has been done, as shown in Fig.68. The proposed model follows the experimental evolution with a maximum error lower than 1.5% for a SoC value greater than 30%, whereas the maximum error is 1.7% for a SoC value lower than 30%, as shown in Fig.69. Moreover, it is possible to evaluate the enhancement between the improved model and the one without the iron effect consideration.

Analogously, a charge test to simulate a typical application of a battery with a different current has been implemented. The battery has been charged from 10% to 90% of SoC. A comparison between experimental evolution (red trace) and the improved model (green trace) is shown in Fig.70. In this test, the maximum error is lower than 1,5%, as shown in Fig.71.

In this section a Thévenin circuit approach for Sodium Metal Halides Battery (SMHB) that considers the effects of iron reaction in the positive electrode has been investigated. A novel configuration of the Thévenin circuit, suitable for modelling the dynamic behaviour of SMHB has been proposed.

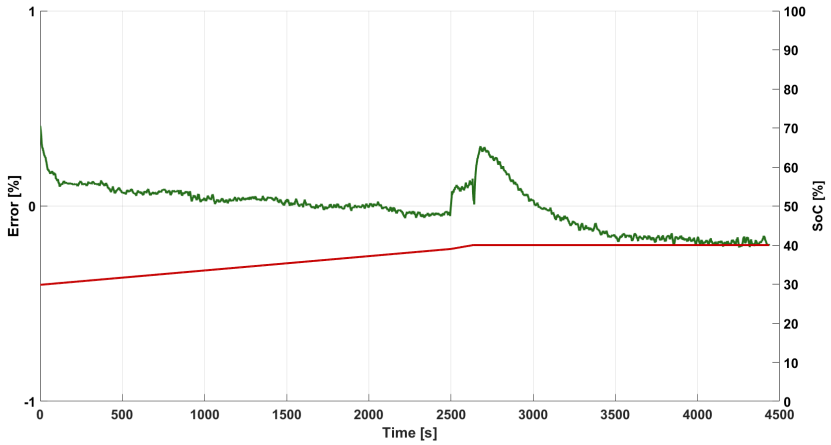

Figure 65: Error evolution related to 30%-40% SoC range. The green trace represents the percentage error considering iron effects (improved model); the red trace represents the SoC evolution.

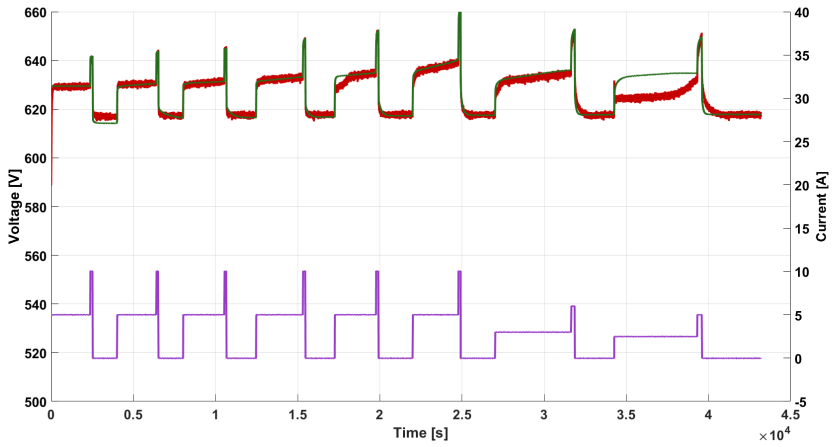

Figure 66: Comparison between the experimental voltage (red trace) and the one simulated with the improved model (green trace), related to step current (violet trace) and during the charge from 10% to 90% of SoC.

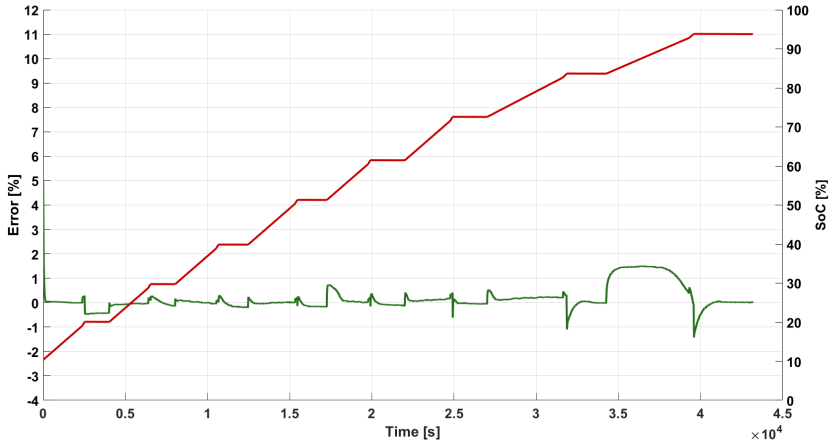

Figure 67: Error evolution related to 10%-90% SoC range. Red trace represents the SoC evolution, and green trace represents the evolution of the percentage error considering iron effect (proposed model).

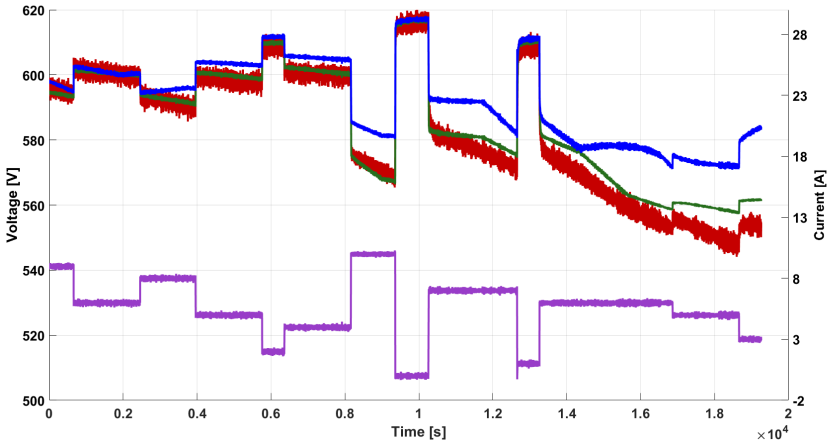

Figure 68: Comparison between the experimental voltage (red trace), the voltage simulating by the improved model (green trace) and the one simulated without considering the iron effect (blue trace), related to different current (violet trace) and during the discharge phase from 90% to 10% of SoC.

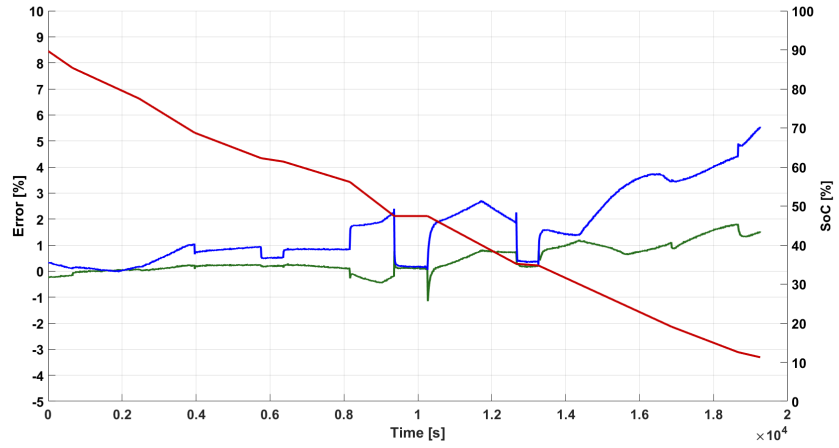

Figure 69: Error evolution related to 90%-10% SoC range considering different current. The red trace represents the SoC evolution, the green trace represents the evolution of the percentage error of the improved model, and the blue trace represents the percentage error without considering iron effect.

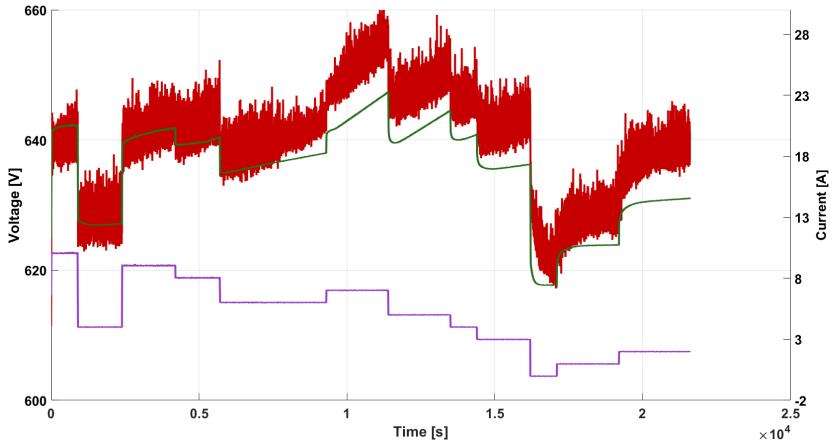

Figure 70: Comparison between the experimental voltage (red trace), the voltage simulating by the improved model (green trace) and the one simulated without considering the iron effect (blue trace), related to different current (violet trace) and during the charge phase from 10% to 90% of SoC.

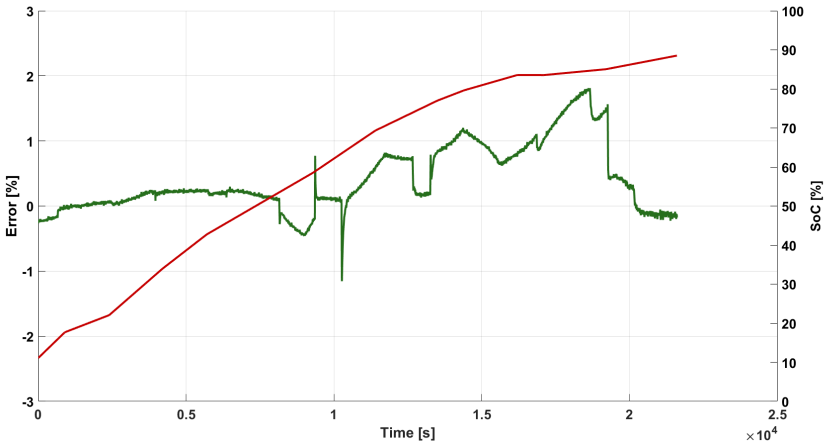

Figure 71: Error evolution related to 10%-90% SoC range considering different current. The red trace represents the SoC evolution, the green trace represents the evolution of the percentage error of the improved model, and the blue trace represents the percentage error without considering iron effect.

Moreover, the procedure for parameters identification has been described. Particular attention has been devoted to analysing the behaviour at low values of SoC. The comparison among the experimental and the simulation results, developed using the improved model, confirms the goodness of the proposed approach. In particular, in the 90%-30% SoC range, the relative error is lower than 1.5% with a peak value of 1.7% at lower SoC.

6

COUPLING BATTERY AND ACTIVE FILTER

This chapter will be presented a sizing criterion for an LC filter to be used as a suitable interface between an SMHB and a 4L-VSI for an AFS. This should provide active filtering and power balancing services simultaneously. In particular, reference is made to the AFS configuration proposed in 4 and to the SMHB electrical model presented in chapter 5. Based on these, a simplified AFS model achieved at first and LC filter design is carried out by identifying optimal inductance and capacitance pairs of values for any given SMHB current bandwidth. The effectiveness of the proposed approach has been validated through numerical simulations, which refer to advanced SMHB electrical model and regard different inductance and capacitance pairs of values for given SMHB current bandwidths and SoC.

6.1 SODIUM METAL HALIDES BATTERY

The SMHB modelling approach is described in Chapter 5. As reminder in Fig.72 the two RC branches model has been depicted together with the LC filter described in the following section.

6.2 THE LC FILTER

In order to couple the SMHB to the 4L-VSI, an LC filter should be employed. In Fig.73 is shown the block scheme of the proposed coupling system. In order to stabilise the input voltage of the 4L-VSI a capacitance C_{DC}, that represents the DC-link capacitor, must be introduced. Consequently, C_{DC} should be large enough in order to prevent fast and significant voltage fluctuations which may damage or make less effective 4L-VSI and AFS operation. Regarding the SMHB, fast current variations and ripple are unsuitable because they may reduce its performances and/or life cycle, hence an appropriate L_{DC} has also been considered.

In this context, it is worth noting that if no L_{DC} is included, large C_{DC} values determine relatively low voltage ripple, but may cause high current ripple on the SMHB. On the other hand, excessively small C_{DC} values

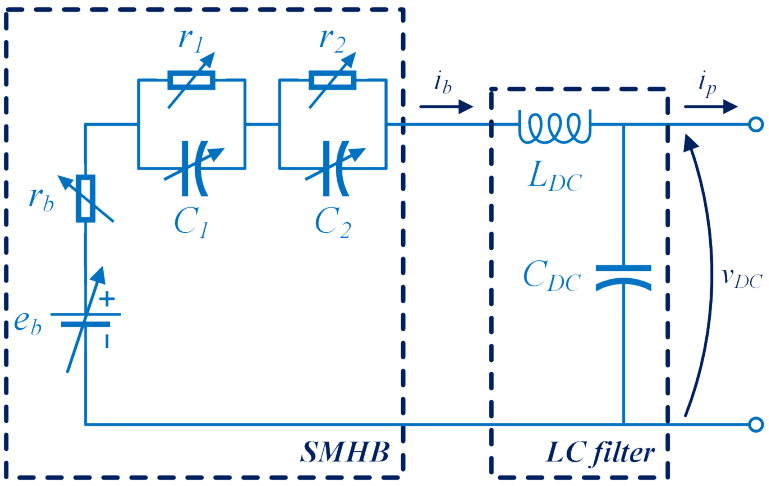

Figure 72: Block scheme of the Thévenin circuit model of the battery coupled with the LC filter.

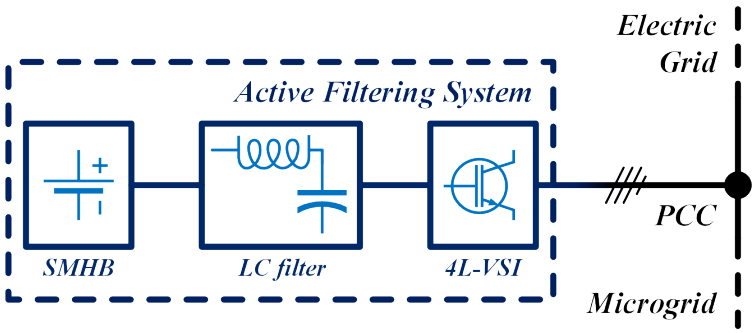

Figure 73: Simplified block scheme of the considered active filter.

lead to high voltage ripple on the input stage of 4L-VSI, which may be unacceptable for ensuring a proper AFS operation. Based on the previous considerations, an LC filter seems the most reasonable solution in order to prevent both high voltage and current ripple on DC-link and SMHB respectively. In this regard, a suitable design and sizing procedure can be employed in order to determine both L_{DC} and C_{DC} values properly, as detailed in the following section.

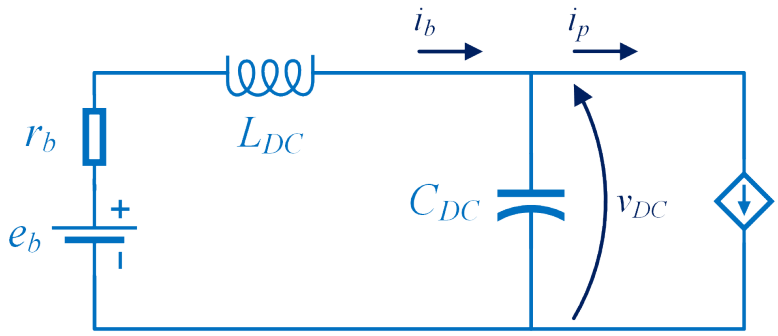

Figure 74: Simplified AFS model for LC filter design purposes.

6.3 LC FILTER DESIGN AND SIZING

6.3.1 *LC filter design*

For LC filter design purposes, the AFS model shown in Fig.72 can be simplified, as depicted in Fig.74. In particular, the two RC branches of SMHB can be both neglected due to their large capacitance and small resistance values. Furthermore, the DC current profile required by AFS operation can be modelled by a controlled current source (i_p). As a result, the following relationships hold:

$$e_b = r_b i_b + L_{DC}\frac{di_b}{dt} + v_{DC} \tag{26}$$

$$C_{DC}\frac{dv_{DC}}{dt} = i_b - i_p \tag{27}$$

in which e_b and r_b denote the SMHB open-circuit voltage and series resistance respectively, while i_b and v_{DC} are SMHB current and DC-link voltage.

By choosing i_b and vDC as the AFS state variables and e_b and i_p as the input signals, (1) and (2) can be expressed as

$$\frac{dx}{dt} = Ax + Bu \tag{28}$$

where

$$x = \begin{bmatrix} i_b \\ v_{DC} \end{bmatrix}, u = \begin{bmatrix} e_b \\ i_p \end{bmatrix} \tag{29}$$

$$A = \begin{bmatrix} -\frac{r_b}{L_{DC}} & -\frac{1}{L_{DC}} \\ \frac{1}{C_{DC}} & 0 \end{bmatrix}, B = \begin{bmatrix} \frac{1}{L_{DC}} & 0 \\ 0 & -\frac{1}{C_{DC}} \end{bmatrix} \tag{30}$$

Hence, with the aim of determine the dynamic relationship between x and u, the Laplace's Transformation has been applied to (28), leading to

$$X(s) = G(s)U(s) \tag{31}$$

in which G denotes the transfer function matrix between X and U and it could be expressed as

$$G(s) = (sI - A)^{-1}B = \begin{bmatrix} G_{11} & G_{12} \\ G_{21} & G_{22} \end{bmatrix} \tag{32}$$

where

$$G_{11} = \frac{1}{L_{DC}} \cdot \frac{s}{s^2 + \frac{r_b}{L_{DC}}s + \frac{1}{C_{DC}L_{DC}}} \tag{33}$$

$$G_{12} = G_{21} = \frac{1}{C_{DC}L_{DC}} \cdot \frac{1}{s^2 + \frac{r_b}{L_{DC}}s + \frac{1}{C_{DC}L_{DC}}} \tag{34}$$

$$G_{22} = -\frac{1}{C_{DC}} \cdot \frac{s + \frac{r_b}{L_{DC}}}{s^2 + \frac{r_b}{L_{DC}}s + \frac{1}{C_{DC}L_{DC}}} \tag{35}$$

Furthermore, in order to better investigate the relationship of i_b and v_{DC} with the inverter current i_p, only G_{12} and G_{22} can be considered and for argument's sake they have been redefined as G_b and G_{DC} respectively. Moreover, reference can be change to Fourier's Transformation rather than Laplace's one, leading to:

$$G_b(\omega) = \frac{1}{C_{DC}L_{DC}} \cdot \frac{1}{\left(\frac{1}{C_{DC}L_{DC}} - \omega^2\right) + \frac{r_b}{L_{DC}}j\omega} \tag{36}$$

$$G_{DC}(\omega) = \frac{1}{C_{DC}} \cdot \frac{\frac{r_b}{L_{DC}} + j\omega}{\left(\frac{1}{C_{DC}L_{DC}} - \omega^2\right) + \frac{r_b}{L_{DC}}j\omega} \tag{37}$$

Therefore, based on (36) and (37) it is possible to compute both current and voltage bandwidth (f_b and f_{DC}) as a function of L_{DC} C_{DC}, as highlighted by the following expressions:

$$\omega_b^4 + a_{1,b}\omega_b^2 + a_0 = 0 \tag{38}$$

$$\omega_{DC}^4 + a_{1,DC}\omega_{DC}^2 + a_0 = 0 \tag{39}$$

in which:

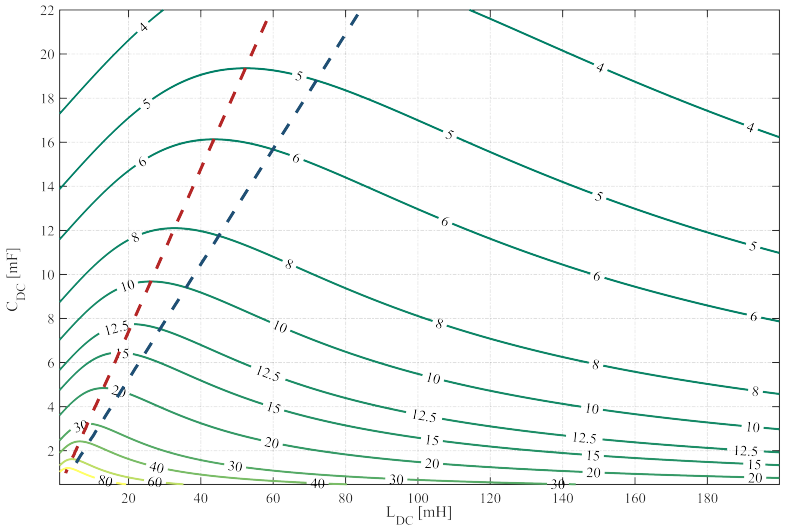

Figure 75: The f_b constant loci on the $L_{DC} - C_{DC}$ plane (level curves, labels in Hz), together with the MCPCB (in red) and MCPVB (in blue) loci.

$$\omega_b = 2\pi f_b, \qquad \omega_{DC} = 2\pi f_{DC}, \tag{40}$$

$$a_{1,b} = \left(\frac{r_b}{L_{DC}}\right)^2 - \frac{2}{C_{DC}L_{DC}}, \qquad a_0 = -\frac{1}{(C_{DC}L_{DC})^2} \tag{41}$$

$$a_{1,DC} = \left(\frac{r_b}{L_{DC}}\right)^2 - \frac{2}{L_{DC}C_{DC}} + \frac{2}{(r_b C_{DC})^2} \tag{42}$$

Based on (39) and (42) it is possible to depict suitable f_b and f_{DC} constant loci on the $L_{DC} - C_{DC}$ plane, by means of these a LC filter sizing procedure has been developed as explained in the following subsection.

6.3.2 *Lc filter sizing*

In Fig and Fig the f_b and f_{DC} constant loci on the $L_{DC} - C_{DC}$ plane have been shown. They are determined based on the specific SMHB described in 5 considering parameters highlighted in Tab.17 and Tab.16.

It can be seen how the more L_{DC} and C_{DC} increase, the more are achieved low bandwidth, as expected. However, choosing a generic f_b curve and starting from $L_{DC=0}$ in Fig.75 it is worth noting that the curve has a maximum. Consequently, such specific points belonging to different level curves

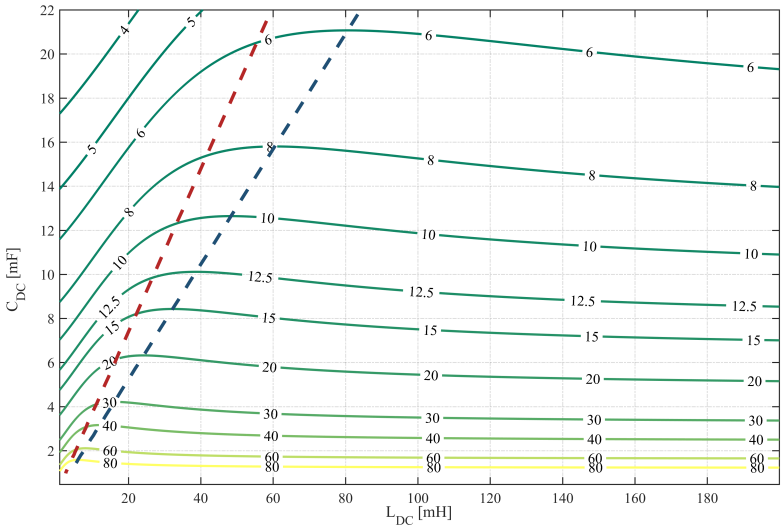

Figure 76: The f_{DC} constant loci on the $L_{DC} - C_{DC}$ plane (level curves, labels in Hz), together with the MCPCB (in red) and MCPVB (in blue) loci.

can be grouped into a Maximum Capacitance Per Current Bandwidth (MCPCB) locus. Similar considerations hold also for the f_{DC} constant loci depicted in Fig.76 leading to identify a Maximum Capacitance Per Voltage Bandiwidth (MCPVB).

Based on previous considerations, the optimal sizing of the LC filter for any given f_b value should thus correspond to the point belonging to MCPCB; this is proved by the fact that a further increase of L_{DC} beyond MCPCB would lead to a C_{DC} reduction in order to preserve the same f_b value. However, this increases f_{DC} unsuitably and it should be avoided. In this regard, it is worth noting that LC filter sizing should be based on MCPCB rather than MCPVB because LC filter must prioritize preserving SMHB performances and, thus, ensuring an appropriate f_b value.

In order to better investigate the effects of the model simplification described in section6.3.1 and of the SoC variation on LC filter sizing, a further theoretical analysis is performed by means of Bode diagrams, as shown from Fig.77 to Fig.80. Focusing on Fig.77 and Fig.78 at first, some mismatches between simplified and advanced model occur on G_b and G_{DC}, which leads to a slight underestimation of both f_b and f_{DC}. Much significant variations of G_b and G_{DC} occur with variation of the SoC, as highlighted in Fig.79 and Fig.80. Particularly, f_b and f_{DC} decrease with the SoC; this is due mainly to the increase of r_b, as shown in Table 18.

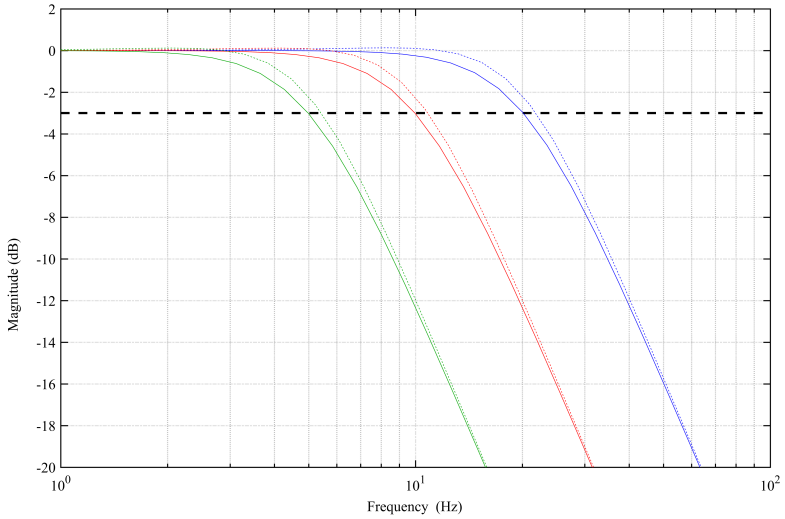

Figure 77: The magnitude of G_b achieved by imposing different (L_{DC}, C_{DC}) pairs of values belonging to MCPCB and by using the simplified (solid lines) and advanced AFS model (dashed lines): f_b = 5 Hz (green), 10 Hz (red) and 20 Hz (blue).

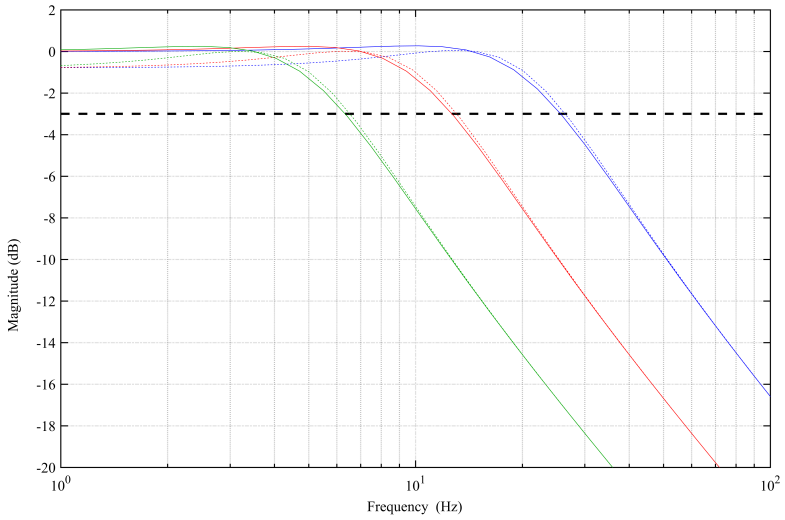

Figure 78: The magnitude of G_{DC}/r_b achieved by imposing different (L_{DC}, C_{DC}) pairs of values belonging to MCPCB and by using the simplified (solid lines) and advanced AFS model (dashed lines): f_b = 5 Hz (green), 10 Hz (red) and 20 Hz (blue).

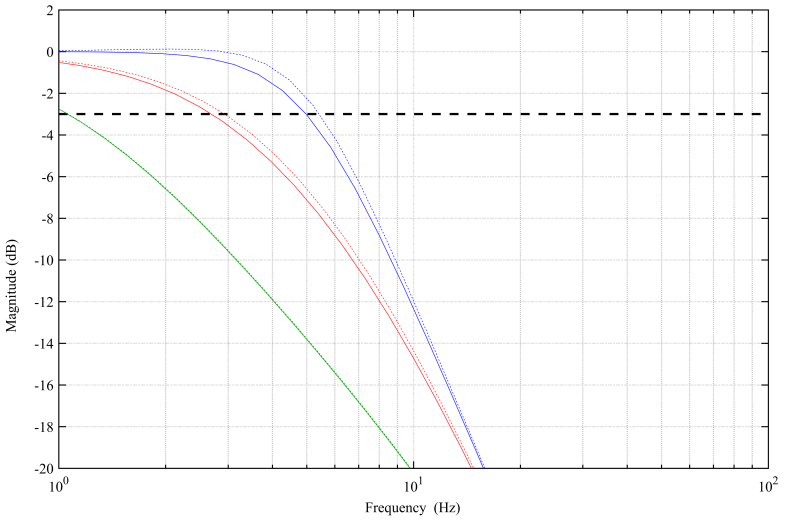

Figure 79: The magnitude of Gb achieved by imposing the (L_{DC}, C_{DC}) pair of values belonging to MCPCB and corresponding to f_b = 5 Hz and by using the simplified (solid lines) and advanced AFS model (dashed lines): SoC = 90% (blue), 60% (red) and 30% (green).

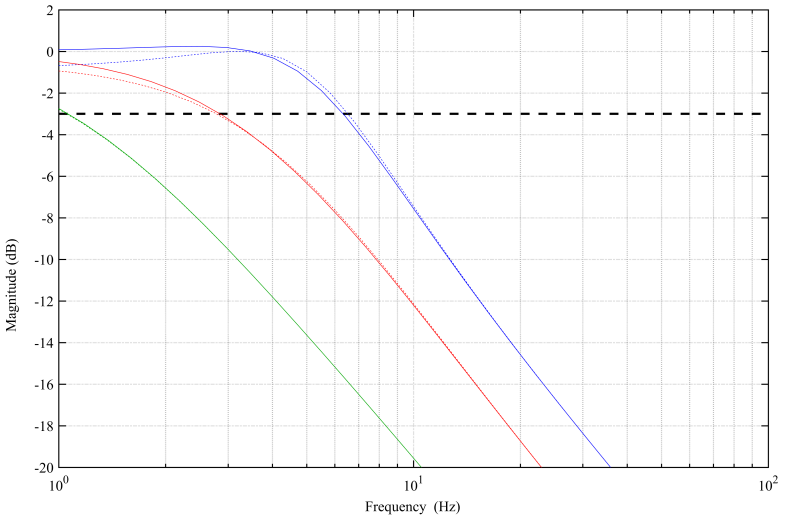

Figure 80: The magnitude of G_{DC}/r_b achieved by imposing the (L_{DC}, C_{DC}) pair of values belonging to MCPCB and corresponding to f_b = 5 Hz and by using the simplified (solid lines) and advanced AFS model (dashed lines): SoC = 90% (blue), 60% (red) and 30% (green).

SoC (%)	V_b V	r_b Ω	r_1 Ω	C_1 F	r_2 Ω	C_2 F
90	618.5	2.3263	0.0798	62.822	0.0502	1817.9
80	618.4	2.9228	0.1469	23.859	0.0542	1844.2
70	618.0	3.1394	0.2101	21.685	0.0685	2159.6
60	617.6	3.7187	0.2802	17.058	0.1008	1999.8
50	617.3	4.7105	0.3424	28.292	0.1328	2041.5
40	617.0	5.4863	0.5050	32.168	0.1874	2392.1
30	616.4	8.0521	3.0803	7.791	0.2844	1630.4

Table 18: SMHB parameters used for simulations.

However, SMHB benefits from such a bandwidth reduction because it means that slower current variations are allowed when the SoC becomes relatively low. Consequently, sizing the LC filter at the maximum SoC seems a reasonable choice for preserving SMHB appropriately.

6.4 SIMULATIONS

For the purpose of verify effectiveness of the proposed LC filter sizing, a simulation study has been performed in Matlab-Simulink environment by considering the AFS model shown in Fig.72. The current profile (i_p) absorbed by the 4L-VSI during his operation has been set based on the profile determined by simulating the AFS in the conditions described in 4. In order to decrease simulation time and efforts significantly without affecting the overall performances of the proposed AFS, the 4L-VSI has been replaced with an ideal current generator controlled by the previous calculated i_p. It is worth noting that this will not affects the sizing approach of the LC filter. In Fig.81 is highlighted the i_p current profile.

Regarding SMHB during tests, the starting SoC is imposed equal to 90%, while all the electrical circuit parameters have been modelled as SoC-dependent only (cf. 5 and in accordance with Table 18. The implemented simulations consider different LC filter sizes, which correspond to same f_b values with different ($L_{DC} - C_{DC}$) or distinct f_b values, as summarized in Table 19. In Fig. are highlighted working points shown in the above mentioned Table.

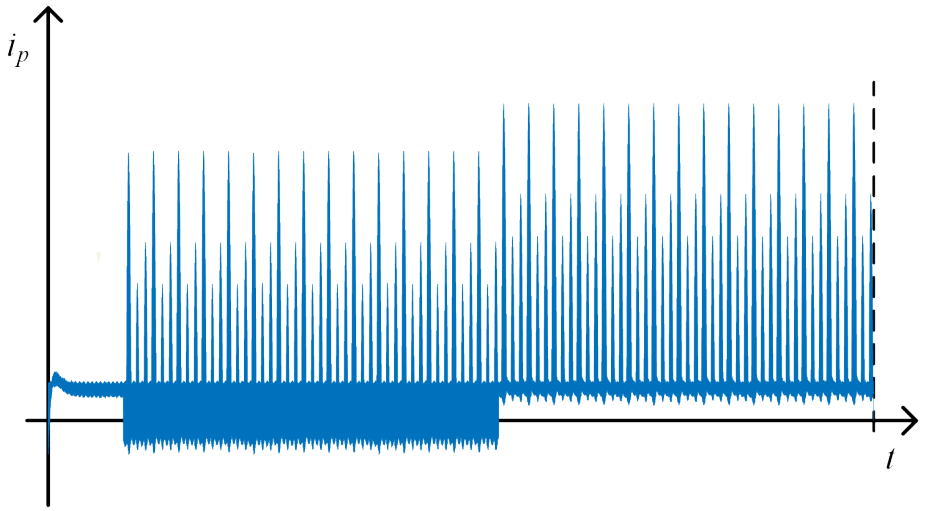

Figure 81: DC current profile of the 4L-VSI during active filtering.

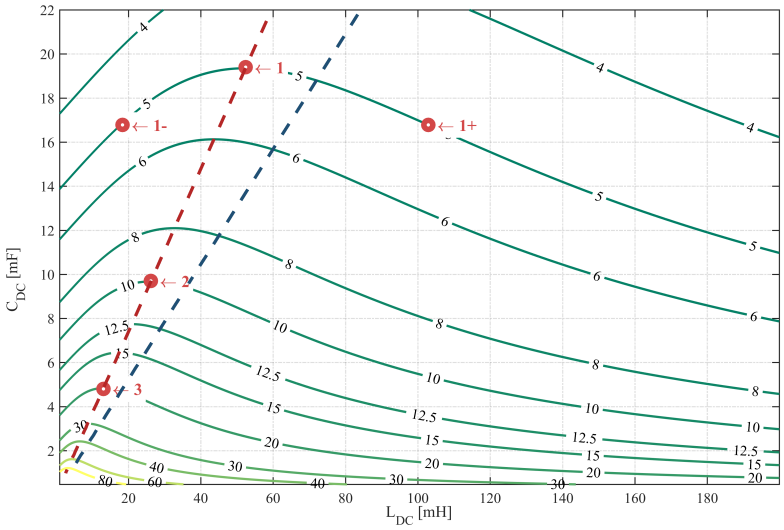

Figure 82: Cases considered for simulations (red dots).

case	$L_{DC} mH$	$C_{DC} mF$	$f_b Hz$	$f_{DC} Hz$
1	52.4	19.4	5	6.3
2	26.2	9.7	10	12.7
3	13.1	4.8	20	25.7
1-	18.37	16.8	5	5.3
1+	102.9	16.8	5	7.3

Table 19: Values of L_{DC}, C_{DC}, f_b, f_{DC} for each case studied.

Simulation firstly regards AFS operations at different f_b values by considering distinct $L_{DC} - C_{DC}$ belonging to MCPCB (cases 1, 2 and 3). Simulation results shown in Fig.83, Fig.84 and Fig.85 highlights the superior performances achieved in case 1 compared to cases 2 and 3, in particular in terms of current and voltage ripple. Moreover, the results highlight the decoupling between the power balancing services, provided by SMHB, and the active filtering services, sustained only in voltage by the SMHB.

In order to better point out the advantages of sizing the LC filter in accordance with the MCPCB, another simulation setting has been considered. It is characterised by the same value of f_b (equal to 5 Hz), and three different $L_{DC} - C_{DC}$ pairs of values (case 1-, 1 and 1+ in Table 19 and Fig.82). In particular, case 1- corresponds to an operating point of the level curve at $f_b = 5Hz$ on the left of the MCPCB, while case 1+ corresponds to an operating point on the same level curve but on the right of the MCPCB, as reported in Fig.82.

Hence, simulation results depicted in Fig.83, Fig.86 and Fig.87 reveals that the best performances are still achieved in case 1, namely selecting the $L_{DC} - C_{DC}$ pair of values on the MCPCB. The event is easily explained considering the lower L_{DC} and C_{DC} values used in case 1- lead to increased current and voltage ripple compared to case 1. Likewise, case 1+ is characterised by higher L_{DC} and lower C_{DC} and for this reason there is not any significant benefit to SMHB current ripple but, as expected, a non-negligible current overshoot is introduced and the voltage ripple is increased.

The last simulation has been performed with reference to case 1 by assuming different SMHB SoC. Results of these simulations are shown in Fig.88: it can be seen that SMHB dynamic performances decrease significantly with the diminishing of the SoC, due to the corresponding increase of r_b. In conclusion, SMHB is preserved more at low SoC values, thus confirming the effectiveness of the proposed sizing approach.

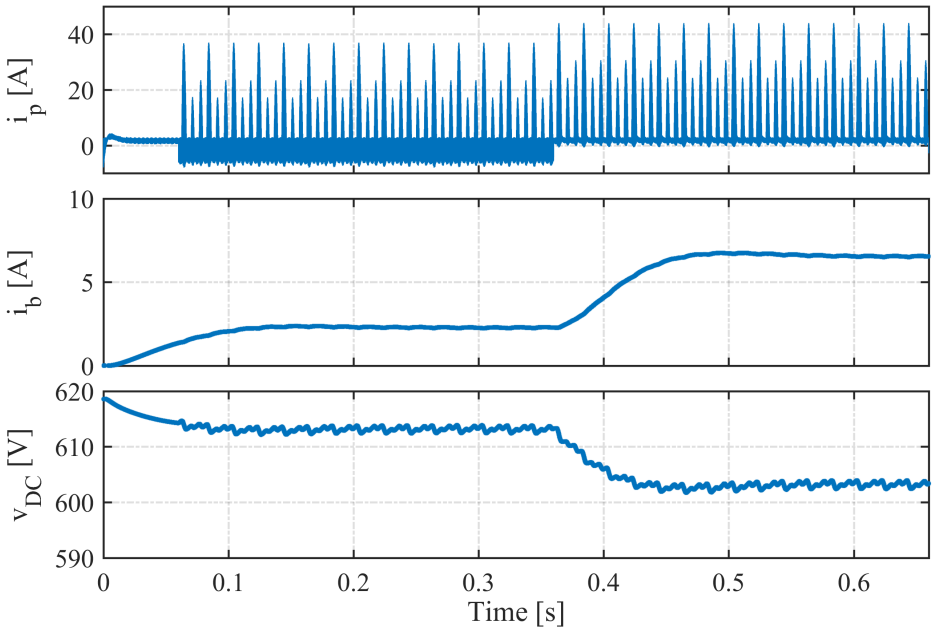

Figure 83: Simulation result achieved on MCPCB of case 1.

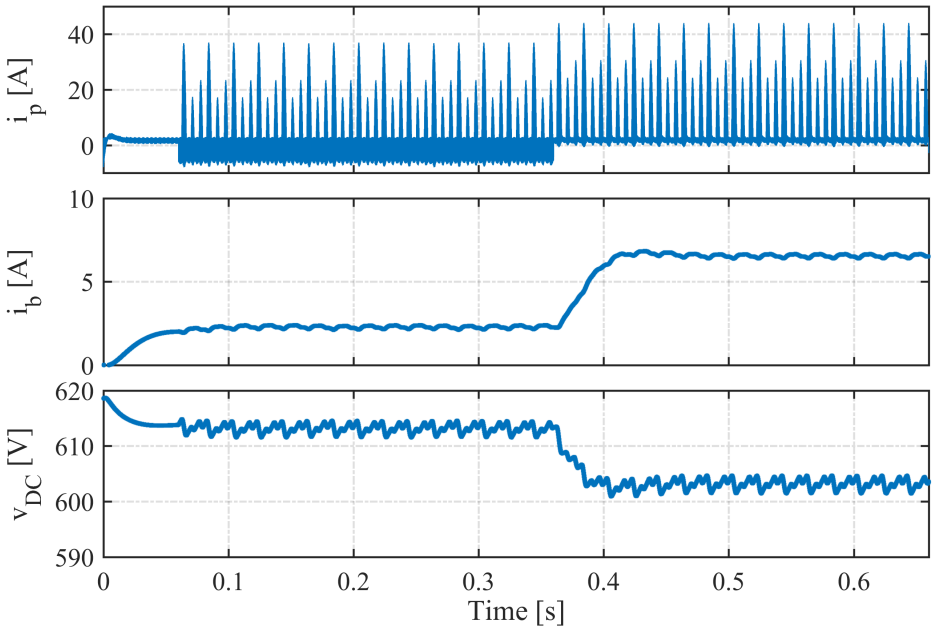

Figure 84: Simulation result achieved on MCPCB of case 2.

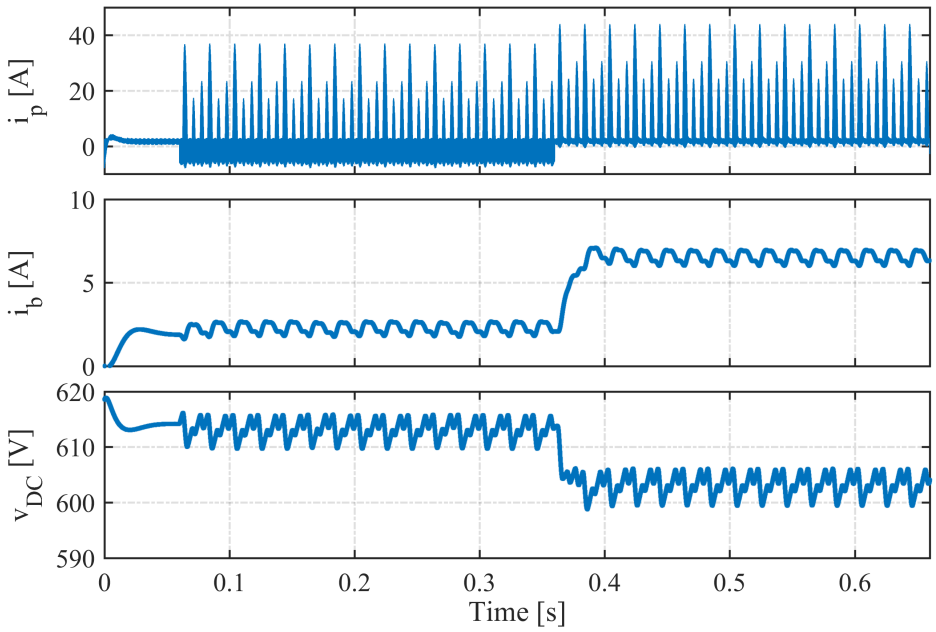

Figure 85: Simulation result achieved on MCPCB of case 2.

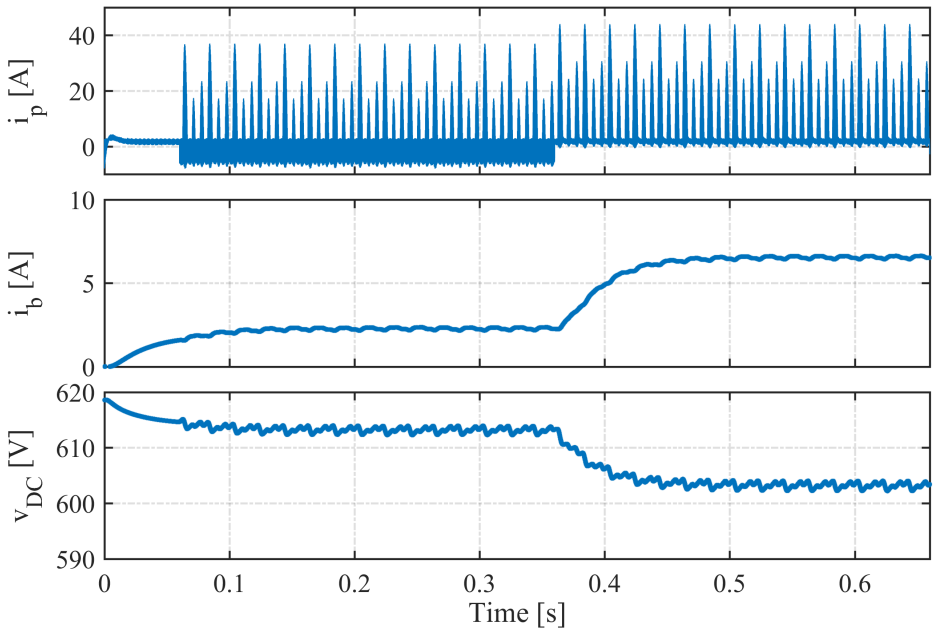

Figure 86: Simulation result achieved with $f_b = 5Hz$ with $L_{DC} - C_{DC}$ pair related to case 1-.

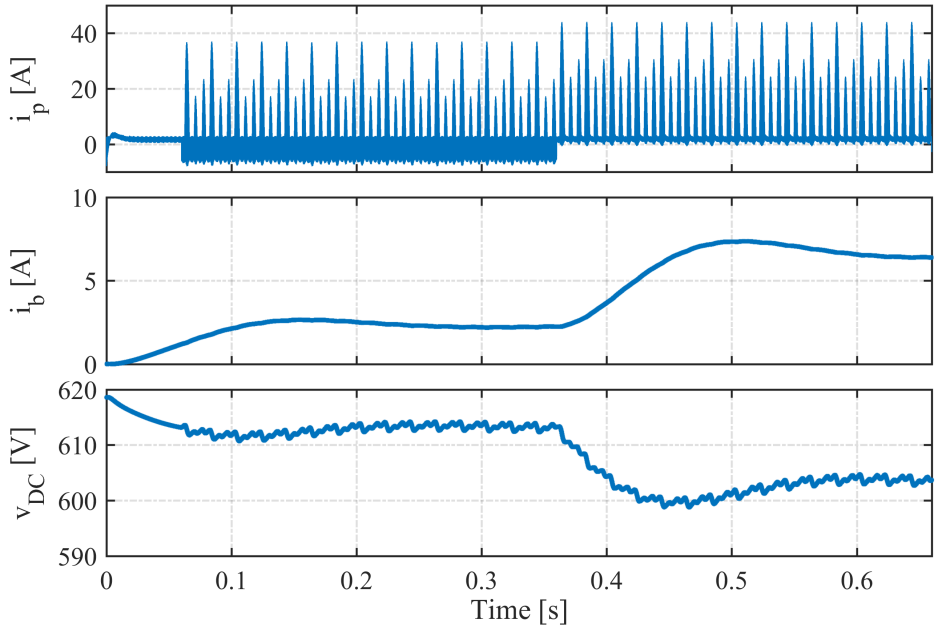

Figure 87: Simulation result achieved with $f_b = 5Hz$ with $L_{DC} - C_{DC}$ pair related to case 1+.

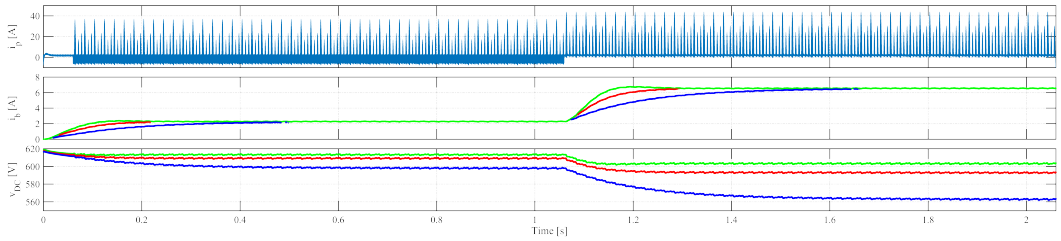

Figure 88: Simulation results achieved in case 1 for different SMHB state of charge: SoC = 30% (blu), 60% (red) and 90% (green).

6.5 CONCLUSION AND FORTHCOMING RESEARCH

In this chapter has been presented a suitable sizing criterion for an LC filter used in AFS applications. The LC filter represents the coupling component between the SMHB and the 4L-VSI, thus it has been sized with the aim of prevent SMHB from handling fast and sudden current variations, as well as for minimizing DC-link voltage ripple. The theoretical analysis presented in this chapter leads to identify a suitable locus on the $L_{DC} - C_{DC}$ plane, namely the Maximum Capacitance Per Current Bandwidth (MCPCB); in accordance with this, both L_{DC} and C_{DC} can be chosen easily for any given SMHB current bandwidth. The advantages of choosing the couple (L_{DC}, C_{DC}) on MCPCB has been proved by numerical simulations. The proposed sizing approach could be improved further by accounting for advanced SMHB model, especially for the dependency of electrical circuit parameters on the state of charge; this and other aspects will be investigated in future works.

7

AN ADVANCED FBM OF HESS FOR MICROGRIDS

As highlighted in chapter 4 and in particular in the block diagram of Fig.43, the charging and discharging logic of the SMHB battery can be determined through a strategy of optimization of the same. This chapter presents a control strategy for HESS with a Frequency Based energy Management. The battery charge and discharge set point could therefore be determined with a strategy of this type.

7.1 MICROGRID AND HESS MODELING

An MG is generally made up of several distributed generators and loads, clustered as shown in Fig.5 in Chapter 1. It is thus possible to define its residual power at the PCC as

$$r = \sum_i p_i + \sum_j l_j \tag{43}$$

in which p_i and l_j denote the power delivered by the i-th generator and drawn by the j-th load respectively. Particularly, p_i is always positive, whereas l_j is always negative. Consequently, an MG acts as either a load or generator depending on the sign of r. Assuming the HESS coupled with the PCC directly, the power balance at that node can be easily expressed as

$$g = r + s \tag{44}$$

where s and g denotes the overall power exchanged by the MG with the HESS and the main grid respectively. A positive s value thus means that HESS is discharging, the opposite occurring over an HESS charging process.

7.1.1 *Hybrid energy storage system*

The HESS considered in this paper is made up of two energy storage units, namely electrochemical batteries (B) and supercapacitors (S). Consequently, HESS overall power is made up of two contributions as

$$s = s_B + s_S \tag{45}$$

where s_B and s_S denote the power exchanged by batteries and supercapacitors respectively. Similarly, the overall energy stored in the HESS can be expressed as

$$e = e_B + e_S \tag{46}$$

in which e_B and e_S vary in accordance with s_B and s_S respectively.

Denoting by η_c and η_d the charging and discharging efficiency, the energy time variation of both batteries and supercapacitors can be defined as

$$\frac{de_X}{dt} = \Big(\frac{1}{\eta_{d,X}}\frac{s_X + |s_X|}{2} + \eta_{c,X}\frac{s_X + |s_X|}{2}\Big), X \in \{B, S\}. \tag{47}$$

Furthermore, power and energy of both B and S are bounded in accordance with appropriate constraints as

$$s_{X,min} \leqslant S_X \leqslant S_{X,max}, X \in \{B, C\} \tag{48}$$

$$e_{X,min} \leqslant e_X \leqslant e_{X,max}, X \in \{B, C\} \tag{49}$$

in which upper and lower boundaries depend on the specific energy storage technology, size and operating conditions. In this regard, it is worth noting that supercapacitors power constraint is much more relevant than their energy constraint since they are employed for MG power services, which are generally characterized by a high-frequency and poor energy content. Different considerations should be made for B energy and power constraints, which are both of paramount importance in order to provide energy services appropriately. Consequently, a suitable B energy and power management cannot be achieved by means of a frequency-based power split criterion only, thus requiring a more advanced algorithm, as detailed in the following section.

7.2 FILTER-BASED HESS ENERGY MANAGEMENT

The overall block control scheme of the proposed frequency-based HESS energy management FBM is depicted in Fig.90.

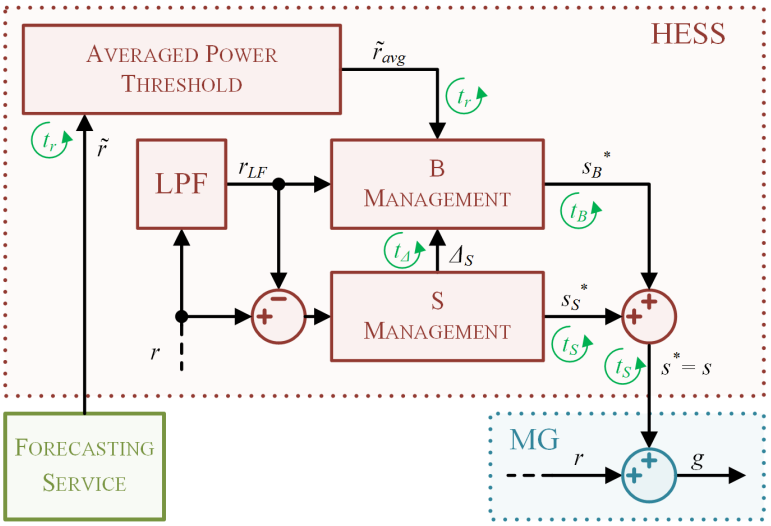

Figure 89: Overall block control scheme of the frequency-based HESS energy management proposed, in which LPF denotes the low-pass filter

It can be seen that the low-frequency content of the MG residual power profile (r_{LF}) is determined in real-time by an appropriate digital low-pass filter, whose transfer function in the frequency domain is depicted in Fig. 3.

This does not account for magnitude ripple, while the transition band has been chosen between 1.11 mHz and 8.33 mHz.

Since r_{LF} is generally characterized by a significant energy content, batteries could hardly compensate for such a large MG residual power profile due to both power and energy constraints. Particularly, since peak shaving is concerned, r_{LF} should be deprived of its average power component, thus reducing its energy content significantly. This could be computed based on forecasted MG residual power profile over a given time horizon T. Consequently, by taking into account batteries charging and discharging efficiencies in providing a full peak-shaving service, $\tilde{r}_{avg}$ can be computed by solving the following equation:

$$\int_t^{t+T} \left(\alpha_B (\tilde{r}_{avg} - \tilde{r}) + \beta_B |\tilde{r}_{avg} - \tilde{r}| \right) dt = 0 \tag{50}$$

where α_B and β_B depend on batteries charging and discharging efficiencies shown in the following

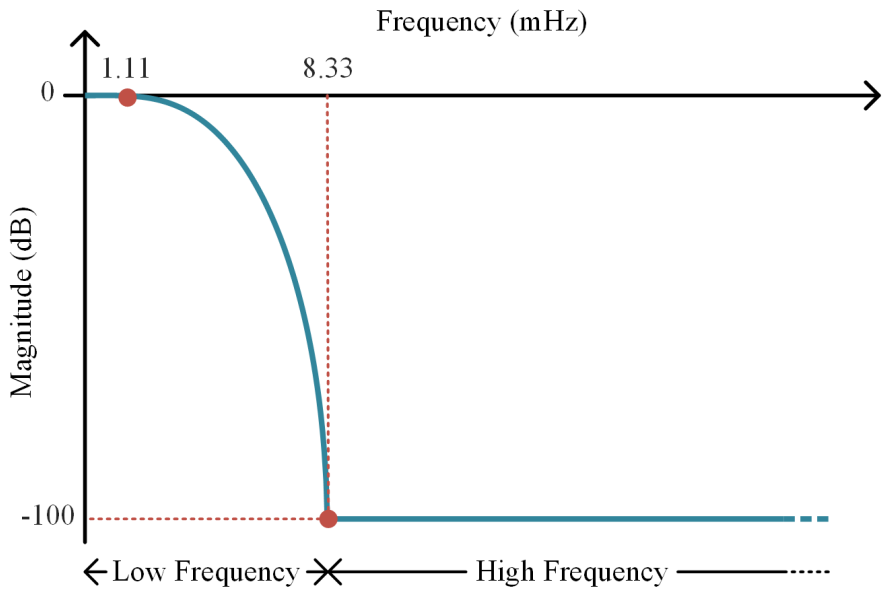

Figure 90: Transfer function of the LPF employed for the FBM.

$$\alpha_B = \frac{1}{2}\left(\frac{1}{\eta_{d,B} + \eta_{c,B}}\right),$$
$$\beta_B = \frac{1}{2}\left(\frac{1}{\eta_{d,B} - \eta_{c,B}}\right). \tag{51}$$

The batteries power profile could be thus determined in real-time in accordance with its power and energy constraints as

$$s_B = \left(-r_{LF} + \tilde{r}_{avg}\right)\Big\rangle_{s_{S,min}}^{s_{S,max}} \tag{52}$$

in which $\tilde{r}_{avg}$ can be updated every t_r in order to benefit from more accurate forecasting and batteries energy status. However, employing (**??**) does not usually lead to adequate performances of batteries in providing peak-shaving, unless large battery capacity is employed. This is because the battery is rapidly filled in as soon as r_{LF} overcomes $\tilde{r}_{avg}$. The opposite occurs when r_{LF} drops below $\tilde{r}_{avg}$, namely the battery is quickly charged to its rated capacity. Consequently, the battery acts for short time periods only, which do not usually correspond to r_{LF} peak values, as highlighted in Fig.91.

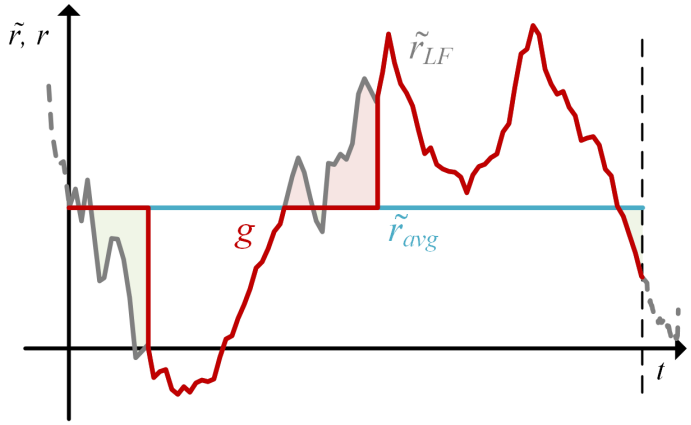

Figure 91: An example of MG residual power profile, together with the battery power profile synthesised in accordance with (52)

Hence, in order to avoid poor peak shaving capability, two additional power thresholds can be defined based on the battery energy constraint, as shown in Fig.92.

In particular, positive and negative power thresholds ($\tilde{r}^+$ and $\tilde{r}^-$) can be determined by the iterative procedure summarized in Fig.93.

Starting from $\tilde{r}^+ = \tilde{r}^- = \tilde{r}_{avg}$, the B power profile provided by (10) is considered at first, together with the corresponding B energy evolution. Since this does not generally comply with (49), if the first violation implies overcoming $e_{B,max}$, $\tilde{r}^+$ is increased in order to reduce the energy drawn by the battery in accordance with the following equation:

$$S_B = \left(-r_{LF} + \tilde{r}^+\right)\Big\rangle_{S_{B,min}}^{0} + \left(-r_{LF} + \tilde{r}^-\right)\Big\rangle_{0}^{S_{B,max}} \tag{53}$$

Therefore, e_B is computed again in accordance with (53) and a new iteration starts: if another violation is detected, $\tilde{r}^+$ is increased or $\tilde{r}^-$ is decreased in order to reduce the energy exchanged by the battery with the MG appropriately. The proposed procedure ends when the s_B profiles given by (53) leads to an e_B profile that complies with (49), meaning that the optimal pair of thresholds have been achieved, like the case shown in Fig.92. In conclusion, the supercapacitor power profile is computed directly in real-time in accordance with the high-frequency content of the residual power profile ($r - r_{LF}$), as already shown in Fig.90. Particularly, s_S can be determined as

$$s_S = \left(-r + r_{LF}\right)\Big\rangle_{S_{S,min}}^{S_{S,max}} \tag{54}$$

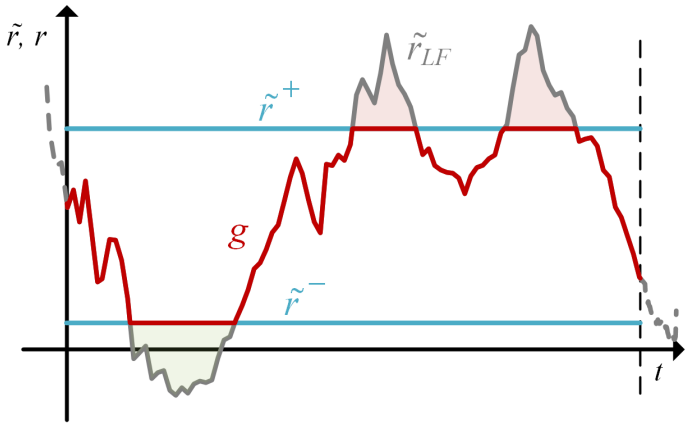

Figure 92: An example of MG residual power profile, together with the battery power profile synthesised in accordance with

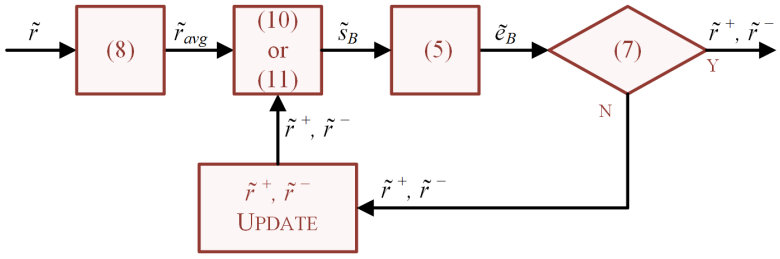

Figure 93: Flowchart of the proposed FBM energy management strategy.

Table 20: Frequency based HESS management.

e_B	$= e_{B,max}$	$< e_{B,max}$ & $> e_{B,min}$	$e_{B,min}$
s_B^*	0	$\left(-r_{LF}+\tilde{r}^+\right)\Big\rangle_{S_{S,min}}^{0} + \left(-r_{LF}+\tilde{r}^-\right)\Big\rangle_{0}^{S_{S,max}}$	0
e_C	$= e_{S,max}$	$< eS, max$ & $> e_{S,min}$	$= e_{S,min}$
s_C^*	0	$\left(-r+r_{LF}\right)\Big\rangle_{S_{S,min}}^{S_{S,max}}$	0

It is worth noting that 54 generally complies with 49 since a poor energy content of the high-frequency MG residual power profile is foreseen. Consequently, there is no need of advanced energy constraint management, as required by batteries. However, an appropriate average power is required by supercapacitors from batteries (δ_S) in case of excessive lower or higher supercapacitors state-of-charge, as pointed out in Fig.89. The HESS power profiles can be thus computed as summarized in Tab.20.

7.3 SIMULATIONS

The proposed FBM has been validated by means of a simulation study, which is carried out in the Matlab environment by referring to the MG of Borkum. It is a German island located in the North Sea (30.7 km^2, 5181 inhabitants) and it is characterized by both conventional and RES power plants, i.e. Combined Heat and Power (CHP), wind and photovoltaic. These are connected on either Medium Voltage (MV) or Low Voltage (LV), as highlighted in Tab.21.

In addition, the PCC consists of four submarine cables that enable a bidirectional power flow with the mainland. The HESS consists of an active configuration that allows battery and supercapacitor to be managed independently. Particularly, the battery consists of a Lithium Iron Phosphate battery ($LiFePO_4$) that is coupled to the DC-Link of the grid-tie inverter directly. Whereas the supercapacitor is coupled to the DC-Link through an appropriate DC-DC converter. Both battery and supercapacitor main specifications are resumed in Tab.22.

	Power Plant	Installed Power [kW]
MV	Wind	3600.00
	Photovoltaic	1386.70
	Total	4986.70
LV	Photovoltaic	953.44
	CHP	890.50
	Total	1843.94
MV + LV	Total	6830.64

Table 21: Borkum island electricity generation

	Parameter	Value
Battery	Rated Charging Power	-250 kW
	Rated Discharging Power	500 kW
	Total Energy	500 kWh
	Usable Energy	400 kWh
	Max Stored Energy	450 kWh
	Min Stored Energy	50 kWh
	Round-trip Efficiency	92 %
Supercapacitor	Rated Power	1108 kW
	Total Energy	9 kWh
	Usable Energy	6 kWh
	Max Stored Energy	11.4 kWh
	Min Stored Energy	2.4 kWh
	Round-trip Efficiency	90 %

Table 22: HESS parameters and rated values

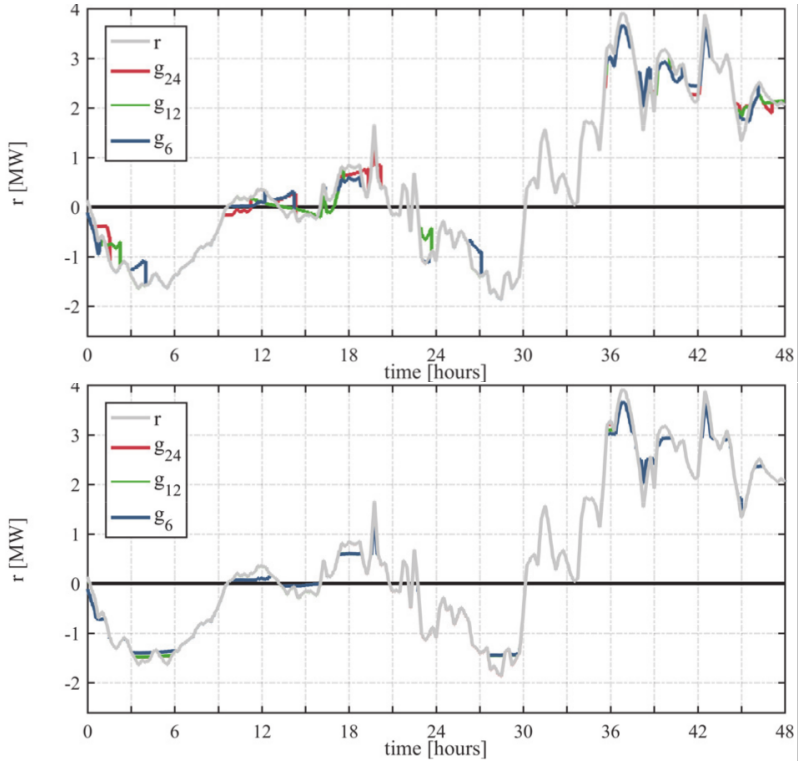

Figure 94: Residual and grid power profiles achieved by FBM-A (top) and FBM-B (bottom) over different time horizons.

7.3.1 *Simulation results*

Regarding simulations, two different FBMs have been considered: the first case (FBM-A) refers to the application of a single power threshold (r_{avg}), while the simulation of the second case (FBM-B) considers the two different power thresholds proposed in this paper ($\tilde{r}^+$ and $\tilde{r}^-$). The overall simulation results achieved in both cases are reported in Fig.94-12.

Focusing on Fig.94-96 at first, it can be seen that FBM-A exploits the HESS much more than FBM-B regardless of the chosen time horizon. However, FBM-B provides a better peak shaving capability due to the application of the proposed power thresholds, which enable the detection of both generation and load power peaks over the given time horizon. Whereas FBM-A fully charges/discharges the HESS as soon as the residual power profile crosses the average power threshold. Consequently, FBM-A is unable to wait for both generation and load power peaks and, thus, it shows a poor peak shaving capability, as expected.

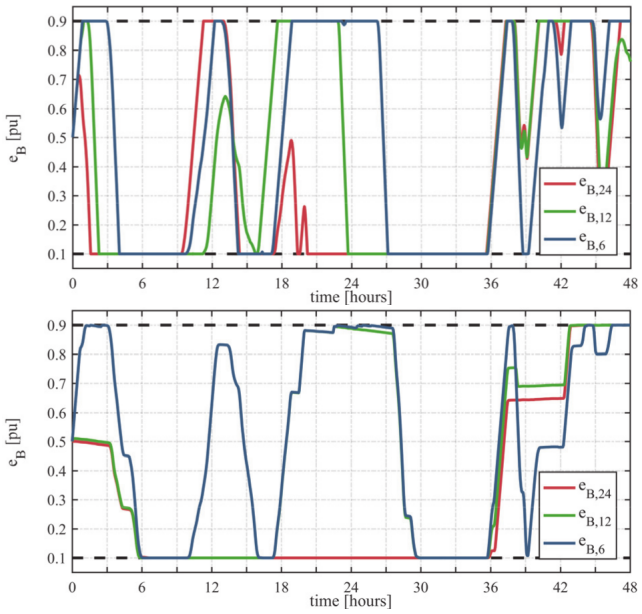

Figure 95: Evolutions of the battery SoC over each day achieved by FBM-A (top) and FBM-B (bottom) over different time horizons.

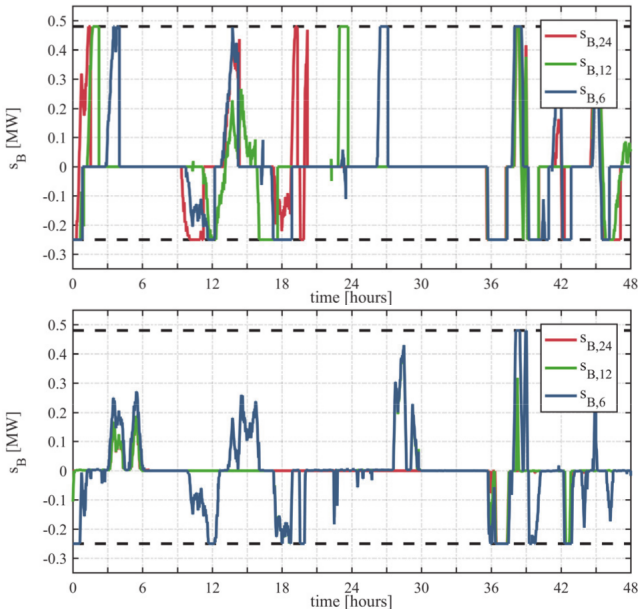

Figure 96: The battery power profiles over each day achieved by FBM-A (top) and FBM-B (bottom) over different time horizons.

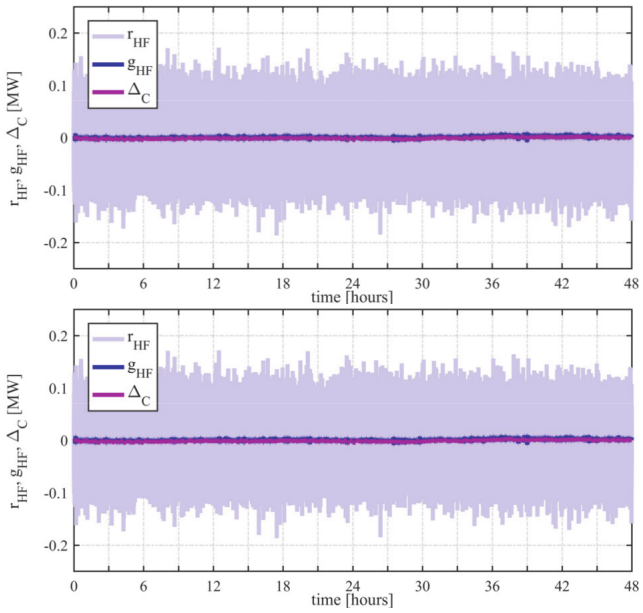

Figure 97: Power fluctuations on residual (r_{HF}, light purple) and grid power (g_{HF}, blue) by employing FBM-A (top) and FBM-B (bottom) at T = 24 h, together with the supercapacitor power demand (Δ_S, magenta.

Simulation results reveal also that both FBM-A and FBM-B exploits the HESS more as the time horizon decreases, as shown in both Fig.95 and Fig.96. However, increased HESS exploitation does not always correspond to improved peak shaving capability. Particularly, the time horizon has to be chosen in accordance with the periodicity of the residual power profile, namely it should be long enough in order to cover two subsequent generation and load peaks. However, if multiple generation and/or peaks are detected, only the greatest ones are reduced, as by FBM-B with T = 24 h. Consequently, excessively long time horizons should be avoided as well.

Very good performances are achieved by both FBM-A and FBM-B in compensating for the high-frequency power fluctuations occurring on residual power, as pointed out by Fig.97-99.

Furthermore, Fig.98 reveals that the supercapacitor never reaches its maximum or minimum energy thresholds, it thus being able to provide this power service continuously over the given time horizon.

In order to better highlight the peak shaving capability of both FBM-A and FBM-B, reference can be made to Fig.100, which shows the maximum averaged powers achieved when the MG acts as either a generator or a

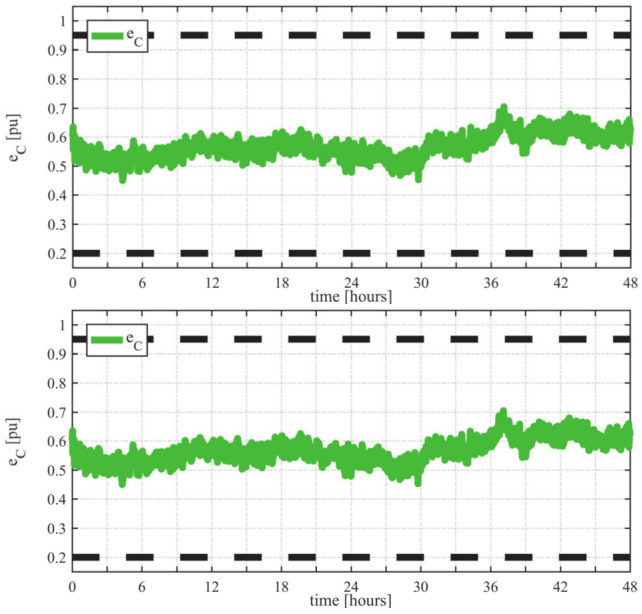

Figure 98: Evolution of the supercapacitor stored energy over each day (green) by employing FBM-A (top) and FBM-B (bottom) at T = 24 h.

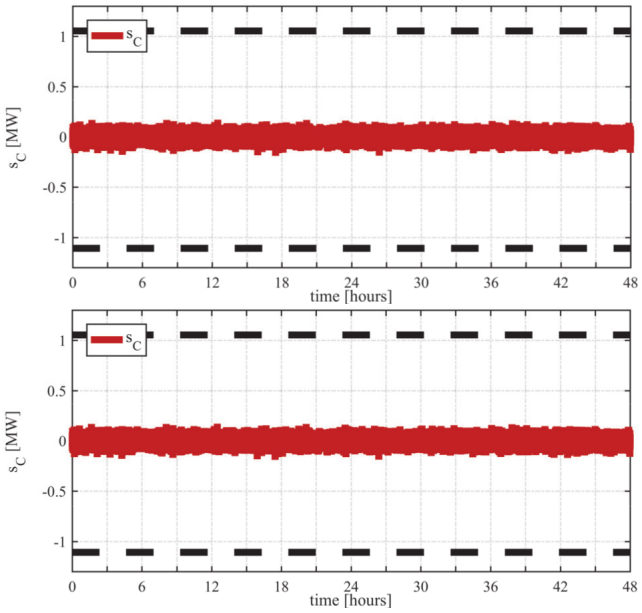

Figure 99: The supercapacitor power profile over each day (red) by employing FBM-A (top) and FBM-B (bottom) at T = 24 h.

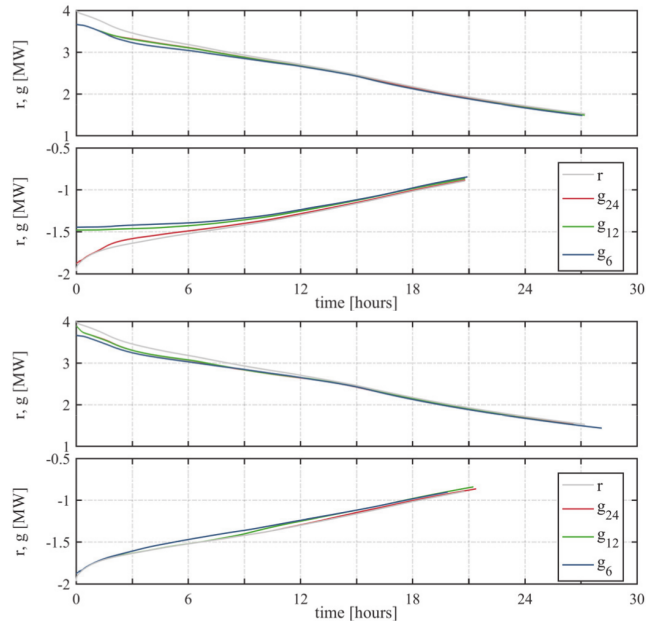

Figure 100: Pareto diagram of averaged r (gray) and g(red, green, blue) when the MG acts as generator and as a load: FBM-A (top) and FBM-B (bottom).

load over different time windows. For example, by choosing t = 3 h, the corresponding power values represents the averaged power achieved over the three hours of maximum generation and load. The results highlight the superior performances achieved by FBM-B, especially in reducing load powers during "peak" hours.

In conclusion, the HESS performances are summed up in Tab.23, which accounts for battery and supercapacitor cycling performances over a week. It reveals that the supercapacitor cycling is totally unaffected by the vari-

	HESS Elem.	**Time T [h]**		
		24	12	6
FBM-A	Battery	9.6	9.8	12.3
	Supercapactor	306.1	306.1	306.1
FBM-B	Battery	2.3	5.7	10.8
	Supercapacitor	306.1	306.1	306.1

Table 23: HESS cycling performances (cycles over one week).

ation of the time horizon in both cases, as expected. The comparison between battery and supercapacitor exploitation reveals the effectiveness of both FBM-A and FBM-B, which prevent the battery from excessive cycling due to the frequency-based power split criterion. However, battery cycles achieved by FBM-B increase significantly as T decreases. This occurs less for FBM-A, which is characterized by a greater number of cycle and, thus, an unsuitable battery overexploitation compared to FBM-B.

7.4 CONCLUSION

An advanced Frequency Based energy Management (FBM) of Hybrid Energy Storage System (HESS) for Microgrid (MG)s has been presented in this chapter. It consists of employing a suitable frequency-based power split criterion, together with a suitable management of battery power and energy constraints based on forecasted MG residual power profile. The effectiveness of the proposed approach is verified through numerical simulations, which highlight good FBM performances, especially by employing two different power thresholds over relatively short time horizons. However, peak shaving capability could be improved resorting to more advanced management approach, which may also reduce the energy exchanged between the MG and the main grid. This aspect will be investigated in future works.

8

EXPERIMENTAL IMPLEMENTATION OF THE AFS

As explained in the introduction, the research activity has been carried out in the laboratories of Electric Energy at the Piattaforma Energie Rinnovabili of Sardegna Ricerche, in Macchiareddu, Sardinia. This research center consists of three main laboratories: Electric Energy, Biomasses, Hydrogen. The installed power plants, storage systems and loads are included in a project aimed to convert the building to a microgrid, whose purpose is to demonstrate the feasibility and effectiveness of microgrid for an efficient energy management. These research activities are financed with the resource of the ROP ERDF 2014-2020 and are carried out as a setting of the *"Complex Project of Sardinia Research - Smart Grids for the efficient management of energy"*, which aims at the pursuit of the integration of DG, consumption and distributed storage, extended both to the thermal and to the mobility sector. The configuration of the Renewable Energy Platform in depicted in Fig.101.

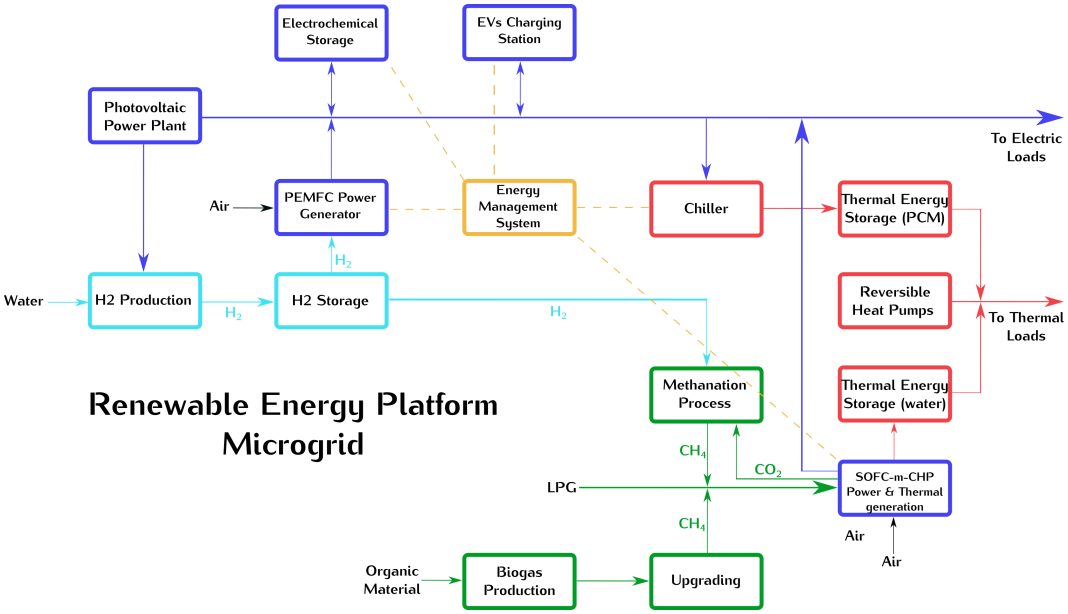

Figure 101: Reneable Energy Platform laboratories block scheme.

At the present time the power plant installed are the following:

- Traditional PV Power Plant of 18.70 kWp total, of which 7.74 kWp of amorphous silicon and 10.96 kWp of monocrystalline silicon. The PV plant is divided in two layers with two different orientation: South-East, 5.16 kWp monocrystalline silicon and 5.16 kWp amorphous silicon; South-West, 5.8 kWp monocrystalline silicon and 2.58 kWp amorphous silicon;

- A CPV power plant of 6.2 kWp, consisting of 90 module characterised by Fresnel lenses optics;

- Two Kostal storage systems, both based on lithium iron phosphate technology and characterised by a capacity of 9.6 kWh;

- Three LGchem storage system, based on lithium ion technology and characterised by a capacity of 6.4 kWh.

- A FIAMM High Temperature SMHB, Sonick ZEBRA with a capacity of 23.5 kWh.

The installation of the following systems has been also planned in the future:

- Monocrystalline silicon PV power plant of 25.38 kWp;

- Storage system based on lithium ion, characterised by a nominal capacity of 36 kWh;

- A Solid Oxide Fuel Cell (SOFC) powered by GPL, nominal power of 9kW aimed to cover the base load of the building.

The complex project considers also the implementation of an EMS aimed at real-time control of the power plants, storages and loads. In this context the realization of the active filter of the present work is also included.

Table 24: CompactRIO hardware characteristics.

Real-Time Controller	
CPU	Intel Atom E3845
Number of cores	4
CPU frequency	1.91 GHz
Memory	2 GB DDR3L
Solid-state drive	16 GB
Operative System	NI Linux Real-Time (64-bit)
FPGA board	
FPGA type	Xilinx Kintex-7 7K325T
Number of flip-flop	407600
Number of 6-input LUTs	203800
Number of DSP slices	840
Available block RAM	16020 kbits
Number of DMA channels	16
FPGA Memory	128 MB

For this purpose, the results obtained from the simulations carried out, shown in the previous chapters of this thesis, provided the right conditions for starting the experimental realisation of the active filtering system described. In order to take advantage of the previous programming experiences in the LABoratory Virtual Instrumentation Engineering Workbench (LabVIEW) environment and the hardware present in the Electric Energetic laboratories of the Macchiareddu Renewable Energy Platform, it was decided to develop the system in LabVIEW on the National Instruments CompactRIO (cRIO) platform. The cRIO model adopted, NI-9034, has the following characteristics:

The algorithm described in chapter 4 requires the acquisition of the network voltages at the PCC (V_1, V_2, V_3, V_n), of the currents absorbed by the load (i_1, i_2, i_3) and of the converter output currents (i_{f1}, i_{f2}, i_{f3}) needed for the functioning of the current loop. The algorithm also considers the acquisition of the neutral voltage V_n since the implemented modulation is a 3D Space Vector Pulse Width Modulation (3D-SVPWM). In order to fulfil the performance required by the application (described below), it is necessary that the acquisition process of the different quantities is as fast as possible and simultaneous, so as to be able to determine the variables calculated by

Table 25: NI-9220 characteristics.

C-Series 9220 module	
Number of channels	16 analog input channels
ADC resolution	16 bits
Type of ADC	SAR
Input Voltage Range	$\mp 10V$
Conversion time	10 μs minimum
Sample Rate	100 kS/s maximum
Input impedance	$> 1G\Omega$

Table 26: NI-9401 characteristics.

C-Series 9401 module	
Number of channels	8 DIO channels
Input/output type	TTL, single-ended
Input High	2 V min
Input Low	0.8 V max
Output High Sourcing 100 μA	4.7 V min
Output High Sourcing 2 mA	4.3 V min
Output Low Sourcing 100 μA	0.1 V min
Output Low Sourcing 2 mA	0.4 V min
Max Signal freq. 8 ch.	5 MHz
I/O propagation delay	100 ns max

the algorithm on the basis of the values of voltages and currents in the PCC referred to the same time instant. For this reason, the C-Series acquisition module chosen is the NI-9220, Tab.25 shows its main characteristics. The acquisition speed can be improved in the future thanks to the use of recent modules with higher performance.

The voltage and current probes used have analog output signals compatible with the selected module. As a load, a single half-wave rectifier with a resistance that can be set to three values ($45\Omega, 75\Omega, 120\Omega$) was realized to carry out the tests.

The gate signals are sent to the inverter by a C-Series module DIO NI-9401, which characteristics are summarised in Tab.26

Table 27: IPM characteristics.

On-Semiconductor IPM	
Supply voltage	450 V
Output current	30 A
t_{ON} at 30 A	0.6 μs
t_{OFF} at 30 A	0.9 μs
Max t_{ON} at 30 A	1.3 μs
Max t_{OFF} at 30 A	1.6 μs
Recommended Dead Time	2 μs

The power converter is an Intelligent Power Module (IPM) STK581U3C2D-E by On-Semiconductor mounted on an evaluation board of the same company. In Tab.27 are highlighted its main characteristics.

Due to the recommended value of 2 μs, the AFS is set in order to have a working period of 200 μs so that the Dead Time does not weigh excessively on the overall period. It is worth noting that the modulation frequency chosen is consequently equal to 5 kHz.

The algorithm has been developed in LabVIEW and, as a consequence of the requested performances, entirely through the use of the FPGA module packages. Programming in FPGA means finding the right balance between timing control (deterministic), high throughput, numerical precision and use of FPGA resources. Before explaining common methods to achieve this balance condition, it is useful to define the most used terms.

DETERMINISM , is one of the main features of real time applications. It represents the ability of an application to operate within a predetermined time interval. Higher determinism means lower jitter;

JITTER , indicates a variation on the desired Loop Cycle Time (LCT);

LATENCY , time required by the program to respond to an event, also defined as the time interval between an input and the corresponding output;

LCT , defined as the execution time of a cycle operation, or also as the time between the beginning of a cycle and the beginning of the next cycle;

REAL-TIME (RT) APPLICATION , it does not necessarily mean that it must have particularly short execution times ("fast application");

SCHEDULING , assignment of a priority level to different sub-processes.

THREAD , a subset of the operations of a program that share the same common target;

THROUGHPUT , represents the number of valid output per unit of time.

In particular, National Instruments define throughput as result of three factors [94]:

- The rate of the clock you are using to drive your design (cycles/time);
- The number of samples that the Intellectual Property (IP) or default LabVIEW blocks accepts per call (samples/call);
- The number of cycles that must elapse before your algorithm can be called again (cycles/call); this is also referred to as the Initiation Interval (II) or initiation period.

By this three factors, throughput can be defined as:

$$Throughput = \frac{ClockRate \cdot Samplespercall}{InitiationInterval} \tag{55}$$

Therefore, on the basis of equation 55 it is easy to see that throughput can be increased by acting on these three factors:

- Increasing the clock rate;
- Increasing the number of samples processed per call;
- Decreasing the initiation interval.

In the following are shown some programming strategies that allow to take action on the three factors listed above.

It is worth noting that increasing the clock rate doesn't means just increase its value because it could be impossible to execute all the required operations in a certain loop time causing a compilation failure. In order to increase the clock rate, the first thing to do is to separate the computationally expensive operations from the lighter ones, in two separate cycles:

a first slow cycle, possibly non-deterministic, a second one fast and deterministic. Another strongly helpful operations is to reduce the critical path, e.g. by parallelising operations.

Modifying the algorithm introducing parallel operations contributes also in increasing the number of samples/call. In the specific case of the AFS, for example, the scaling of input signals can be executed in parallel because it provides for every signals the same operations.

Moreover, numeric precision strongly affects computational time, clock rate and resource usage. Avoid over-estimating the accuracy and precision needed by the application, translates into choosing the numeric type characterised by the lower consumption of resources, higher clock rates and lower computational time associated. In fact, some operations require a number of "ticks" (the unit of measurement of the FPGA board clock cycles) which increases with the increase of the bits assigned to the input numerical values.

Among the various techniques aimed at increasing the throughput, it can not help but mention pipelining. In particular, the most famous example used to explaining how pipelining works is referred to laundry [95].

Assuming that the activity of a laundry is divided into the four main operations of washing, drying, folding of clothes, placing them in the wardrobe; and assuming that it receives four orders represented by the colours blue, yellow, green and red, the same laundry can complete the four orders by adopting two different strategies. The first strategy involves the execution of the four series orders, and if to simplify it is considered that each operation requires one hour, the whole process requires a total of sixteen hours. This strategy is shown at the top in Fig.102 But for each job, the washing phase remains unused for three hours, and this applies to each subsequent phase. Parallelisation allows using continuously every phase of the process. In fact, while the drying of the first job starts, nothing prohibits starting the washing of the second one. Consequently, while starting the folding phase of the clothes of the first order, the drying of the second and the washing of the third can be started. With this strategy, the four orders require a total of seven hours. The savings in terms of working hours is, therefore, nine hours. This strategy is depicted at the bottom in Fig.102.

The cited example makes it possible to better explain the concepts of latency and throughput. Both strategies are characterized by a four-hour latency, but they have very different throughput. The "series" strategy concludes a job every four hours. The pipeline strategy on the other hand,

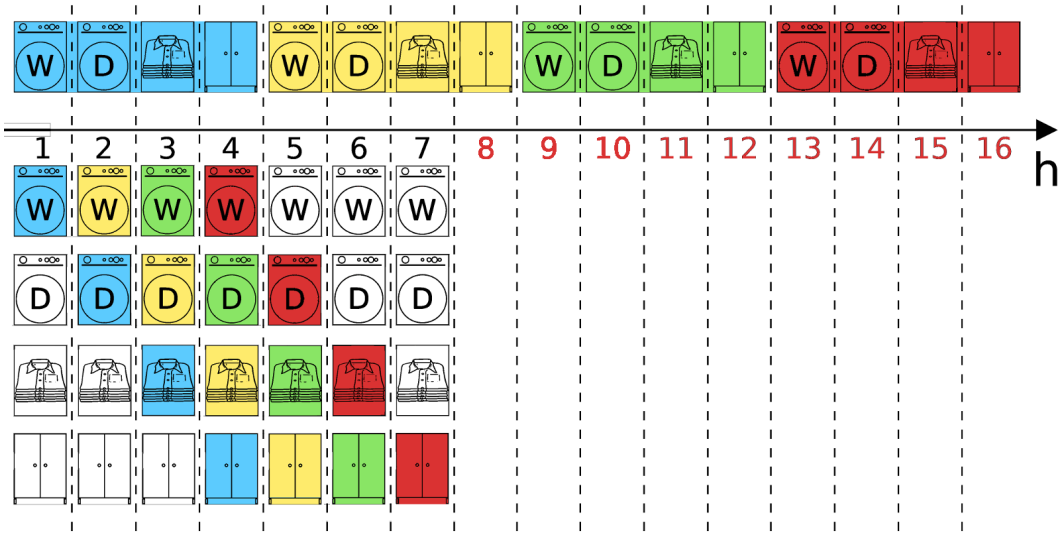

Figure 102: Comparison between the series strategy (top) and the pipelined one (bottom) of the operations in a laundry.

after a first three-hour start-up phase, concludes one job every hour, finishing as already said nine hours in advance. The effects of this strategy are more noticeable improvements if applied for example to industrial productions, where the number of products produced every hour takes on a significantly different weight. Furthermore, it should be considered that in the steady-state condition with the pipeline strategy, all production phases remain active at the same time. But with the "series" strategy, they remain inactive throughout the duration of the latency. In LabVIEW, the FPGA programming is optimised by using the structure called Single Cycle Timed Loop (SCTL). In fact, this cycle ensures that the code present inside it is executed within a "clock cycle" of a specific FPGA clock. Compiling a program that uses the SCTL returns a time violation in case it is not possible to execute the code within a single cycle. Applying the "pipeline" strategy to the code allows to subdivide it into steps that require less execution time and be able to satisfy the time constraints imposed by the SCTL clock.

Another important procedure adopted in the realization of the algorithm is the handshaking. This can only be used within SCTL and provides for the activation of a register on an elementary block. This register acts as a FIFO of a single element. The handshake takes into account the computational cost, in terms of tick, of each block on which it is activated by providing a digital output signal that defines whether the calculated value

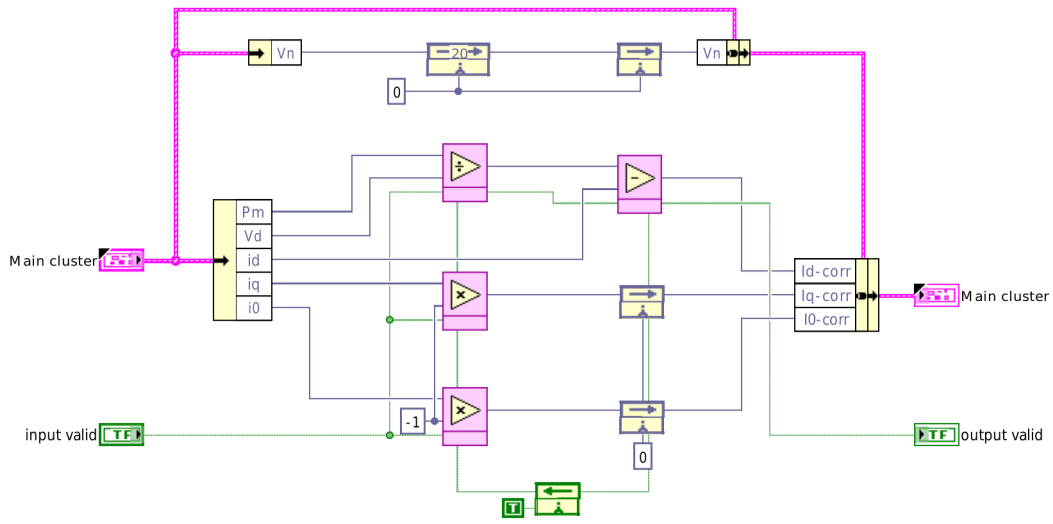

Figure 103: Block scheme example aimed to show handshaking procedure and the pipeline delays.

can be considered valid or not. This happens because in FPGA programming at each cycle the operators perform continuously parallel calculations, not necessarily on "valid" values. Therefore the quantities that in a particular block do not undergo operations must be delayed. Knowing when a value is considered "valid", thanks to the handshake, allows a much more precise synchronisation.

Fig.103 better explains this procedure. The divisor in figure returns a valid value of the result 20 clock cycles after it receives the input. It means that it returns 19 invalid output before the correct result. The two parallel multipliers instead return a valid output at every clock cycles. Therefore, the handshaking is controlled by the divisor, that activates the subtractor block by the handshaking signal represented in dotted-green in the figure. In this way the subtractor knows which input is valid and considering its computational time gives an output valid signal to the next block. The parallel signal V_n does not participate in any calculation operation, therefore it must be delayed by the ticks required by the divider (20) and the subtractor (1) as shown in the same figure.

The program developed for the AFS, for the above considerations, has been divided into three main blocks: acquisition, processing, sending control signals of the inverter gates. The acquisition, considering the duration of the conversion of the signals equal to 10 µs and the duration of the LCT

set at 200 µs, is started after 190 µs from the start of the program and is carried out in parallel to the other two blocks, so that this phase does not involve a period of non-functioning of the modulator. The acquired values are written on flip-flop First In First Out (FIFO), variable characterised by the best performance for the communication of values within the same program and between parallel cycles in FPGA.

The second block is represented by the algorithm which determines the compensating currents and the associated gates-control signals. The algorithm was developed within an SCTL, and a throughput of 1 $cycle/sample$ was imposed in each elementary block, with an output register for the handshaking chain. The algorithm has been divided into thirteen blocks (SubVI in LabVIEW), based on the function they perform. Below is the list of SubVIs made with associated their function and the duration (in tick) required by each. It is worth noting that the FPGA adopted has an internal 40 MHz clock, thus a tick lasts 25 ns.

 , **Scaling**, 2 ticks,
this block perform the scaling of the measured quantities;

 , **EPLL**, 26 ticks, in this block an Enhanced Phase-Locked Loop (EPLL) is implemented, returning as output the voltages phase and amplitude. It lasts so much because of the presence of sine-cosine functions;

 , **Voltages generation**, 25 ticks, based on the previously determined voltage phase and amplitude this block generates three voltages synchronised with the measured ones. This block also suffers the presence of sine and cosine functions;

 , **Clarke transform**, 3 ticks, this block simply calculates the Clarke transform of the voltages, load currents and inverter currents;

 , **Park transform**, 2 ticks, as above but this block calculates the Park transform;

 , **Average Power**, 13 ticks, this block determines the instantaneous power in d-q-0 coordinates and the mean value of the active one by a second-order Finite Impulse Response (FIR) filter;

 , **Compensating currents**, 23 ticks, in this block are calculated the compensating current (see (6) in chapter 4 section 4.2). It lasts so much because of the presence of a division operation;

 , **PI controller**, 5 ticks, in this block is developed the PI control of the current-loop with anti-windup;

 , **Park anti-transform**, 2 ticks, this block calculates the Park anti-transform of the compensating currents;

 , **Feed Forward**, 1 tick, this block add the V_α an V_β values to compensating currents $\alpha - \beta$ respectively;

 , **Prism Determination**, 3 ticks, this block identifies the prism in which the reference vector is located, see chapter 6;

 , **Tetrahedron & duty ratios matrix**, 5 ticks, this block identifies the tetrahedron in which the reference vector is located and the associated duty-ratios matrix;

 , **Time intervals determination**, 4 ticks, this block determines each time interval of each switching vector that is modulated in order to obtain the reference vector.

The duration of the entire algorithm is equal to 114 ticks, equal to 2.85 us, less than the duration of the dead time chosen for the inverter. For this reason are introduced six ticks of delay (120 ticks, 3 µs). Fig.104 depicts the entire algorithm block-scheme. On the left, it can be seen the input data wire (pink) and the input valid wire (green). The algorithm is inside a SCTL with a fixed number of iteration (120). On the right, it can be seen the times-cluster and a disabled structure in which is possible to activate a

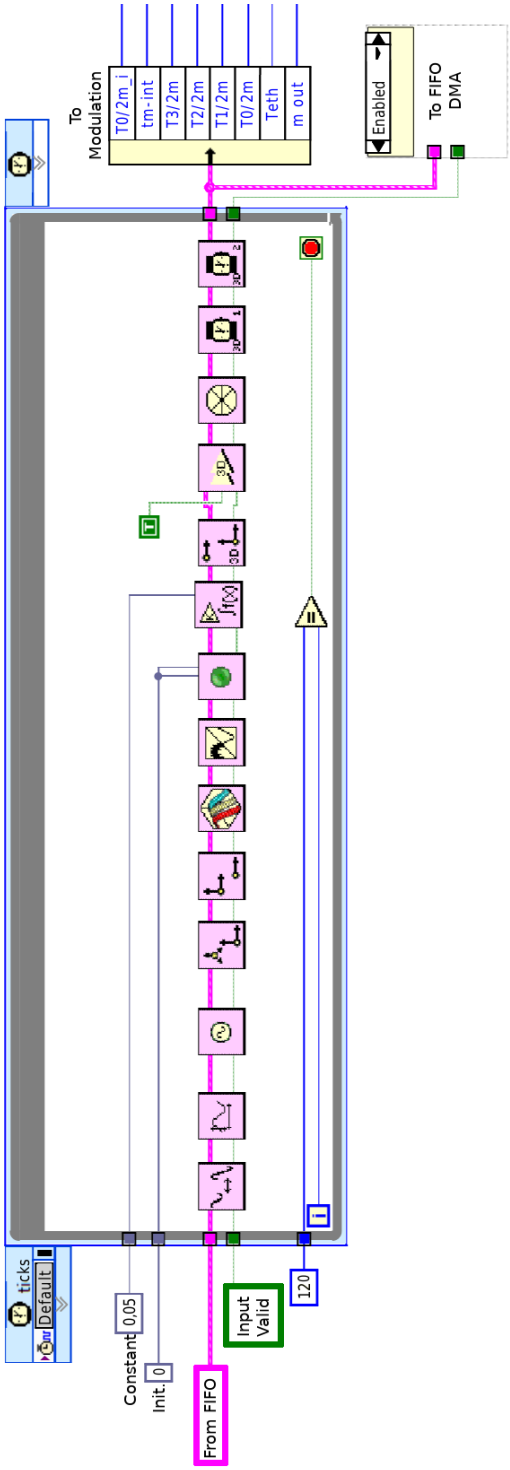

Figure 104: Block scheme of the developed algorithm in LabVIEW.

Table 28: Times sequence associated to a Bus Clamped 3D-SVPWM.

$\frac{T_0}{2}i$	T_{DT}	$\frac{T_1}{2}$	T_{DT}	$\frac{T_2}{2}$	T_{DT}	T_3	T_{DT}	$\frac{T_2}{2}$	T_{DT}	$\frac{T_1}{2}$	T_{DT}	$\frac{T_0}{2}$

"Write to FIFO Direct Memory Access (DMA)" function in order to monitor the behaviour of the algorithm.

The third block includes nested "Case structures". The first is a function of the prism identified and therefore has six cases; the second is a function of the identified tetrahedron, then related on which of the four tetrahedra of the considered prism the reference vector is located; the third includes a For-Loop that runs all possible states, determined on the basis of the type of modulation chosen. Each state consists of an SCTL that writes the control signals of the high and low switches (of each of the four legs) in the digital output module.

The modulation chosen is a 3D Space Vector Pulse Width Modulation (3D-SVPWM) Bus Clamped. This allows to considerably reduce the number of commutations, and therefore the incidence of the dead time on the total modulation period, to the detriment of a worse precision in the realization of the waveform. The sequence of the times associated with this modulation is shown in Tab.28.

The times are calculated from the blocks described above and are measured in ticks. The SCTL guarantees that the digital output is maintained for the desired number of ticks. The $\frac{T_0}{2}i$ time in Tab.28 is equivalent to the $\frac{T_0}{2}$ time determined by the described blocks but subtracted from the 120 ticks necessary for the algorithm execution. The digital output signals are negations of those actually associated with switching vectors since an inverting optoisolator is installed before the inverter.

In Fig.105 is shown one of the various combinations of cases related to the structure of the third block.

A test with bus voltage equal to 100 V and modulation index equal to 0.6 was performed in the laboratory to verify the correctness of the modulation. Fig.106,107,108 show the modulating signals in three different tetrahedra, during the modulation of a three-phase symmetric system.

Future research involves tuning the PI regulator of the current loop and generating non-sinusoidal waveforms representing possible three-phase compensating currents.

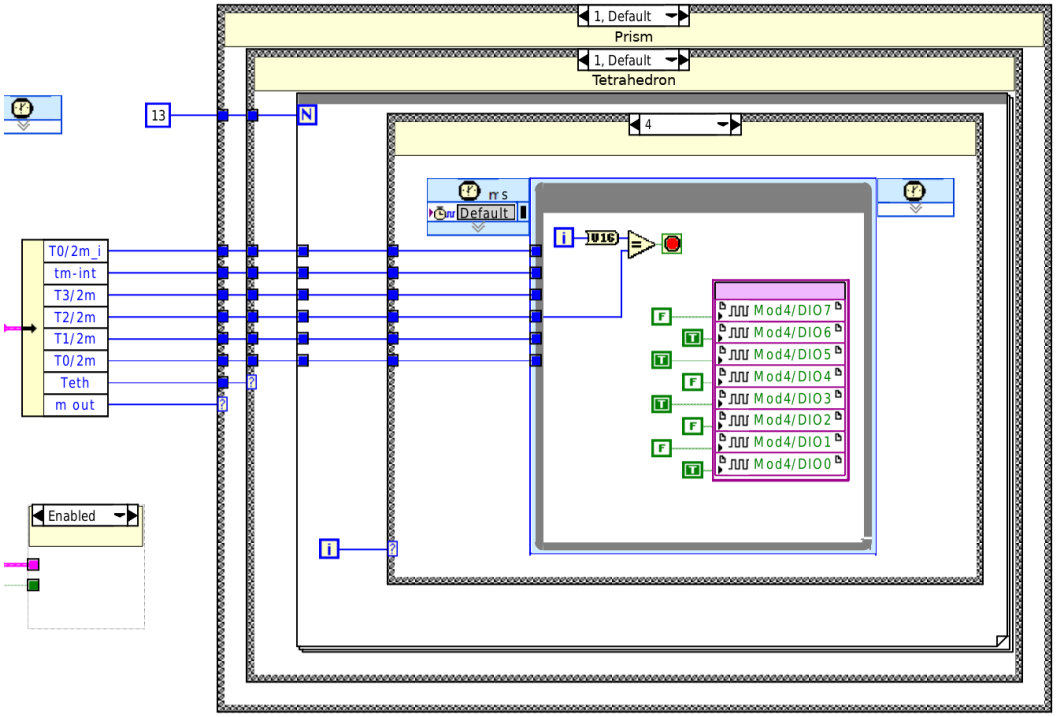

Figure 105: Block scheme of the gate control signals output in LabVIEW.

Figure 106: Modulation control signals of prism 1 tethraedron 1.

Figure 107: Modulation control signals of prism 3 tethraedron 2.

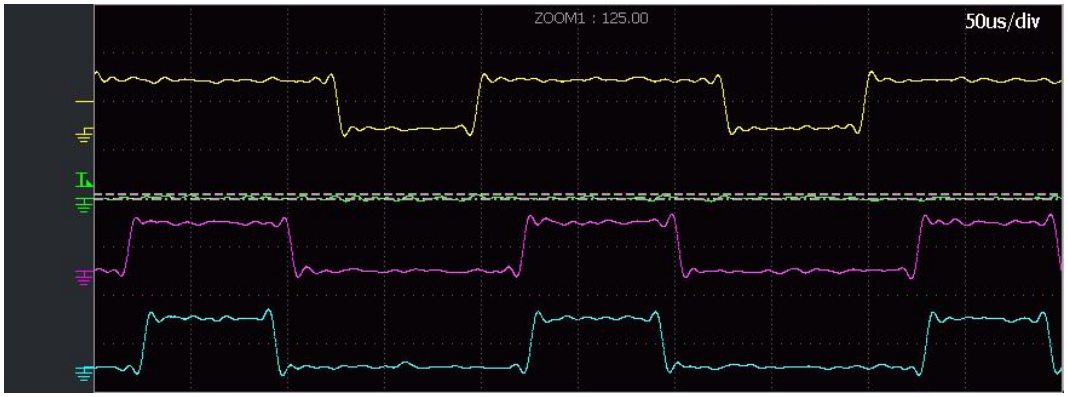

Figure 108: Modulation control signals of prism 6 tethraedron 1.

CONCLUSIONS AND FORTHCOMING RESEARCH

In the present PhD thesis, the design of an integrated Active Filtering System with an Energy Storage System based on Sodium Metal Halides Battery technology, for Power Quality improvement in Microgrids, has been developed.

The two investigations presented in chapters 2 and 3 show the technical and economic advantages linked to the realisation of a Microgrid with ESS and generation from photovoltaic sources (traditional and CPV).

The feasibility of the control algorithm of the AFS inverter is shown in chapter 4. The proposed control algorithm makes it possible to generate compensating currents by calculating the instantaneous active power, permitting at the same time the charging and discharging of the battery during compensation.

In order to correctly evaluate the behaviour of the system, a Thévenin model of the SMHB used is then implemented. The model also considers the iron effect on battery reactions and has a maximum error of 1.7% in the lowest State of Charge.

Subsequently, the sizing of an LC filter used for the decoupling of AFS and SMHB battery is presented. The introduction of the passive filter is necessary to preserve the battery from the deleterious effect of the high dynamics of the active filter. Therefore, the decoupling between the management of battery charging/discharging and the active filtering, allows avoiding that the battery manages the high current variations and reduces the voltage ripple in the DC-link.

Chapter 7 is dedicated to the analysis of one of the possible smart strategies for controlling the charge and discharge of the SMHB battery. In particular, two Frequency Based energy Management strategies (one threshold, two thresholds) have been implemented referring to production and consumption data of the island of Borkum in Germany, place where the European project NETfficient has been implemented. The results obtained from the comparison shows how the strategy with two thresholds allows obtaining better results, especially in the applications related to pick-shaving.

The last chapter is dedicated to the preliminary experimental validation of the AFS. The future research activities have been already planned its completion. In particular, a series of verification tests in compliance with

the actual standard will be carried out. Finally, the proposed AFS will be put into service in the Renewable Energies Platform of Macchiareddu, in Sardinia.

PUBLICATIONS

[1] A. Salimbeni, M. Boi, I. Marongiu, M. Porru and A. Damiano, "Integration of active filter and energy storage system for power quality improvement in microgrids," 2016 International Symposium on Power Electronics, Electrical Drives, Automation and Motion (SPEEDAM), Anacapri, 2016, pp. 709-714. doi: 10.1109/SPEEDAM.2016.7526040

[2] M. Gawronska, C. S. Piattaforma, S. Casula, A. Salimbeni and A. Damiano, "A test bench for microgrids powered by Concentrator photovoltaic systems," 2017 6th International Conference on Clean Electrical Power (ICCEP), Santa Margherita Ligure, 2017, pp. 262-268. doi: 10.1109/ICCEP.2017.8004825

[3] C. Sanna, M. Gawronska, A. Salimbeni, M. Porru and A. Damiano, "Experimental assessment of ESS integration in a microgrid supplied by photovoltaic," 2017 AEIT International Annual Conference, Cagliari, 2017, pp. 1-6. doi: 10.23919/AEIT.2017.8240514

[4] M. Boi, A. Salimbeni and A. Damiano, "A Thévenin circuit modelling approach for sodium metal halides batteries," IECON 2017 - 43rd Annual Conference of the IEEE Industrial Electronics Society, Beijing, 2017, pp. 7611-7616. doi: 10.1109/IECON.2017.8217334

[5] M. Porru, A. Serpi, A. Salimbeni and A. Damiano, "An advanced frequency-based energy management of hybrid energy storage systems for microgrids," IECON 2017 - 43rd Annual Conference of the IEEE Industrial Electronics Society, Beijing, 2017, pp. 7617-7622. doi: 10.1109/IECON.2017.8217335

[6] A. Salimbeni, A. Serpi, M. Porru and A. Damiano, "Integration of Sodium Metal Halides Batteries in Microgrids for Providing Active Filtering Services," 2018 International Symposium on Power Electronics, Electrical Drives, Automation and Motion (SPEEDAM), Amalfi, 2018, pp. 473-478. doi: 10.1109/SPEEDAM.2018.8445376

[7] M. Boi, D. Battaglia, A. Salimbeni, A. Damiano, "A Non-Linear Electrical Model for Iron Doped Sodium Metal Halides Batteries," 2018 Energy Conversion Congress and Exposition (ECCE 2018), Portland, 2018,

[8] A. Damiano, M. Porru, A. Salimbeni, A. Serpi, V. Castiglia, A. O. Di Tommaso, R. Miceli, G. Schettino, "Batteries for Aerospace: a Brief Review," 2018 Associazione Italiana di Elettrotecnica, Elettronica, Automazione, Informatica e Telecomunicazioni (AEIT 2018), Bari, 2018,

LIST OF FIGURES

LIST OF TABLES

BIBLIOGRAPHY

[1] Andreas Schmidt, Ana Ivanova, and Mike S. Schäfer. "Media attention for climate change around the world: A comparative analysis of newspaper coverage in 27 countries". In: *Global Environmental Change* 23.5 (Oct. 1, 2013), pp. 1233–1248. ISSN: 0959-3780. DOI: 10.1016/j.gloenvcha.2013.07.020. URL: http://www.sciencedirect.com/science/article/pii/S095937801300126X (visited on 08/16/2018).

[2] *Full text of President Obama's speech on the Paris Climate Agreement*. ABC7 San Francisco. Dec. 12, 2015. URL: https://abc7news.com/1120330/ (visited on 08/16/2018).

[3] Leonardo DiCaprio. "Leonardo DiCaprio at the UN: 'Climate change is not hysteria – it's a fact'". In: *The Guardian* (Sept. 23, 2014). ISSN: 0261-3077. URL: https://www.theguardian.com/environment/2014/sep/23/leonarodo-dicaprio-un-climate-change-speech-new-york (visited on 08/16/2018).

[4] UNFCCC. *Edward Norton - Climate Neutral Now*. URL: https://www.youtube.com/watch?v=XwsMjI7XP7Y (visited on 08/16/2018).

[5] Alison Anderson. "Sources, media, and modes of climate change communication: the role of celebrities: Sources, media, and modes of climate change communication". In: *Wiley Interdisciplinary Reviews: Climate Change* 2.4 (July 2011), pp. 535–546. ISSN: 17577780. DOI: 10.1002/wcc.119. URL: http://doi.wiley.com/10.1002/wcc.119 (visited on 08/17/2018).

[6] *Climate Change Used to Be a Bipartisan Issue. Here's What Changed*. Time. URL: http://time.com/4874888/climate-change-politics-history/ (visited on 08/17/2018).

[7] Oliver Milman, David Smith, and Damian Carrington. "Donald Trump confirms US will quit Paris climate agreement". In: *The Guardian* (June 1, 2017). ISSN: 0261-3077. URL: https://www.theguardian.com/environment/2017/jun/01/donald-trump-confirms-us-will-quit-paris-climate-deal (visited on 08/16/2018).

[8] Michael D. Shear. "Trump Will Withdraw U.S. From Paris Climate Agreement". In: *The New York Times* (Jan. 20, 2018). ISSN: 0362-4331. URL: https://www.nytimes.com/2017/06/01/climate/trump-paris-climate-agreement.html (visited on 08/17/2018).

[9] "Good Morning, IRENA: New Energy Agency Opens Its Doors". In: *The Electricity Journal* 22.3 (Apr. 1, 2009), pp. 2–3. ISSN: 1040-6190. DOI: 10.1016/j.tej.2009.03.006. URL: http://www.sciencedirect.com/science/article/pii/S1040619009000669 (visited on 08/17/2018).

[10] *Global Energy Transformation: A Roadmap to 2050*. /publications/2018/Apr/Global-Energy-Transition-A-Roadmap-to-2050. URL: /publications/2018/Apr/Global-Energy-Transition-A-Roadmap-to-2050 (visited on 08/17/2018).

[11] Paul Komor and Timothy Molnar. *Background Paper On Distributed Renewable Energy Generation And Integration*. Feb. 20, 2015. (Visited on 08/18/2018).

[12] "Off-grid renewable energy solutions". In: (), p. 20.

[13] "IRENA - Renewable capacity statistics 2018". In: (), p. 60.

[14] "RENEWABLES 2018 GLOBAL STATUS". In: (), p. 325. URL: http://www.ren21.net/wp-content/uploads/2018/06/17-8652_GSR2018_FullReport_web_final_.pdf (visited on 08/21/2018).

[15] Antonio Scala et al. "Distributed Generation and Resilience in Power Grids". In: vol. 7722. Aug. 28, 2012. DOI: 10.1007/978-3-642-41485-5_7.

[16] R. H. Lasseter. "Microgrids and Distributed Generation". In: *Journal of Energy Engineering* 133.3 (Sept. 2007), pp. 144–149. ISSN: 0733-9402, 1943-7897. DOI: 10.1061/(ASCE)0733-9402(2007)133:3(144). URL: http://ascelibrary.org/doi/10.1061/%28ASCE%290733-9402%282007%29133%3A3%28144%29 (visited on 08/22/2018).

[17] E. Barklund et al. "Energy Management in Autonomous Microgrid Using Stability-Constrained Droop Control of Inverters". In: *IEEE Transactions on Power Electronics* 23.5 (2008), pp. 2346–2352. ISSN: 0885-8993. DOI: 10.1109/TPEL.2008.2001910.

[18] R. H. Lasseter and P. Paigi. "Microgrid: a conceptual solution". In: *2004 IEEE 35th Annual Power Electronics Specialists Conference (IEEE Cat. No.04CH37551)*. Vol. 6. 2004, 4285–4290 Vol.6. DOI: 10.1109/PESC.2004.1354758.

[19] Dan T. Ton and Merrill A. Smith. "The U.S. Department of Energy's Microgrid Initiative". In: *The Electricity Journal* 25.8 (Oct. 2012), pp. 84–94. ISSN: 10406190. DOI: 10.1016/j.tej.2012.09.013. URL: http://linkinghub.elsevier.com/retrieve/pii/S1040619012002254 (visited on 08/22/2018).

[20] N. Hatziargyriou et al. "Microgrids". In: *IEEE Power and Energy Magazine* 5.4 (2007), pp. 78–94. ISSN: 1540-7977. DOI: 10.1109/MPAE.2007.376583.

[21] F. Katiraei et al. "Microgrids management". In: *IEEE Power and Energy Magazine* 6.3 (2008), pp. 54–65. ISSN: 1540-7977. DOI: 10.1109/MPE.2008.918702.

[22] "IEEE Guide for the Interoperability of Energy Storage Systems Integrated with the Electric Power Infrastructure". In: *IEEE Std 2030.2-2015* (2015), pp. 1–138. DOI: 10.1109/IEEESTD.2015.7140715.

[23] R. D'Agostino et al. "A Vanadium-Redox-Flow-Battery Model for Evaluation of Distributed Storage Implementation in Residential Energy Systems". In: *IEEE Transactions on Energy Conversion* 30.2 (2015), pp. 421–430. ISSN: 0885-8969. DOI: 10.1109/TEC.2014.2369437.

[24] A. Marongiu, A. Damiano, and M. Heuer. "Experimental analysis of lithium iron phosphate battery performances". In: *2010 IEEE International Symposium on Industrial Electronics*. 2010, pp. 3420–3424. DOI: 10.1109/ISIE.2010.5637749.

[25] J. M. Guerrero et al. "Hierarchical Control of Droop-Controlled AC and DC Microgrids—A General Approach Toward Standardization". In: *IEEE Transactions on Industrial Electronics* 58.1 (2011), pp. 158–172. ISSN: 0278-0046. DOI: 10.1109/TIE.2010.2066534.

[26] J. A. P. Lopes, C. L. Moreira, and A. G. Madureira. "Defining control strategies for MicroGrids islanded operation". In: *IEEE Transactions on Power Systems* 21.2 (2006), pp. 916–924. ISSN: 0885-8950. DOI: 10.1109/TPWRS.2006.873018.

[27] R. H. Lasseter. "MicroGrids". In: *2002 IEEE Power Engineering Society Winter Meeting. Conference Proceedings (Cat. No.02CH37309)*. Vol. 1. 2002, 305–308 vol.1. DOI: 10.1109/PESW.2002.985003.

[28] Q. Zhong and G. Weiss. "Synchronverters: Inverters That Mimic Synchronous Generators". In: *IEEE Transactions on Industrial Electronics* 58.4 (2011), pp. 1259–1267. ISSN: 0278-0046. DOI: 10.1109/TIE.2010.2048839.

[29] C. Chen et al. "Optimal Allocation and Economic Analysis of Energy Storage System in Microgrids". In: *IEEE Transactions on Power Electronics* 26.10 (2011), pp. 2762–2773. ISSN: 0885-8993. DOI: 10.1109/TPEL.2011.2116808.

[30] J. Kim et al. "Cooperative Control Strategy of Energy Storage System and Microsources for Stabilizing the Microgrid during Islanded Operation". In: *IEEE Transactions on Power Electronics* 25.12 (2010), pp. 3037–3048. ISSN: 0885-8993. DOI: 10.1109/TPEL.2010.2073488.

[31] S. Bahramirad, W. Reder, and A. Khodaei. "Reliability-Constrained Optimal Sizing of Energy Storage System in a Microgrid". In: *IEEE Transactions on Smart Grid* 3.4 (2012), pp. 2056–2062. ISSN: 1949-3053. DOI: 10.1109/TSG.2012.2217991.

[32] C. Chen et al. "Smart energy management system for optimal microgrid economic operation". In: *IET Renewable Power Generation* 5.3 (2011), pp. 258–267. ISSN: 1752-1416. DOI: 10.1049/iet-rpg.2010.0052.

[33] F. Wang, J. L. Duarte, and M. A. M. Hendrix. "Grid-Interfacing Converter Systems With Enhanced Voltage Quality for Microgrid Application—Concept and Implementation". In: *IEEE Transactions on Power Electronics* 26.12 (2011), pp. 3501–3513. ISSN: 0885-8993. DOI: 10.1109/TPEL.2011.2147334.

[34] Simon P. Philipps et al. *Current Status of Concentrator Photovoltaic (CPV) Technology*. NREL/TP–5J00-65130, 1351597. Dec. 1, 2015. DOI: 10.2172/1351597. URL: http://www.osti.gov/servlets/purl/1351597/ (visited on 08/27/2018).

[35] Martin A. Green et al. "Solar cell efficiency tables (version 50)". In: *Progress in Photovoltaics: Research and Applications* 25.7 (July 2017), pp. 668–676. ISSN: 10627995. DOI: 10.1002/pip.2909. URL: http://doi.wiley.com/10.1002/pip.2909 (visited on 08/28/2018).

[36] P. Pérez-Higueras et al. "High Concentrator PhotoVoltaics efficiencies: Present status and forecast". In: *Renewable and Sustainable Energy Reviews* 15.4 (May 1, 2011), pp. 1810–1815. ISSN: 1364-0321. DOI: 10.1016/j.rser.2010.11.046. URL: http://www.sciencedirect.com/science/article/pii/S1364032110004156 (visited on 08/28/2018).

[37] Katie Shanks, S. Senthilarasu, and Tapas K. Mallick. "Optics for concentrating photovoltaics: Trends, limits and opportunities for materials and design". In: *Renewable and Sustainable Energy Reviews* 60 (July 1, 2016), pp. 394–407. ISSN: 1364-0321. DOI: 10.1016/j.rser.2016.01.089. URL: http://www.sciencedirect.com/science/article/pii/S1364032116001192 (visited on 08/28/2018).

[38] Joan E. Haysom et al. "Learning curve analysis of concentrated photovoltaic systems: Concentrated photovoltaic systems". In: *Progress in Photovoltaics: Research and Applications* 23.11 (Nov. 2015), pp. 1678–1686. ISSN: 10627995. DOI: 10.1002/pip.2567. URL: http://doi.wiley.com/10.1002/pip.2567 (visited on 08/28/2018).

[39] C. Sanna, M. Gawronska, and A. Damiano. "Energy performance of concentrator and flat plate photovoltaics in the mediterranean area". In: *2015 International Conference on Renewable Energy Research and Applications (ICRERA)*. 2015, pp. 760–765. DOI: 10.1109/ICRERA.2015.7418513.

[40] R. H. Lasseter. "Smart Distribution: Coupled Microgrids". In: *Proceedings of the IEEE* 99.6 (2011), pp. 1074–1082. ISSN: 0018-9219. DOI: 10.1109/JPROC.2011.2114630.

[41] C. A. Hill et al. "Battery Energy Storage for Enabling Integration of Distributed Solar Power Generation". In: *IEEE Transactions on Smart Grid* 3.2 (2012), pp. 850–857. ISSN: 1949-3053. DOI: 10.1109/TSG.2012.2190113.

[42] A. Damiano et al. "Real-Time Control Strategy of Energy Storage Systems for Renewable Energy Sources Exploitation". In: *IEEE Transactions on Sustainable Energy* 5.2 (2014), pp. 567–576. ISSN: 1949-3029. DOI: 10.1109/TSTE.2013.2273400.

[43] M. Musio et al. "Optimal management strategy of energy storage systems for RES-based microgrids". In: *IECON 2015 - 41st Annual Conference of the IEEE Industrial Electronics Society*. 2015, pp. 005044–005049. DOI: 10.1109/IECON.2015.7392891.

[44] M. Liserre, R. Teodorescu, and F. Blaabjerg. "Stability of photovoltaic and wind turbine grid-connected inverters for a large set of grid impedance values". In: *IEEE Transactions on Power Electronics* 21.1 (2006), pp. 263–272. ISSN: 0885-8993. DOI: 10.1109/TPEL.2005.861185.

[45] J. H. R. Enslin and P. J. M. Heskes. "Harmonic interaction between a large number of distributed power inverters and the distribution network". In: *IEEE 34th Annual Conference on Power Electronics Specialist, 2003. PESC '03.* Vol. 4. 2003, 1742–1747 vol.4. DOI: 10.1109/PESC.2003.1217719.

[46] X. Zhou et al. "Four-Leg Converters With Improved Common Current Sharing and Selective Voltage-Quality Enhancement for Islanded Microgrids". In: *IEEE Transactions on Power Delivery* 31.2 (2016), pp. 522–531. ISSN: 0885-8977. DOI: 10.1109/TPWRD.2015.2450111.

[47] B. Singh, K. Al-Haddad, and A. Chandra. "A review of active filters for power quality improvement". In: *IEEE Transactions on Industrial Electronics* 46.5 (1999), pp. 960–971. ISSN: 0278-0046. DOI: 10.1109/41.793345.

[48] C. A. Quinn and N. Mohan. "Active filtering of harmonic currents in three-phase, four-wire systems with three-phase and single-phase nonlinear loads". In: *[Proceedings] APEC '92 Seventh Annual Applied Power Electronics Conference and Exposition*. 1992, pp. 829–836. DOI: 10.1109/APEC.1992.228328.

[49] S. Chen, H. Beng Gooi, and M. Wang. "Sizing of energy storage for microgrids". In: *2012 IEEE Power and Energy Society General Meeting*. 2012, pp. 1–1. DOI: 10.1109/PESGM.2012.6345233.

[50] S. Vazquez et al. "Energy Storage Systems for Transport and Grid Applications". In: *IEEE Transactions on Industrial Electronics* 57.12 (2010), pp. 3881–3895. ISSN: 0278-0046. DOI: 10.1109/TIE.2010.2076414.

[51] A. Damiano, C. Musio, and I. Marongiu. "Experimental validation of a dynamic energy model of a battery electric vehicle". In: *2015 International Conference on Renewable Energy Research and Applications (ICRERA)*. 2015, pp. 803–808. DOI: 10.1109/ICRERA.2015.7418523.

[52] Reza Hemmati and Hedayat Saboori. "Emergence of hybrid energy storage systems in renewable energy and transport applications – A review". In: *Renewable and Sustainable Energy Reviews* 65 (Nov. 1, 2016), pp. 11–23. ISSN: 1364-0321. DOI: 10.1016/j.rser.2016.06.

029. URL: http://www.sciencedirect.com/science/article/pii/S1364032116302374 (visited on 09/10/2018).

[53] Lanre Olatomiwa et al. "Energy management strategies in hybrid renewable energy systems: A review". In: *Renewable and Sustainable Energy Reviews* 62 (Sept. 1, 2016), pp. 821–835. ISSN: 1364-0321. DOI: 10.1016/j.rser.2016.05.040. URL: http://www.sciencedirect.com/science/article/pii/S1364032116301502 (visited on 09/10/2018).

[54] R. A. Dougal, S. Liu, and R. E. White. "Power and life extension of battery-ultracapacitor hybrids". In: *IEEE Transactions on Components and Packaging Technologies* 25.1 (2002), pp. 120–131. ISSN: 1521-3331. DOI: 10.1109/6144.991184.

[55] Lijun Gao, R. A. Dougal, and Shengyi Liu. "Power enhancement of an actively controlled battery/ultracapacitor hybrid". In: *IEEE Transactions on Power Electronics* 20.1 (2005), pp. 236–243. ISSN: 0885-8993. DOI: 10.1109/TPEL.2004.839784.

[56] I. Chotia and S. Chowdhury. "Battery storage and hybrid battery supercapacitor storage systems: A comparative critical review". In: *2015 IEEE Innovative Smart Grid Technologies - Asia (ISGT ASIA)*. 2015, pp. 1–6. DOI: 10.1109/ISGT-Asia.2015.7387080.

[57] E. Micolano, R. Lazzari, and L. Pellegrino. "Influence of management and system configuration on performances and lifetime of lithium-ion batteries". In: *2015 AEIT International Annual Conference (AEIT)*. 2015, pp. 1–6. DOI: 10.1109/AEIT.2015.7415243.

[58] S. W. Alnaser and L. F. Ochoa. "Optimal Sizing and Control of Energy Storage in Wind Power-Rich Distribution Networks". In: *IEEE Transactions on Power Systems* 31.3 (2016), pp. 2004–2013. ISSN: 0885-8950. DOI: 10.1109/TPWRS.2015.2465181.

[59] M. Ammar and G. Joós. "A Short-Term Energy Storage System for Voltage Quality Improvement in Distributed Wind Power". In: *IEEE Transactions on Energy Conversion* 29.4 (2014), pp. 997–1007. ISSN: 0885-8969. DOI: 10.1109/TEC.2014.2360071.

[60] M. D. Mufti et al. "Supervisory Adaptive Predictive Control Scheme for Supercapacitor Energy Storage System". In: *IEEE Systems Journal* 9.3 (2015), pp. 1020–1030. ISSN: 1932-8184. DOI: 10.1109/JSYST.2013.2289251.

[61] B. Liu et al. "System Operation and Energy Management of a Renewable Energy-Based DC Micro-Grid for High Penetration Depth Application". In: *IEEE Transactions on Smart Grid* 6.3 (2015), pp. 1147–1155. ISSN: 1949-3053. DOI: 10.1109/TSG.2014.2374163.

[62] N. Mendis, K. M. Muttaqi, and S. Perera. "Management of Battery-Supercapacitor Hybrid Energy Storage and Synchronous Condenser for Isolated Operation of PMSG Based Variable-Speed Wind Turbine Generating Systems". In: *IEEE Transactions on Smart Grid* 5.2 (2014), pp. 944–953. ISSN: 1949-3053. DOI: 10.1109/TSG.2013.2287874.

[63] S. K. Kollimalla, M. K. Mishra, and N. L. Narasamma. "Design and Analysis of Novel Control Strategy for Battery and Supercapacitor Storage System". In: *IEEE Transactions on Sustainable Energy* 5.4 (2014), pp. 1137–1144. ISSN: 1949-3029. DOI: 10.1109/TSTE.2014.2336896.

[64] S. Adhikari et al. "A battery/supercapacitor hybrid energy storage system for DC microgrids". In: *2016 IEEE 8th International Power Electronics and Motion Control Conference (IPEMC-ECCE Asia)*. 2016, pp. 1747–1753. DOI: 10.1109/IPEMC.2016.7512558.

[65] N. R. Tummuru, M. K. Mishra, and S. Srinivas. "Dynamic Energy Management of Renewable Grid Integrated Hybrid Energy Storage System". In: *IEEE Transactions on Industrial Electronics* 62.12 (2015), pp. 7728–7737. ISSN: 0278-0046. DOI: 10.1109/TIE.2015.2455063.

[66] S. Wang et al. "Design and advanced control strategies of a hybrid energy storage system for the grid integration of wind power generations". In: *IET Renewable Power Generation* 9.2 (2015), pp. 89–98. ISSN: 1752-1416. DOI: 10.1049/iet-rpg.2013.0340.

[67] A. Mohamed, V. Salehi, and O. Mohammed. "Real-Time Energy Management Algorithm for Mitigation of Pulse Loads in Hybrid Microgrids". In: *IEEE Transactions on Smart Grid* 3.4 (2012), pp. 1911–1922. ISSN: 1949-3053. DOI: 10.1109/TSG.2012.2200702.

[68] Y. Ye, R. Sharma, and P. Garg. "An integrated power management strategy of hybrid energy storage for renewable application". In: *IECON 2014 - 40th Annual Conference of the IEEE Industrial Electronics Society*. 2014, pp. 3088–3093. DOI: 10.1109/IECON.2014.7048951.

[69] B. Hredzak, V. G. Agelidis, and M. Jang. "A Model Predictive Control System for a Hybrid Battery-Ultracapacitor Power Source". In: *IEEE Transactions on Power Electronics* 29.3 (2014), pp. 1469–1479. ISSN: 0885-8993. DOI: 10.1109/TPEL.2013.2262003.

[70] W. Jiang et al. "Research on power sharing strategy of hybrid energy storage system in photovoltaic power station based on multi-objective optimisation". In: *IET Renewable Power Generation* 10.5 (2016), pp. 575–583. ISSN: 1752-1416. DOI: 10.1049/iet-rpg.2015.0199.

[71] Dr Simon Philipps et al. "Photovoltaics Report". In: (), p. 47.

[72] "IRENA - REthinking energy 2017". In: (), p. 130.

[73] Seth B. Darling et al. "Assumptions and the levelized cost of energy for photovoltaics". In: *Energy & Environmental Science* 4.9 (2011), p. 3133. ISSN: 1754-5692, 1754-5706. DOI: 10.1039/c0ee00698j. URL: http://xlink.rsc.org/?DOI=c0ee00698j (visited on 09/26/2018).

[74] *JRC Photovoltaic Geographical Information System (PVGIS) - European Commission*. URL: http://re.jrc.ec.europa.eu/pvg_download/map_index.html (visited on 09/26/2018).

[75] "JRC PV Status Report". In: (), p. 90.

[76] "Annual Energy Outlook 2017 with projections to 2050". In: (2016), p. 64.

[77] Carla Sanna et al. *Performance analysis of non-linear load effects on a micro-grid supplied by photovoltaic power plants*. Sept. 2014.

[78] Masoud Karimi-Ghartema. "Enhanced Phase-Locked Loop". In: *Enhanced Phase-Locked Loop Structures for Power and Energy Applications*. IEEE, 2014. DOI: 10.1002/9781118795187.ch2. URL: https://ieeexplore.ieee.org/xpl/articleDetails.jsp?arnumber=6798205.

[79] R. Zhang et al. "Three-dimensional space vector modulation for four-leg voltage-source converters". In: *IEEE Transactions on Power Electronics* 17.3 (2002), pp. 314–326. ISSN: 0885-8993. DOI: 10.1109/TPEL.2002.1004239.

[80] J. L Sudworth. "The sodium/nickel chloride (ZEBRA) battery". In: *Journal of Power Sources*. Journal of Power Sources Volume 100 100.1 (Nov. 30, 2001), pp. 149–163. ISSN: 0378-7753. DOI: 10.1016/S0378-7753(01)00891-6. URL: http://www.sciencedirect.com/science/article/pii/S0378775301008916 (visited on 09/10/2018).

[81] Cord-H Dustmann. *Advances in ZEBRA batteries - ScienceDirect*. URL: https://www.sciencedirect.com/science/article/pii/S0378775303009418 (visited on 09/10/2018).

[82] S Restello, G Lodi, and A.K. Miraldi. *Sodium Nickel Chloride Batteries for telecom application: A solution to critical high energy density deployment in telecom facilities*. Sept. 2012.

[83] R. Manzoni. "Sodium Nickel Chloride batteries in transportation applications". In: *2015 International Conference on Electrical Systems for Aircraft, Railway, Ship Propulsion and Road Vehicles (ESARS)*. 2015, pp. 1–6. DOI: 10.1109/ESARS.2015.7101491.

[84] G. Crugnola S. Dambone Sessa G. Lodi C. Parmeggiani R. Benato N. Cosciani and M. Todeschini. *Sodium nickel chloride battery technology for large-scale stationary storage in the high voltage network - ScienceDirect*. URL: https://www.sciencedirect.com/science/article/pii/S0378775315009180 (visited on 09/10/2018).

[85] Min Chen and G. A. Rincon-Mora. "Accurate electrical battery model capable of predicting runtime and I-V performance". In: *IEEE Transactions on Energy Conversion* 21.2 (2006), pp. 504–511. ISSN: 0885-8969. DOI: 10.1109/TEC.2006.874229.

[86] H. Rahimi-Eichi et al. "Battery Management System: An Overview of Its Application in the Smart Grid and Electric Vehicles". In: *IEEE Industrial Electronics Magazine* 7.2 (2013), pp. 4–16. ISSN: 1932-4529. DOI: 10.1109/MIE.2013.2250351.

[87] T. M. O'Sullivan, C. M. Bingham, and R. E. Clark. "Zebra battery technologies for all electric smart car". In: *International Symposium on Power Electronics, Electrical Drives, Automation and Motion, 2006. SPEEDAM 2006.* 2006, pp. 243–. DOI: 10.1109/SPEEDAM.2006.1649778.

[88] S. Grillo et al. "Optimal Management Strategy of a Battery-Based Storage System to Improve Renewable Energy Integration in Distribution Networks". In: *IEEE Transactions on Smart Grid* 3.2 (2012), pp. 950–958. ISSN: 1949-3053. DOI: 10.1109/TSG.2012.2189984.

[89] Sebastian Dambone Sessa et al. "Sodium nickel chloride battery steady-state regime model for stationary electrical energy storage". In: *Journal of Energy Storage* 6 (May 1, 2016), pp. 105–115. ISSN: 2352-152X. DOI: 10.1016/j.est.2016.03.005. URL: http://www.sciencedirect.com/science/article/pii/S2352152X16300470 (visited on 09/10/2018).

[90] M. Musio and A. Damiano. "A non-linear dynamic electrical model of Sodium-Nickel Chloride Batteries". In: *2015 International Conference on Renewable Energy Research and Applications (ICRERA)*. 2015, pp. 872–878. DOI: 10.1109/ICRERA.2015.7418535.

[91] Hanlei Zhang and Mo-Yuen Chow. "Comprehensive dynamic battery modeling for PHEV applications". In: *IEEE PES General Meeting*. 2010, pp. 1–6. DOI: 10.1109/PES.2010.5590108.

[92] T. Kim and W. Qiao. "A hybrid battery model capable of capturing dynamic circuit characteristics and nonlinear capacity effects". In: *2012 IEEE Power and Energy Society General Meeting*. 2012, pp. 1–1. DOI: 10.1109/PESGM.2012.6345454.

[93] M. Boi, A. Salimbeni, and A. Damiano. "A Thévenin circuit modelling approach for sodium metal halides batteries". In: *IECON 2017 - 43rd Annual Conference of the IEEE Industrial Electronics Society*. 2017, pp. 7611–7616. DOI: 10.1109/IECON.2017.8217334.

[94] *The NI LabVIEW High-Performance FPGA Developer's Guide - Now Live! - National Instruments*. URL: https://www.ni.com/tutorial/14600/en/ (visited on 09/12/2018).

[95] David A. Patterson and John L. Hennessy. *Computer organization and design: the hardware/software interface*. 3. ed., rev. OCLC: 255042622. Amsterdam: Elsevier [u.a.], 2008. ISBN: 978-0-12-370606-5.